Master's thesis

NTNU
Norwegian University of Science and Technology
Faculty of Engineering
Department of Marine Technology

Anders Matias Akselsen

Hydrodynamic Analysis of a Floating Renewable Energy Device

Master's thesis in Marine Technology
Supervisor: Bjørnar Pettersen
July 2019

NTNU
Norwegian University of Science and Technology

EDR™ MEDESO

Anders Matias Akselsen

Hydrodynamic Analysis of a Floating Renewable Energy Device

Master's thesis in Marine Technology
Supervisor: Bjørnar Pettersen
July 2019

Norwegian University of Science and Technology
Faculty of Engineering
Department of Marine Technology

NTNU
Norwegian University of
Science and Technology

NTNU
Norwegian University of Science and Technology
Department of Marine Technology

MASTER THESIS IN MARINE HYDRODYNAMICS

SPRING 2019

FOR

Stud.techn. Anders Maties Akselsen

HYDRODYNAMIC ANALYSIS OF WAVE ENRGY CONCEPTS.

The candidate shall investigate the hydrodynamic properties of floating wave energy devices by using Aqwa/Fluent.
Initial, vertical motion of simple geometric bodies, such as a sphere, shall be investigated, and results compared with results published in the literature. Special focus shall be on numerical parameters.
If time allows other actual geometries may be investigated with respect to performance as possible energy devices.

In the thesis the candidate shall present his personal contribution to the resolution of the problem within the scope of the thesis work. Theories and conclusions should be based on mathematical derivation and logic reasoning identifying the various steps in the deduction. The original contribution of the candidate and material taken from other sources shall be clearly defined. Work from other sources shall be properly referenced. The candidate should utilize the existing possibilities for obtaining relevant literature.
The thesis should be organized in a rational manner to give a clear exposition of results, assessments and conclusions. The text should be brief and to the point, with a clear language.

The thesis shall contain the following elements: A text defining the scope, preface, list of contents, summary, main body of thesis, conclusions with recommendations for further work, list of symbols and acronyms, references and appendices. All figures, tables and equations shall be numerated.
It is supposed that Department of Marine Technology, NTNU, can use the results freely in its research work by referring to the student's thesis.
The thesis shall be submitted June 11th , 2019.

Bjørnar Pettersen
Professor/supervisor

Co-supervisor: Ken.Robert G. Jakobsen, EDRMedeso

Abstract

This study covers a hydrodynamic assessment of a wave energy converter device, and on a heaving point-absorber configuration in specific. Many commonly used analysis tools used to evaluate point-absorbing wave energy converters are based on linear models. The foundation in which the linear models are based on is the assumption of small motions. In those cases linear models are efficient and provide good approximations. A contradiction is therefore inevitable as point-absorbers are designed to induce large motions to optimise the power absorption. Many cases and operating conditions are therefore by nature nonlinear. Hence, it is important to have an understanding of which hydrodynamic effects are dominating in different load situations and where it is necessary to model effects of higher order. The main focus of the numerical assessment is to evaluate the impact of nonlinear Froude-Krylov and hydrostatic forces. That is essentially done by accounting for the instantaneous wetted body surface, instead of the mean wetted surface used in a linear analysis. This weak nonlinear model is compared to results from a linear model in which considers the mean wetted surface. Three geometries are assessed; sphere, cylinder and a model scale WEC float. The devises are evaluated in uncontrolled conditions and with optimum PTO force. A secondary objective is to evaluate the impact of the geometrical shape of a point-absorber with respect to absorbed power.

It appears from the results of this study that when the immersed cross-sectional area(CSA) of the device is constant and the waves are rather linear, the linear model can remain accurate. At least in terms of the Froudy-Krylov and hydrostatic forces. When the immersed CSA changes over time, such as for the sphere, nonlinear geometrical effects were induced in large waves and in resonance. The effect was most prominent when an additional damping was applied in large incident waves. There it was seen that the weak nonlinear solution predicted a reduced heave response compared to the linear model, which resulted in a drastically reduced mean power estimation. Based on the findings in this thesis, the linear solution can in this case give an overoptimistic estimation of mean power and consequently give a misleading guide to economic predictions. In linear conditions on the other hand, the linear and weak nonlinear model were in good agreement also for the sphere.

The second objective was to investigate the three geometries with respect to absorbed energy. It was seen that the WEC float absorbed most energy out of the three geometries at resonance and in longer waves. The sphere performed at a similar rate as the two other geometries at resonance, but absorbed substantially less power for larger waves due to the small size. It was argued with the following reasoning: the magnitude of the exciting forces acting on the body increases with size due to the pressure from the incident and diffracted waves being integrated over a larger area. Since the mean power is proportional to the square of the excitation forces, an increase in size will subsequently increase the mean power. Lastly, it was seen that the geometry has a severe impact at resonance, but seem to have less effect when oscillating off resonance. That implies that when control methods are applied, which forces the device to oscillate in resonance, the geometry is important.

Preface

This project serves as a master thesis in the subject TMR4930 Marine Technology, Master Thesis in Marine Hydrodynamical Engineering at the Department of Marine Technology at NTNU. The work was executed in the spring of 2019.

The topic of the thesis is hydrodynamic assessment of a point-absorbing wave energy device, with focus of nonlinear modelling of hydrostatic and incident wave forces.

The report contains a brief overview of the wave energy industry, it's history, challenges and potential. The thesis contains a theoretical background of linear and nonlinear potential theory. The major part of the work is discussion and presentation of the results from the hydrodynamic assessment. In the course of the work, choices and simplifications were made in line with the recommendations of the supervisor, Professor Bjørnar Pettersen and co-supervisor Ken-Robert G. Jakobsen

All the work has been executed by the author, Anders M. Akselsen, and the thesis is a continuation of a project thesis executed in the fall of 2018.

Kristiansand, July 12th, 2019

Anders M. Akselsen

Acknowledgement

I would like to thank my supervisor Professor Bjørnar Pettersen for guidance in all phases of this master thesis.

I would also like to thank EDR Medeso for formulating the objective of the thesis, and especially Ken-Robert G. Jakobsen who also contributed with extensive assistance.

In addition, I would like to thank my family and Karoline for love and support though out my time at NTNU.

A.M.A

Contents

List of Figures

List of Tables

1 Introduction

The world is in need of renewable energy solutions to withstand the rapid temperature increase in the atmosphere. Energy solutions offshore has a huge potential to contribute to the inevitable change, as approximately 70 percent of the earth's surface is covered in water. Ocean waves is an energy source in order of terrawatts worldwide, which to date has not been commercialized. It has the potential to be an important contributor in the mix of renewable energy sources needed to replace fossil fuel as the world's main energy source.

This thesis will contribute with a hydrodynamic assessment of wave energy converter device, and on heaving point-absorber configuration in specific. Many commonly used analysis tools used to evaluate point-absorbing wave energy converters are based on linear models. The foundation in which the linear models are based on is the assumption of small motions. In those cases linear models are efficient and provide good approximations. A contradiction is therefore inevitable as point-absorbers are designed to induce large motions to optimise the energy generation. Many cases and operating conditions are therefore by nature nonlinear. Hence, it is important to have an understanding of which hydrodynamic effects are dominating in different load situations and where it is necessary to model effects of higher order. The main focus of the numerical assessment is to evaluate the impact of nonlinear Froude-Krylov and hydrostatic forces. That is essentially done by accounting for the instantaneous wetted body surface, instead of the mean wetted surface used in a linear analysis. A secondary objective is to evaluate the impact of the geometrical shape of a point-absorber with respect to absorbed power.

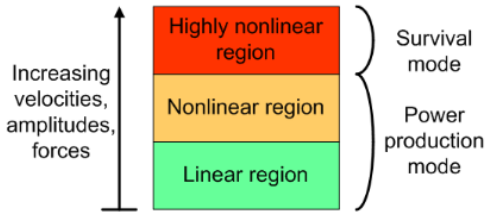

Figure 1: Different operating regions for wave energy devices. Retrieved from [49]

The thesis will firstly present the relevant theoretical background regarding linear and nonlinear potential theory. A brief introduction to the foundation of boundary element method(BEM) based software will also be given. Thereafter, a mathematical formulation of power absorption for a point-absorber will follow. The results and discussion regarding the numerical assessment will then be presented. The numerical simulations are separated into three categories:

- Chapter 4: Sphere
- Chapter 5: WEC float
- Chapter 6: Sphere, WEC float and Cylinder

The first two follows the cases from an ongoing project IEA OES Task10 [56] with two different geometries. The first regards a heaving sphere, with focus on assessing the effect

of weak nonlinearities in small and rather steep waves. The second considers a model scaled WEC float which is evaluated against experimental results from the Sandia Laboratiries[10] in linear conditions. Lastly, in chapter 6, three geometries are evaluated with main focus on absorbed energy. The thesis ends with a final conclusion and suggestions for further work.

1.1 Background and motivation

The outline of this master thesis was proposed by Dr. Ken-Robert G. Jakobsen at EDRMedeso, and is a continuation of a project thesis written in the fall of 2018. EDRMedeso have been a part of an ongoing project lead by the Ocean Energy Systems(OES) Task 10 Wave Energy Converter Modeling verification and validation group. The group was established under the OES Technology Network program under the International Energy Agency. OES was established in 2001, and the Task 10 project was proposed by Bob Thresher from the National Renewable Energy Laboratory(NREL) in 2015. Task 10 was approved by OES in 2016, and the first workshop took place in September of the same year. A total of 25 different organizations from 11 different countries participated.

Many numerical design tools today are potential theory codes, which are based on linear potential flow assumptions. These assumptions are often violated for WECs operating in resonance or are exposed to other nonlinear load conditions. Potential codes have been successfully utilized in other marine sectors such as Oil and Gas for decades. But how well do these codes perform for WEC's which by nature operates in rather nonlinear conditions? That is the main motivation behind the IEA OES Task10 project. Some of the objectives for the project includes

- Assessing the accuracy of, and establishing confidence in, the use of numerical models
- Validating a range of existing computational modelling tools
- Identifying simulation methodologies that will lead to reduced risk in technology development, improved WEC energy capture estimates, load estimates and reduced uncertainty in LCOE(levelized cost of energy) models
- Defining future research

The main focus of the first phase of the project was to validate different codes through code-to-code comparison. A floating sphere, restrained to move in heave only, was investigated. Three model configurations(fixed, free to move in heave and free to move in heave with external PTO damping) were tested in a set of regular and irregular wave conditions. The simple geometry and load cases were meant to ensure good understanding and comparable results between the codes. The sphere is by no means a simple geometry from a hydrodynamic aspect, but it is well-examined, easy to model correctly and therefore suitable for a code-to-code comparison study. Both fully linear, weak nonlinear and nonlinear codes participated, highlighting the impact of including/excluding higher order effects. A

joint reference paper presented on the European Wave and Tidal Energy Conference series(EWTEC) 2017[56] was written, which describes the process and results of the first phase. The aim of future phases is to increase in complexity and move towards more realistic WEC geometries and other WEC concepts. The second phase(IEA OES Task 10.2) is currently ongoing, and regards a model-scale point-absorber WEC, designed to provide dynamics ranging from mostly-linear for a single degree-of-freedom problem to increasingly nonlinear in multiple degrees-of-freedom [9]. The focus in this phase is validation with existing experimental data, retrieved from a testing campaign lead by Sandia National Labs. A more detailed description of the WEC model and the test cases are found later, in section 5.1. A paper of the second phase is under development.

The IEA OES Task10 project has been the inspiration for the majority of the simulations performed in this study. Investigation of the same geometry and test cases allowed for easy comparable results and validation, both with other codes and experimental data.

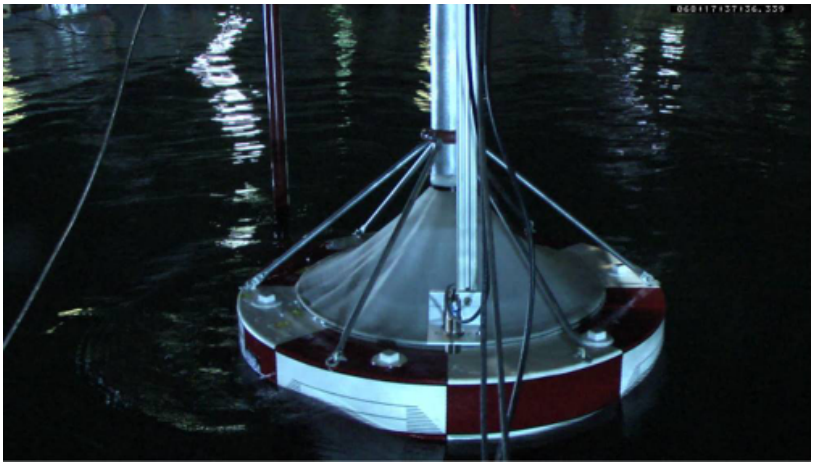

Figure 2: IEA OES Task 10.2 float geometry. The picture is retrieved from [10]

1.2 An overview of wave energy

History and development

The idea of extracting energy from waves is not new. Although it is not the first attempt to make use of energy from waves, the first known patent was filed by two Frenchmen in 1799 [3]. It was a shoreline device which intention was to use waves to pump fresh water to a nearby village. Ever since, the idea of generating energy from waves has led to a sporadic journey, with a lot of failures and set-backs, and some success-full achievements. Leishman and Scobie[41] estimated that over 340 patents on wave-powered generators were granted in Britain alone between 1856 and 1973, and that the rate of invention was highest in the early

1900's and up to the 1930's. The interest for utilization of wave energy slowly faded away during the interwar period as petroleum became the world's main energy source. However, history has shown that ocean energy solutions boom in times of oil crisis. A sudden increased interest in research and development regarding wave energy emerged in the aftermath of the oil crisis in 1973. Stephen Salter and Kjell Budal(1933-1989) initiated in 1973 research projects at universities in Scotland and Norway. In Norway, a research program was initiated at former NTH, Trondheim. Several universities and other institutions in Europe and the U.S followed in the next few years [24]. The oil price declined again in the early 1980's and consequently were the investments and focus regarding wave power drastically reduced[50]. Nevertheless, a first generation of prototypes were tested at sea and the scientific progress and development laid a lot of the foundation for later work. Even though several concepts were developed, no design emerged as an efficient and feasible solution. The main reason for this was the lack of successful large-scale implementations of the technology.

Another boom started in the mid 1990's, which we currently are at the end of. Several large-scale developments were initiated by countries like Portugal, Japan, India and Scotland. The world's first commercial wave energy device, Islay LIMPET,was installed in 2000 at the coast of Islay in Scotland, and connected to the United Kingdom's National Grid. In 2008 the first experimental, wave farm, the Aguçadoura Wave Farm, was opened 5km north of Porto in Portugal. It was however shut down two months after the opening. One might say that this paints a picture of the status of wave energy today. One strives to commercialize the industry, but there are still several issues to overcome. Today's research and development within the field of wave energy is driven by the need of low carbon and consistent energy solutions.

MAGNE

BARNEAFHOLDSBLAD

No. 12. | 16de juni 1901. | II. aarg.

Elektriske fyrbøier.

Du ved, der er en mægtig kraft i bølgeslagene. Selv om det er stille veir, saa er dog altid havbølgerne i bevægelse og kan hæve og sænke de største skibe. Nu har menneskene, som jo af Gud er sat til at herske over naturen og bruge dens kræfter i sin tjeneste, ogsaa fundet paa at bruge de kræfter, som ligger i bølgeslagene, til at fabrikere elektricitet, denne

en pumpe i bevægelse, og pumpen slynger en vandstrøm imod en turbin, og turbinen sætter en maskine igang, maskinen (dynamo kaldes den) frembringer elektricitet, og elektriciteten igjen et kraftigt lys.

Paa sjøen kan det være mørkt, og farlige banker, holmer og skjær truer skibene. Det er derfor godt at faa kraftige og kjendte

Figure 3: Front page of the Norwegian magazine Magne from 1901. The article suggested using energy from waves to light up electrical light buoys

The wave energy resource

The wave energy present in the worlds oceans origins from the sun. The varying distribution of sunlight over the earth's surface creates winds which travels from high pressure areas to areas of lower pressure. As the winds travel over the oceans, waves are created due to friction between the wind and sea surface. This is an energy source in order of terrawatts worldwide[15], which to date not has been commercialized. The transformation of energy from solar to wind to waves is an ascending chain of energy density. Ocean waves has in fact the highest energy density out of all presently known renewable energy sources, and it has the second largest energy potential among the ocean energy sources[36]. Although the waves has a high energy potential, the amount of extractable energy is limited. Opinions on the exact amount varies. Some studies regarded as conservative has estimated the amount of energy possible to exploit to be around 10-20% of the total potential [1]. This is however a considerable amount of the world's total power consumption[14]. Data from the International Renewable Energy Agency(IRENA) shows estimations of the wave energy resource potential in different parts of the world. These numbers are based on yearly average and represents an overview of the potential only.

Regions	Wave Energy Potential(TWh/y)
Mediterraniean Sea and Atlantic Archipelagos	1300
Central America	1500
Western and Northern Europe	2800
Africa	3500
North America and Greenland	4000
South America	4600
Australia, New Zealand and Pacific Islands	5600
Asia	6200
TOTAL	29500

Table 1: Theoretical Potential. Data from IRENA, retrieved from [1]

An important remark is that renewable energy sources complements each other. Areas with good conditions for ocean thermal energy aren't necessarily the same areas which contains a high amount of wave energy. In fact ocean thermal energy has a high potential along the equator, whilst the energy contained in the ocean waves are highest in latitudes 40-50 degrees [24]. This is connected with the solar power, and it's seen that in countries with a significant wave energy potential the solar energy tends to be less[6]. Moreover, wind and waves are traveling with different speeds and are consequently often present at different times. An advantage of wave energy is, according to Akar et al.[2], that the electricity power extraction is continuous 90% of the day, which for wind and solar are 20% and 30% in comparison. A combined utilization of these energy sources can therefore contribute to

more reliable and continuous electricity supply. A study by Mørk et al. [43] obtained the data illustrated in figure 4. It shows that the largest power levels in general occur along the west coast. In Europe, the largest power levels occur ouside Scotland and Ireland. The power level along the Norwegian coast is large as well, and the potential for utilizing wave energy is huge.

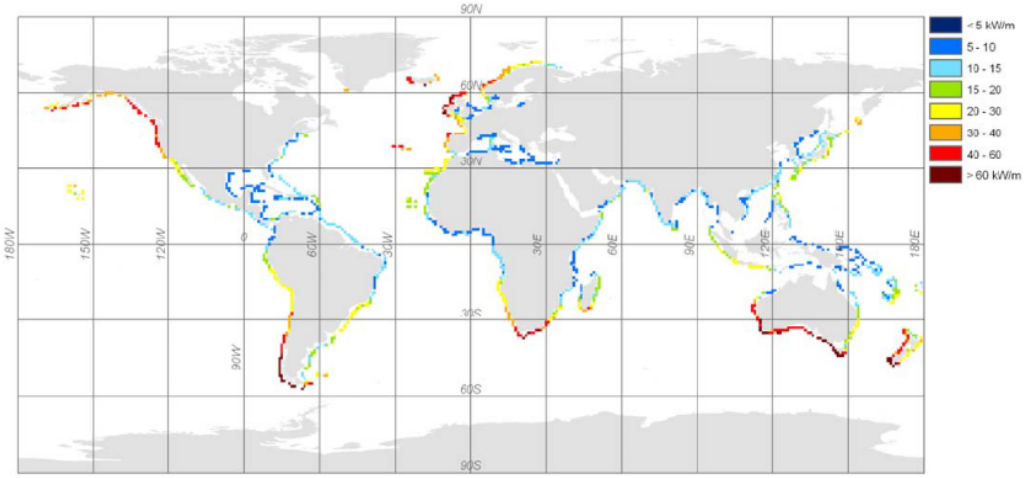

Figure 4: Annual net theoretical coastal power worldwide. Retrieved from [43]

Status of the wave energy industry today

Today one strives to commercialize the industry, making it competitive with other energy sources. Data from IRENA shows that ocean energy is much less utilized compared to other renewable resources such as hydropower, wind and solar energy(see figure 5). Ocean energy here includes wave energy, tidal energy, salinity gradient energy and ocean thermal energy. One of the issues which prevents commercial use is that it can be challenging to integrate the power from large WEC's into electricity grid due to the variable wave properties, referring to high variability in height, period and direction in both space and time. As a consequence of the wave energy not yet being commercialized, there are little grid facilities in areas where the wave resource is prominent, which makes it even more difficult to install large scale WEC's at desirable locations. Another issue is extreme weather. Extreme weather conditions influence the design of the construction, operations and provides challenges regarding the maintenance. Altogether, this makes it difficult to plan and harvest the energy.

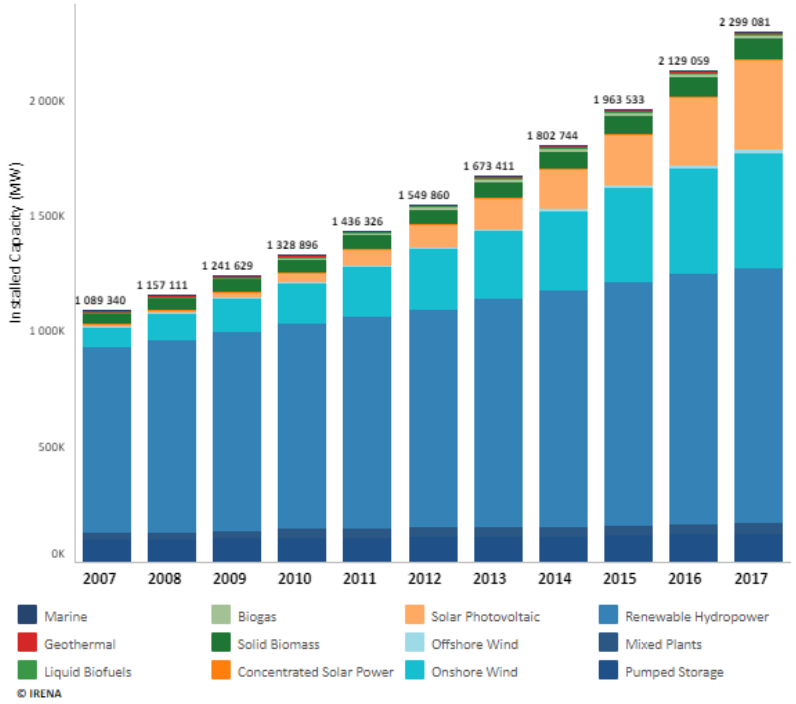

Figure 5: Trends in renewable energy. The plot shows installed capacity(MW) worldwide. Data from IRENA [37]

There are however countries which regardless has focused on development within wave energy. Numbers from the Annual Report Ocean Energy Systems 2016 [46] shows that the interest and awareness of the wave energy resource is increasing. Table 2 contains an overview of WEC installations around the world. Not all of the WEC's included in the table were yet commercialized.

Country	Planned	Installed	Operational	Total
Canada	0	0	11	11
New Zealand	0	20	0	20
Denmark	39	12	1	52
Italy	0	150	0	150
Mexico	200	0	0	200
Ghana	0	0	450	450
Spain	0	230	296	526
Korea	0	0	665	665
China	0	400	300	700
Portugal	350	0	400	750
United States	1335	500	30	1865
Sweden	0	0	3200	3200
Ireland	5000	0	0	5000

Table 2: Wave Energy Converters measured in kilowatt (kW). The numbers are valid as the end of 2016 and are retrieved from the Annual Report Ocean Energy Systems 2016[46]

Estimations from IRENA further indicates that approximately 10.3 million people worldwide were employed within the renewable energy sector in 2017. Out of these, a very small amount are working with wave energy. As can be seen in figure 6, the combined labour within tidal, wave and other ocean energy sources are the lowest out of all the listed ones. Although these numbers comes with an uncertainty related to them, it clearly reflects the fact that the industry not yet is commercialized. For wave energy technology to be commercialized, it's important to ensure recruitment of more people to contribute to research and development and to create awareness of the energy potential that the ocean waves contain.

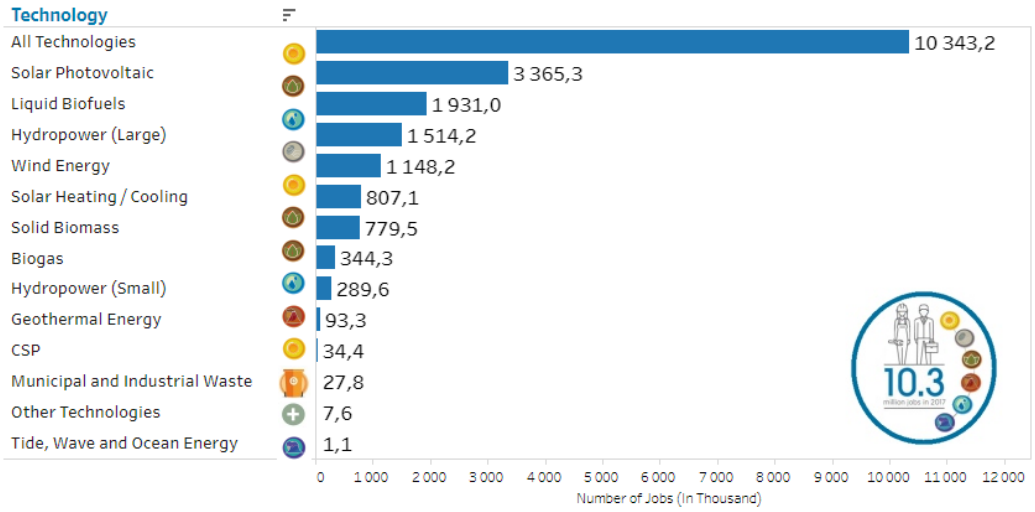

Figure 6: Number of jobs within each branch of renewable energy. The numbers origins from IRENA jobs database

Principles of extracting wave energy

There are several principal ideas of how to utilize the energy from waves. These different ideas leads to a vast variation of wave energy converters, referred to as a WEC. A wave energy converter is the device which harness energy from waves. There have been a lot of different WEC configurations throughout the years, and there are still a lot of ideas of how to efficiently extract the energy. There are mainly three categories of WEC devices

- Oscillating water column(OWT)
- Overtopping devices
- Wave activated bodies

The concept of the OWT is to use an oscillating water column inside a chamber to create a fluctuating air pressure which drives a turbine. Several different configurations based on this principle has been tested. The japanese naval officer Yoshio Masuda (1925–2009) is considered a pioneer within the wave energy technology, and used the principle of OWT to power a navigation buoy. The utilization of this technology has further developed, and one of the most famous concepts is "The Mighty Whale"[34], developed by the Japanese research group at the Japan Marine Science and Technology Center.

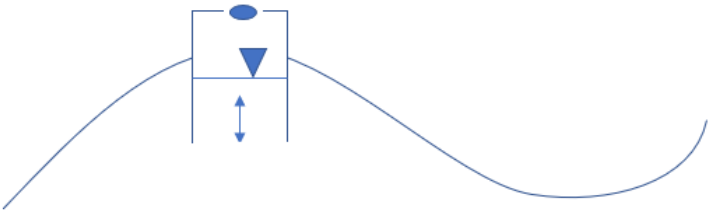

Figure 7: Principle sketch of an OWT configuration. The blue oval shape represents the turbine

The idea behind the second configuration, referred to as *Overtopping devices*, is to lead the waves into an ascending ramp and let the water overflow a certain threshold. The waves are led into a chamber which stores the water at a higher level than the free surface level. The potential energy created by the height difference can then be used to run a low headed hydraulic turbine[1]. Some concepts which are based on this technology today are Tapchan(tapered channel) [42] , Seawave Slot Cone Generator [55] and Wave Dragon[52].

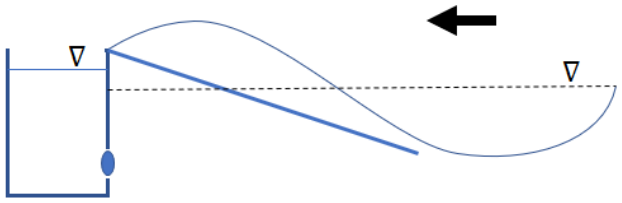

Figure 8: Principle sketch of an overtopping device.The blue oval shape represents the turbine

The third category(i.e wave activated bodies) includes all devices that are based on the principle of extracting energy from wave induced motions of a solid body. Several different ideas within this category have been explored. Two concepts are to exploit the relative motion between different parts of a system(multibody) or use the relative motion between a body and a fixed reference point(e.g at the seabed). Pelamis [58] is an example of the former. An advantage of these so called multibody solutions is that it avoids the challenge of having something react relative to a system at the seabed when the water depth is large. The PowerBouy [1] is an example of the latter, and is a heaving system where the motion relative to the seabed is used. Several other heaving motion concepts exists, and also concepts which uses oscillating modes in surge/sway and pitch. These types of methods are suitable in deep waters where the waves are powerful. They are most efficient when

[1] https://www.oceanpowertechnologies.com/powerbuoy

the body is oscillating in resonance with the ocean waves. This thesis will focus on a wave activated body configuration, and on a point-absorber in specific. The principle is illustrated in figure 9. Figure 10 contains an overview of some of the devices which have been developed throughout the years.

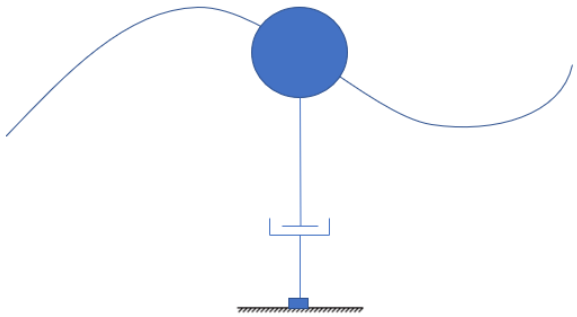

Figure 9: Principle sketch of a point absorbing buoy

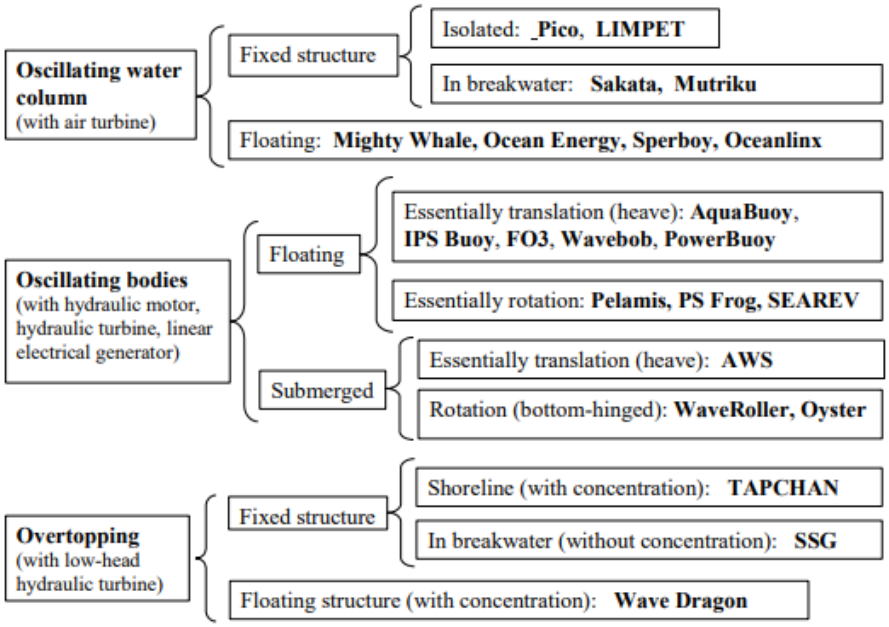

Figure 10: Overview of WEC devices throughout the years and until today. Retrieved form [19]

2 Numerical Model

This chapter will present the relevant mathematical theory necessary to describe the dynamic behaviour of a floating object in regular monochromatic waves. Two mathematical models will be presented which are based on the foregoing theory. A brief review of the software used to conduct the calculations is also included. It is expected that the reader has some knowledge within the field of linear and nonlinear potential theory and boundary element methods(BEM).

2.1 Theoretical background

2.1.1 Linear wave theory

The basic assumptions of linear wave theory, also known as Airy wave theory, is the assumption of homogeneous, incompressible, inviscid fluid and irrotational flow. The wave amplitude is further assumed to be small compared to the wave length and water depth. A natural starting point to introduce the theory is by looking at the velocity potential. The velocity potential, ϕ has turned out to be mathematically very convenient, and can be used to describe the fluid velocity vector $\mathbf{V}(x, y, z, t) = (u, v, w)$ at a time t in a point $\mathbf{X} = (x, y, z)$. The velocity in terms of the potential yields

$$\mathbf{V} = \nabla\phi \equiv \mathbf{i}\frac{\partial\phi}{\partial x} + \mathbf{j}\frac{\partial\phi}{\partial y} + \mathbf{k}\frac{\partial\phi}{\partial z} \tag{2.1}$$

where $\mathbf{i}$, $\mathbf{j}$ and $\mathbf{k}$ denotes the unit vectors along the x-, y- and z-axes. Conservation of mass for an incompressible fluid with constant density gives the relation $\nabla\cdot\mathbf{V} = 0$, also referred to as the continuity equation. By inserting equation (2.1) for $\mathbf{V}$ in the continuity equation, it follows that the velocity potential must satisfy the Laplace equation

$$\nabla^2\phi = 0 \tag{2.2}$$

The pressure p follows from conservation of momentum(i.e Navier-Stokes equation). When assuming inviscid fluid, the associated term of the Navier–Stokes equation is zero. The resulting conservation equation for the fluid momentum is known as the Euler equation

$$\frac{\partial\mathbf{V}}{\partial t} + \mathbf{V}\cdot\nabla\mathbf{V} = -\frac{p}{\rho} + \mathbf{g} \tag{2.3}$$

where ρ is the fluid density and g is the gravitational acceleration. With the assumption of irrotational fluid motion, the velocity vector can be expressed with the velocity potential, which results in the well known Bernoulli's equation

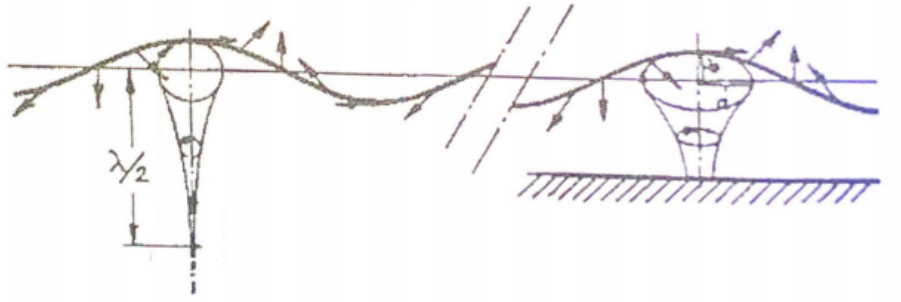

Figure 11: Movement of a water particle at the free surface in deep and finite water. Retrieved from [47]

$$p + \rho g z + \rho \frac{\partial \phi}{\partial t} + \frac{\rho}{2}|\nabla \phi|^2 = C(t) \tag{2.4}$$

where $C(t)$ is an arbitrary function dependent on time. The time dependence is included in the velocity potential, hence $C(t) \to C$. As a consequence of the assumptions made,the equation above is true for unsteady, irrotational and inviscid fluid motion [27].

Kinematic boundary conditions

For a moving body in a fluid the impermeability (no fluid enters or leaves the body surface) condition yields

$$\frac{\partial \phi}{\partial n} = \mathbf{U} \cdot \mathbf{n} \tag{2.5}$$

on the body surface. $\frac{\partial}{\partial n}$ denotes the differentiation along the normal of the body. $\mathbf{U}$ is any type of body motion. For a rigid body, $\mathbf{U}$ can be both translatory and rotary motions.

The kinematic boundary condition at the free surface states that a fluid particle on the free-surface remains at the surface, which is described by the following equation

$$\frac{\partial \zeta}{\partial t} + \frac{\partial \phi}{\partial x}\frac{\partial \zeta}{\partial x} + \frac{\partial \phi}{\partial y}\frac{\partial \zeta}{\partial y} - \frac{\partial \phi}{\partial z} = 0 \quad on \quad z = \zeta(x, y, t) \tag{2.6}$$

where $z = \zeta(x, y, t)$ is the free-surface. When assuming small wave height compared to length and water depth, the product of two terms are negligible. By a Taylor expansion one can transfer the free surface conditions from $z = \zeta(x, y, t)$ to the mean surface(i.e at $z = 0$). Thus, equation (2.6) can be abbreviated to

$$\frac{\partial \zeta}{\partial t} - \frac{\partial \phi}{\partial z} = 0 \quad on \quad z = 0 \tag{2.7}$$

Dynamic free-surface condition

The dynamic free-surface condition states that the water pressure on the free-surface is equal to the atmospheric pressure, p_0. By inserting p_0/ρ for C in Bernoulli's equation, then

$$g\zeta + \frac{\partial \phi}{\partial t} + \frac{\rho}{2}|\nabla \phi|^2 = 0 \quad on \quad z = \zeta(x, y, t) \tag{2.8}$$

By only keeping linear terms, and transform the condition from the free-surface position to the mean free-surface, equation (2.8) yields

$$g\zeta + \frac{\partial \phi}{\partial t} = 0 \quad on \quad z = 0 \tag{2.9}$$

Combined linear free-surface condition

By combining the kinematic and dynamic free surface condition(i.e combine (2.7) and (2.9)), a combined free surface equation can be written as

$$\frac{\partial^2 \phi}{\partial t^2} + g\frac{\partial \phi}{\partial z} = 0 \quad on \quad z = 0 \tag{2.10}$$

For a harmonically oscillating velocity potential in time, equation (2.10) can be expressed in terms of the circular frequency

$$-\omega^2 \phi + g\frac{\partial \phi}{\partial z} = 0 \quad on \quad z = 0 \tag{2.11}$$

Linear regular wave

By assuming a horizontal sea bottom and a free-surface of infinite horizontal extent one can express the Airy wave theory for propagating waves. Through implementation of the combined free-surface condition in the Laplace equation, the sea bottom condition is derived

$$\frac{\partial \phi}{\partial z} = 0 \quad for \quad z = -h \tag{2.12}$$

where h denotes the mean water depth. With the assumptions of ideal, irrotational fluid, a velocity potential which satisfies the linear free surface conditions, the impermeable bottom

condition and the Laplace equation in the whole fluid domain in finite water depth, can be expressed as

$$\Phi_0(\mathbf{X},t) = \phi_0(\mathbf{X})e^{-i\omega t} = -\frac{igζ_a cosh[k(z+h)]}{\omega cosh[kh]} e^{i[-wt+k(xcos(\theta)+ysin(\theta))+\alpha]} \tag{2.13}$$

where $\mathbf{X} = (x, y, z)$ denotes the location in the Cartesian coordinate system, ζ_a is the wave amplitude, ω is the wave frequency(rad/s), k is the wave number, θ is the wave propagating direction and α is the wave phase. For infinite water depth(h $\to \infty$), the velocity potential in (2.13) can be simplified to

$$\Phi_0(\mathbf{X},t) = \phi_0(\mathbf{X})e^{-i\omega t} = -\frac{igζ_a}{\omega} e^{i[-wt+k(xcos(\theta)+ysin(\theta))+\alpha]} \tag{2.14}$$

which is the equation of interest since the numerical simulation performed in this assignment assumes infinite water depth. The elevation of the water surface at a position (x, y) can then be found from the dynamic surface condition, and in complex notation be expressed as

$$\zeta = \zeta_a e^{i[-wt+k(xcos(\theta)+ysin(\theta))+\alpha]} \tag{2.15}$$

The relation between the wave frequency and the wave number(i.e the linear dispersion relation) is further described as

$$\omega^2 = kg\ tanh(kh) \tag{2.16}$$

The wave number, k, is expressed as $k = \frac{2\pi}{\lambda}$ where λ denotes the wavelength. The wave period, T is expressed as $T = \frac{2\pi}{\omega}$. For infinite water depth, the linear dispersion relation is simplified to

$$\omega^2 = kg \tag{2.17}$$

First order hydrostatic forces

The hydrostatic force on a floating body occur from the balance between buoyancy and gravity. The buoyancy of a partially or totally immersed body is the vertical upthrust from the displaced water:

$$F_B = \nabla \rho g \tag{2.18}$$

where ∇ is the volume of displaced water. When the body is in the equilibrium position in still water, the buoyancy force equals the structural weight of the body. More generally,

the hydrostatic force is the fluid force acting on the body in still water. It is calculated by integrating the pressure over the wetted surface in undisturbed conditions, which is embodied in the static term in Bernoulli's equation. In a fully-linear representation, the pressure integral considers the mean wetted surface S_0

$$F_{hys} = -\int_{S_0} p_s \mathbf{n} dS \tag{2.19}$$

where $p_s = -\rho g z$. From this expression a restoring force emerges when the body is moving. When a body is freely floating, the restoring forces acts on the body to bring it back to the equilibrium position. The restoring force can be represented by a hydrostatic stiffness(analogously to a spring), which in the case of a heaving body is proportional to the cross-sectional area at the still water level(SWL).

$$F_s = -C_{33} z = -\rho g A_{SWL} z \tag{2.20}$$

where A_{SWL} is the cross-sectional area at the still water level. The hydrostatic force in heave can then be expressed as [47]

$$F_{hys} = \nabla \rho g + \rho g A_{SWL} z \tag{2.21}$$

which consist of the hydrostatic buoyancy and restoring term. The linearitzation of the hydrostatic force provides a reasonably accurate approximation when the body motions are small.

First order hydrodynamic forces

When a freely floating body is present in the fluid domain, new effects arise. These factors are, due to linearity, separated into two problems; the radiation problem and the diffraction problem. The diffraction problem derives from the case where the floating body is held stationary and exposed to an incoming wave field. The diffraction problem considers the velocity potential of the incident wave field in the absence of the floating body, and the scattering velocity potential, which is scattering of the waves due to the body presence. The incident wave potential will be denoted ϕ_0, and is described above. The scattering velocity potential is denoted ϕ_7, and is referred to as the diffraction potential. The sum of the two loads corresponding to these two potentials gives the wave excitation loads. The contribution from the incident wave potential is known as Froude-Krylov loads, and the contribution from the scattered waves are known as diffraction loads.

In the radiation problem the body is forced to oscillate in otherwise still water, which generates waves that radiates away from the body. These waves are associated with the radiation velocity potential, ϕ_r, and is subjected to hydrodynamic loads identified as added mass, damping, and restoring terms. The restoring terms are related to the hydrostatic pressure(see(2.19)), whilst the damping and added mass are connected to the dynamic

pressure caused by the body motions. First order potential theory of diffraction and radiation waves allows for linear super-positioning of the velocity potential in the fluid domain. The flow field around a free floating body may be described by

$$\Phi(\mathbf{X}, t) = \zeta_a \phi(\mathbf{X}) e^{-i\omega t} \tag{2.22}$$

where $\phi(\mathbf{X})$ consists of the contribution from the radiated waves, diffracted waves and the incident waves. The velocity potential can therefore be written as

$$\phi(\mathbf{X}) e^{-i\omega t} = \Big([\phi_0 + \phi_7] + \sum_{j=1}^{6} \phi_{rj} \eta_j \Big) e^{-i\omega t} \tag{2.23}$$

where η_j for $j = 1, 6$ denotes the translational and rotational motions of the body. ϕ_0 is the first order incident wave potential, ϕ_7 is the corresponding diffraction potential, whilst ϕ_{rj} denotes the radiation wave potential due to the j-th motion. Although the potential functions are complex, the physical quantities such as fluid pressure and body motion in time domain analysis are obtained from the real part of the expression. The first order hydrodynamic pressure is obtained from the dynamic part of the linearized Bernoulli's equation

$$p^{(1)} = -\rho \frac{\partial \Phi(\mathbf{X}, t)}{\partial t} = i\omega\rho\phi(\mathbf{X}) e^{-i\omega t} \tag{2.24}$$

The first order hydrodynamic forces are obtained from integration of the pressure along the body surface, and can thus be written as

$$F_j e^{-i\omega t} = -\int_{S_0} p^{(1)} n_j dS \tag{2.25}$$

By inserting equation (2.23) and (2.24) into equation (2.25), the total first order hydrodynamic force can be further expressed as

$$F_j = F_{Ij} + F_{dj} + \sum_{k=1}^{6} F_{rjk} \eta_k \quad for \quad j = 1, ..., 6 \tag{2.26}$$

F_{Ij}, F_{dj} and F_{rjk} denotes the force due to incident wave, diffraction and radiation respectively. The forces due to the incident waves and diffraction yields

$$F_{Ij} = -i\omega\rho \int_{S_0} \phi_0(\mathbf{X}) \mathbf{n}_j dS \tag{2.27}$$

$$F_{dj} = -i\omega\rho \int_{S_0} \phi_7(\mathbf{X})\mathbf{n}_j dS \tag{2.28}$$

The j-th radiation force due to the unit amplitude of the k-th body motion can be expressed as

$$F_{rjk} = -i\omega\rho \int_{S_0} \phi_{rk}(\mathbf{X})\mathbf{n}_j dS \tag{2.29}$$

The added mass and radiation damping coefficient are embedded in the radiation force, and can be expressed by the velocity potential of the radiation problem. Equation (2.29) can be separated into a real part and an imaginary part

$$F_{rjk} = -i\omega\rho \int_{S_0} Re\big(\phi_{rk}(\mathbf{X})\big) + iIm\big(\phi_{rk}(\mathbf{X})\big)\mathbf{n}_j dS \;=\; \omega^2 A_{jk} + i\omega B_{jk} \tag{2.30}$$

where

$$A_{jk} = \frac{\rho}{\omega} \int_{S_0} Im[\phi_{rk}(\mathbf{X})]\mathbf{n}_j dS \tag{2.31}$$

$$B_{jk} = -\rho \int_{S_0} Re[\phi_{rk}(\mathbf{X})]\mathbf{n}_j dS \tag{2.32}$$

denotes the added mass and damping coefficients, respectively.

2.1.2 Second order forces and moments

The estimation of second order forces and moments are based on the same underlying assumptions as for liner theory; inviscid, incompressible, irrotational and homogeneous fluid. It is also assumed that the wave amplitude and the corresponding structural response are small. The major difference is that while in the linear solution, both the free-surface condition and the body boundary condition are solved at the linear free surface and at the mean wetted surface respectively, the second order solution accounts for the instantaneous body position, the wave profile along the body, and non-linearities in the fluid particle velocity at the free-surface[27]. The most common way to solve such nonlinearities in hydrodynamics is through application of perturbation analysis. With the above assumptions, the fluid potential, wave elevation, the position of the point on a structure and corresponding forces can be expressed with a perturbation approach. The principle of the this method is to expand a variable, y, into a convergent power series with respect to a small parameter, ε

$$y = \sum_{n=0}^{\infty} y^{(n)}\varepsilon^n \tag{2.33}$$

In accordance to classical hydrodynamic theory(see for example Pinkster[48]), it will be assumed that the velocity potential and other quantities such as wave amplitude and body motion, which are derivable from the flow, will be expanded in such a manner

$$\begin{aligned}\phi &= \varepsilon\phi^{(1)} + \varepsilon^2\phi^{(2)} + O(\varepsilon^3)\\ \zeta &= \zeta^{(0)} + \varepsilon\zeta^{(1)} + \varepsilon^2\zeta^{(2)} + O(\varepsilon^3)\\ \mathbf{X} &= \mathbf{X}^{(0)} + \varepsilon\mathbf{X}^{(1)} + \varepsilon^2\mathbf{X}^{(2)} + O(\varepsilon^3)\end{aligned} \tag{2.34}$$

where $\epsilon << 1$. The affix $^{(0)}$ then denotes the static value, while $^{(1)}$ and $^{(2)}$ denotes the first and second order variations, etc. Only higher order terms proportional to ε^2 will be considered. Contributions of higher order than second are denoted $O(\varepsilon^3)$, and are not discussed further. Before introducing the force and moment expression of second order, let's look at the motion and velocity of a point on the body surface when taking into consideration the perturbation methodology. If an object is moving with small amplitudes in six degrees of freedom due to oscillatory linear and second order waves, a point on the body relative to the OXYZ axis, referred to as the fixed reference axis(FRA), is

$$\begin{aligned}\mathbf{X}^{(0)} &= \mathbf{X}_g^{(0)} + \mathbf{x}\\ \mathbf{X}^{(1)} &= \mathbf{X}_g^{(1)} + \boldsymbol{\alpha}^{(1)} \times \mathbf{x}\\ \mathbf{X}^{(2)} &= \mathbf{X}_g^{(2)} + \boldsymbol{\alpha}^{(2)} \times \mathbf{x}\end{aligned} \tag{2.35}$$

$\mathbf{X}^{(0)}$ denotes the mean position vector, $\mathbf{X}^{(1)}$ is the first order oscillating vector and $\mathbf{X}^{(2)}$ is the second order motion vector. $\mathbf{X}_g^{(0)}$, $\mathbf{X}_g^{(1)}$ and $\mathbf{X}_g^{(2)}$ denotes the mean, first and second order of motion for the centre of gravity in the FRA. $\boldsymbol{\alpha}^{(1)}$ and $\boldsymbol{\alpha}^{(2)}$ denotes the first and second order angular motion vectors in the FRA, and $\mathbf{x}$ denotes a point on the body surface relative to the local structure axis(LSA). The velocity responces of that same point will then yield

$$\mathbf{V} = \dot{\mathbf{X}} = \varepsilon\dot{\mathbf{X}}^{(1)} + \varepsilon^2\dot{\mathbf{X}}^{(2)} \tag{2.36}$$

where

$$\begin{aligned}\dot{\mathbf{X}}^{(1)} &= \mathbf{V}^{(1)} = \dot{\mathbf{X}}_g^{(1)} + \dot{\boldsymbol{\alpha}}^{(1)} \times \mathbf{x}\\ \dot{\mathbf{X}}^{(2)} &= \mathbf{V}^{(2)} = \dot{\mathbf{X}}_g^{(2)} + \dot{\boldsymbol{\alpha}}^{(2)} \times \mathbf{x}\end{aligned} \tag{2.37}$$

Similarly, the acceleration is

$$\dot{\mathbf{V}} = \ddot{\mathbf{X}} = \varepsilon\ddot{\mathbf{X}}^{(1)} + \varepsilon^2\ddot{\mathbf{X}}^{(2)} \tag{2.38}$$

where

$$\begin{aligned}\ddot{\mathbf{X}}^{(1)} &= \dot{\mathbf{V}}^{(1)} = \ddot{\mathbf{X}}_g^{(1)} + \ddot{\boldsymbol{\alpha}}^{(1)} \times \mathbf{x}\\ \ddot{\mathbf{X}}^{(2)} &= \dot{\mathbf{V}}^{(2)} = \ddot{\mathbf{X}}_g^{(2)} + \ddot{\boldsymbol{\alpha}}^{(2)} \times \mathbf{x}\end{aligned} \tag{2.39}$$

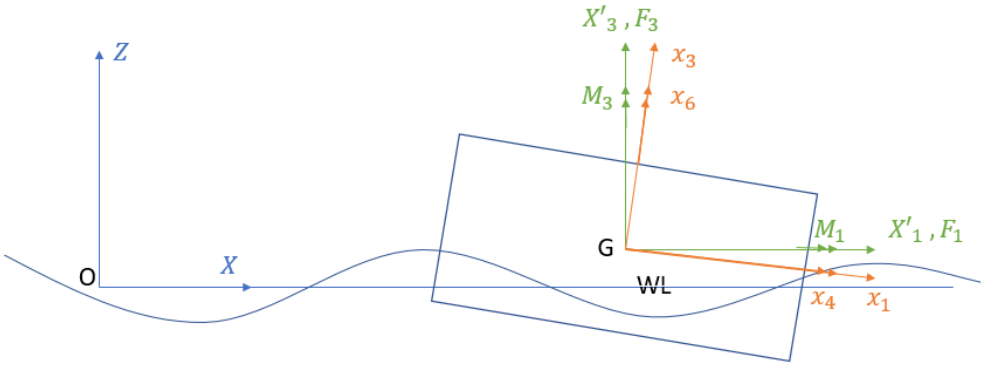

Figure 12: System of coordinates. The first system of co-ordinate axes is the fixed OXYZ system, which is referred to as the fixed reference axes(FRA) or global axes. The origin is located at the mean free surface, and is marked with blue in the figure. The second system of coordinates is the $Gx_1x_2x_3$ system, which is referred to as the local strucutre axis(LSA) or body fixed axes. The origin is located in the centre of gravity of the body. The axes through the origin will initially be parallel to the FRA when the body is in the mean position. It is marked with orange in the figure. The third system of co-ordinates is the $GX'_1X'_2X'_3$ system which has it's origin in the centre of gravity. It is at all times parallel to the fixed OXYZ system, and is marked with green in the figure.

The normal vector of a surface element on a structure in it's equilibrium position in still water relative to the $Gx_1x_2x_3$ axes is oriented outwards and denoted $\mathbf{n}$. Relative to the fixed co-ordinate systems, which are parallel at all times, the normal vector of a surface element is written as $\mathbf{N} = \mathbf{N}^{(0)} + \varepsilon\mathbf{N}^{(1)} + \varepsilon^2\mathbf{N}^{(2)}$ of which

$$\begin{aligned} \mathbf{N}^{(0)} &= \mathbf{n} \\ \mathbf{N}^{(1)} &= \boldsymbol{\alpha}^{(1)} \times \mathbf{n} \\ \mathbf{N}^{(2)} &= \boldsymbol{\alpha}^{(2)} \times \mathbf{n} \end{aligned} \tag{2.40}$$

Now the location of a position at the body surface and it's velocity and acceleration responses are defined, as well as the normal vector of a surface element up to the second order variation. Let's continue by evaluating the pressure at a point in the fluid. The fluid pressure at a given point can be described by Bernoulli's equation. By applying a Taylor expansion of the pressure, evaluated at the mean position, the following expression is valid

$$p = p^{(0)} + \varepsilon p^{(1)} + \varepsilon^2 p^{(2)} \tag{2.41}$$

where $p^{(0)}$ denotes the hydrostatic pressure, $p^{(1)}$ is the first order pressure and $p^{(2)}$ is the second order pressure.

$$\begin{aligned} p^{(0)} &= -\rho g Z^{(0)} \\ p^{(1)} &= -\rho g Z^{(1)} - \rho \frac{\partial \phi^{(1)}}{\partial t} \\ p^{(2)} &= -\frac{\rho}{2}|\nabla \phi^{(1)}|^2 - \rho \frac{\partial \phi^{(2)}}{\partial t} - \rho(\mathbf{X}^{(1)} \cdot \nabla \frac{\partial \phi^{(1)}}{\partial t}) - \rho g Z^{(2)} \end{aligned} \tag{2.42}$$

Notice that a quantity is of second order if it is proportional to ε^2, denoted by the affix $^{(2)}$, or if the component is the product of two first order quantities. Thus, it is seen that the second order pressure only contains one term with the second order velocity potential. The fluid forces and moments working on the body are found by direct integration of the pressure over the body surface. Unlike linear theory, the pressure is now integrated over the instantaneous wetted surface $S(t)$.

$$F(t) = -\iint_{S(t)} p\mathbf{N} dS \tag{2.43}$$

$$M(t) = -\iint_{S(t)} p(\mathbf{X} - \mathbf{X}_g)\mathbf{N} dS \tag{2.44}$$

One can divide the instantaneous wetted surface into two parts; a constant part, S_0, which goes up to the static waterline on the body surface and an oscillating part, s, between the static waterline and the wave profile along the body. By taking this into consideration and substituting the expanded expressions for the pressure and normal vector, one can write

$$\begin{aligned} F = &-\iint_{S_0} (p^{(0)} + \varepsilon p^{(1)} + \varepsilon^2 p^{(2)})(\mathbf{N}^{(0)} + \varepsilon \mathbf{N}^{(1)} + \varepsilon^2 \mathbf{N}^{(2)}) dS \\ &-\iint_{s} (p^{(0)} + \varepsilon p^{(1)} + \varepsilon^2 p^{(2)})(\mathbf{N}^{(0)} + \varepsilon \mathbf{N}^{(1)} + \varepsilon^2 \mathbf{N}^{(2)}) dS \\ = &\ F^{(0)} + \varepsilon F^{(1)} + \varepsilon^2 F^{(2)} + O(\varepsilon^3) \end{aligned} \tag{2.45}$$

The first term, $F^{(0)}$ is the hydrostatic force, the second term, $F^{(1)}$ is the total first order fluid force. The third term, $F^{(2)}$ is found by integrating all second order contributions over the constant and oscillating surface. The moments are expanded analogously. The total

second order wave exciting force and moment can then be described as(see Pinkster [48])

$$\begin{aligned} F^{(2)} =& -\frac{1}{2}\rho g \oint_{WL} \zeta_r^{(1)} \cdot \zeta_r^{(1)} \mathbf{n} dl \quad \text{Water line integral} \\ &+ \frac{1}{2}\rho \iint_{S_0} (\nabla\phi^{(1)} \cdot \nabla\phi^{(1)}) \mathbf{n} dS \quad \text{Bernoulli} \\ &+ \rho \iint_{S_0} \big(\mathbf{X}^{(1)} \cdot \nabla \frac{\partial \phi^{(1)}}{\partial t}\big) \mathbf{n} dS \quad \text{Acceleration} \\ &+ \boldsymbol{\alpha}^{(1)} \times F^{(1)} \quad \text{Momentum} \\ &+ \rho \iint_{S_0} \frac{\partial \phi^{(2)}}{\partial t} \mathbf{n} dS \quad \text{Second order potential} \end{aligned} \tag{2.46}$$

$$\begin{aligned} M^{(2)} =& -\frac{1}{2}\rho g \oint_{WL} \zeta_r^{(1)} \cdot \zeta_r^{(1)} (\mathbf{n} \times \mathbf{x}) dl \quad \text{Water line integral} \\ &+ \frac{1}{2}\rho \iint_{S_0} (\nabla\phi^{(1)} \cdot \nabla\phi^{(1)}) (\mathbf{n} \times \mathbf{x}) dS \quad \text{Bernoulli} \\ &+ \rho \iint_{S_0} \big(\mathbf{X}^{(1)} \cdot \nabla \frac{\partial \phi^{(1)}}{\partial t}\big) (\mathbf{n} \times \mathbf{x}) dS \quad \text{Acceleration} \\ &+ \boldsymbol{\alpha}^{(1)} \times M^{(1)} \quad \text{Momentum} \\ &+ \rho \iint_{S_0} \frac{\partial \phi^{(2)}}{\partial t} (\mathbf{n} \times \mathbf{x}) dS \quad \text{Second order potential} \end{aligned} \tag{2.47}$$

where $\zeta_r^{(1)}$ is the relative wave elevation. $F^{(1)}$ and $M^{(1)}$ are the total first order fluid force. This is the total second order fluid force and moment including the hydrostatic restoring, wave exciting and hydrodynamic radiation force and moment. These are however practically difficult to solve on this form . Thus, time independent quadratic transfer functions(QTF) are introduced. By means of quadratic transfer functions, it is possible to express the second order wave exciting forces in terms of force spectra in the frequency domain, or time histories of second order forces in the time domain. The total QTF can be split up into contributions arising from the five different terms described in equation (2.46) and (2.47). The first four terms, which are second order force terms due to being a product of first order components, can be evaluated based on three-dimensional linear potential theory(see section 2.1.3, Source distribution method). The last term is dependent on the second order velocity potential, which is found by solving the inhomogeneous free-surface boundary value problem

$$\phi_{tt}^{(2)} + g\phi_z^{(2)} = -\frac{\partial}{\partial t}(\phi_x^{(1)2} + \phi_y^{(1)2}\phi_z^{(1)2}) + \frac{1}{g}\phi_t^{(1)}\frac{\partial}{\partial z}(\phi_{tt}^{(1)} + g\phi_z^{(1)}) \quad on \quad z = 0 \tag{2.48}$$

The effect of current is here neglected. The subscripts denotes the quantity which the potentials are differentiated with respect to. To exemplify, $\phi_{tt}^{(2)} = \frac{\partial^2}{\partial t \partial t}\phi^{(2)}$. Finding the

solution to the second order potential is difficult due to the complexity of the free-surface boundary condition. In practice, approximations are often used. Aqwa applies Pinkster's approximation[48] to solve this potential. Note that $\phi^{(2)}$ does not contribute to mean wave drift force effects[27], and it is therefore not necessary to solve the second-order potential in those cases.

2.1.3 Source distribution method

The theory presented in this section is retrieved from Faltinsen [27], Pinkster [48] and the Aqwa Theory Manual[5]. ANSYS Aqwa applies a source distribution method to solve the diffraction and radiation velocity potentials described in equation (2.23). Note that this method applies for first order potentials. Thus, the affix $^{(1)}$ and $^{(2)}$ to distinguish between first and second order variations are not used here, as all potentials described below are of first order.

The technique is based on the use of point sources to derive an expression for the velocity potentials. A source is defined to have a velocity component in the radial direction only. The corresponding velocity potential at any point at a radial distance R from a point source in three dimensions in infinite fluid, is then defined as

$$\phi = \frac{-Q}{4\pi R} \tag{2.49}$$

where Q is referred to as the source strength. The idea is to discretize the body surface into smaller elements, and place a source in the centre of each of them. The potential function ϕ can now be represented by a continuous distribution of single sources on the surface. However, the source potential differs from equation (2.49) when wave effects are included. The velocity potential then has to fulfill the following boundary conditions

- The Laplace equation everywhere in the fluid domain Ω

$$\nabla^2\phi = 0 \tag{2.50}$$

- The linear free surface equation

$$-\omega^2\phi + g\frac{\partial\phi}{\partial z} = 0 \quad on \quad z = 0 \tag{2.51}$$

- The seabed surface condition

$$\frac{\partial\phi}{\partial z} = 0 \quad on \quad z = -h \tag{2.52}$$

or

$$|\nabla\phi| \to 0 \quad when \quad z \to -\infty \tag{2.53}$$

- The body boundary condition

$$\frac{\partial \phi}{\partial n} = -i\omega\eta_j \quad for \quad j = 1, ..., 6 \quad for \quad the \quad radiation \quad problem \tag{2.54}$$

$$\frac{\partial \phi}{\partial n} = -\frac{\partial \phi_0}{\partial n} \quad for \quad the \quad diffraction \quad problem \tag{2.55}$$

  on the mean wetted body surface, S_0

- The radiation condition

As a consequence, the source expression gets far more complicated, and the source density itself is actually complex in the wave problem. The representation of the potential function by a continuous distribution of sources on the boundary surface S_0, can be expressed on the form

$$\phi_j(\mathbf{X}) = \frac{1}{4\pi} \iint_{S_0} \sigma_j(\boldsymbol{\xi}) G(\mathbf{X}; \boldsymbol{\xi}; \omega) dS \quad for \quad j = 1, ..., 7 \tag{2.56}$$

The coordinates along the body surface are defined as $\boldsymbol{\xi} = (\xi, \eta, \zeta)$ while $\mathbf{X} = (x, y, z)$ are the coordinates in the fluid domain. $G(\mathbf{X}; \boldsymbol{\xi}; \omega)$ denotes Green's function of a source, which is singular in (ξ, η, ζ), and σ_j is the complex source strength. The Green's function is on the form

$$\nabla^2 G(\mathbf{X}; \boldsymbol{\xi}; \omega) = \delta(\mathbf{X} - \boldsymbol{\xi}) \tag{2.57}$$

where δ is the Dirac-Delta function. $G(\mathbf{X}; \boldsymbol{\xi}; \omega)$ is referred to as pulsating. A Green's function which fulfills the Laplace equation and the boundary conditions at the sea bottom, linear free surface and at infinity(radiation condition) is

$$\begin{aligned} G(\mathbf{X}; \boldsymbol{\xi}; \omega) = \frac{1}{r_1} + \frac{1}{r_2} + \int_0^\infty & \frac{2(k+\nu)e^{-kd} cosh\big(k(z+d)\big) cosh\big(k(\zeta+d)\big)}{k sinh(kd) - \nu cosh(kd)} J_0 kR dk \\ & + i2\pi \frac{(k_0+\nu)e^{-kd} cosh\big(k_0(z+d)\big) cosh\big(k(\zeta+d)\big)}{sinh(k_0+d) + k_0 d cosh(k_0 d) - \nu d sinh(k_0 d)} J_0 k_0 R \end{aligned} \tag{2.58}$$

where $r_1 = \big((x-\xi)^2 + (y-\eta)^2 + (z-\zeta)^2\big)^{\frac{1}{2}}$, $r_2 = \big((x-\xi)^2 + (y-\eta)^2 + (z+\zeta)^2\big)^{\frac{1}{2}}$ and $R = \big((x-\xi)^2 + (y-\eta)^2\big)^{\frac{1}{2}}$. J_0 is the Bessel function of the first kind of zero order, d is the water depth, $\nu = \frac{\omega^2}{g}$, k is the wave number and $k_0 tanh(k_0 d) = \nu$. Note that this function (2.58) satisfies the homogeneous free surface condition only, i.e not the second order free surface boundary condition. The unknown source strength funtion, σ_j is determined by satisfying the body boundary condition described in equation (2.54) and (2.55), where

$$\frac{\partial\phi(\mathbf{X})}{\partial n(\mathbf{X})} = -\frac{1}{2}\sigma(\mathbf{X}) + \iint_{S_0} \sigma(\boldsymbol{\xi})\frac{G(\mathbf{X};\boldsymbol{\xi};\omega)}{\partial n(\mathbf{X})}dS \quad where \quad \mathbf{X} \in \Omega \cup S_0 \tag{2.59}$$

Due to the linearization in which linear first order solutions are based on, this boundary condition is applied at the surface in it's equilibrium position, S_0. The Aqwa solver uses the Hess-Smith constant panel method[33] to solve the body boundary equation. The body can be discretized into quadrilateral or triangular panels and it's assumed that the source density is constant over each element. The discrete form of equation (2.56) and (2.59) can thus be expressed as

$$\phi(\mathbf{X}) = \frac{1}{4\pi}\sum_{m=1}^{N_p} \sigma_m G(\mathbf{X};\boldsymbol{\xi}_m;\omega)\Delta S_m \tag{2.60}$$

$$\frac{\partial\phi(\mathbf{X}_k)}{\partial n(\mathbf{X}_k)} = -\frac{1}{2}\sigma_k + \sum_{m=1}^{N_p} \sigma_m \frac{G(\mathbf{X}_k;\boldsymbol{\xi}_m;\omega)}{\partial n(\mathbf{X}_k)}\Delta S_m \quad where \quad \mathbf{X} \in \Omega \cup S_0 \tag{2.61}$$

N_p is the number of panels over the mean wetted body surface, ΔS_m is the area of the m-th panel, and $\mathbf{X}_k$ and $\boldsymbol{\xi}_m$ are the coordinates of the geometrical centre of the k-th and m-th panel respectively.

After the above equations are solved for the source strengths, the first order potential function is known. One can then evaluate the pressure over the surface and the first order wave exiting forces and moments as described in section 2.1.1. Finally, the first order motion response is calculated through the well known equation of motion in the frequency domain:

$$\sum_{j=1}^{6}\big(-\omega^2(M_{kj}+A_{kj})sin(\omega t+\varepsilon_j)+B_{kj}\omega cos(\omega t+\varepsilon_j)+C_{kj}sin(\omega t+\varepsilon_j)\big)\eta_{aj} = F_k sin(\omega t+\delta_k) \tag{2.62}$$

where M_{kj} is an inertia matrix, F_k denotes is the wave exited force in the k^{th} mode, and ε_j and δ_k are phase angles. η_{aj} is the amplitude of the oscillating motion given by $\eta_j = \eta_{aj}e^{-i\omega t}$.

2.2 Linear and weak nonlinear model

The theory presented above is quite substantial and briefly explained. In this study there are mainly two different methods to solve the equation of motion; a linear and a weak nonlinear one. This section will clarify exactly which nonlinear effects which are considered, and which terms that are remained linear throughout the study. The formulation of the methods are adopted from Retes et al.[49]. Let us start by looking at the governing equation of the problem. With the assumptions of linear theory described above, Newton's second law can be utilised to specify the following equation

$$m\ddot{x} = F_g - \iint_S p\mathbf{n}dS + F_{PTO} \tag{2.63}$$

where m is the body mass, x is the position of the body relative to the static equilibrium position and F_g is the gravity force, p is the total pressure acting on the surface and n is the normal vector pointing outwards. F_{PTO} denotes the force from the Power Take-off(PTO) system. As will be seen later, this term is modeled as a linear damper. In cases with no PTO force, this term is simply neglected. By separating the forces into each of the individual pressure integrals, i.e hydrostatic, incident wave, diffraction and radiation, the body motion can be expressed as

$$m\ddot{x} = F_S + F_I + F_d + F_r + F_{PTO} \tag{2.64}$$

where $F_S = F_g + F_{hys}$ is the hydrostatic restoring term. F_I is the force from the incident wave and F_d and F_r denotes the diffraction and radiation force respectively. F_S and F_I are often referred to as the static and dynamic Froude-Krylov force, respectively. To avoid any misunderstandings, F_S is referred to as the hydrostatic restoring force, and F_I as the incident wave or Froude-Krylov force. Each of these terms are previously described under the presentation of linear wave theory. Two different methods of solving this investigated; a linear method and a weak nonlinear model. The difference which distinguishes the two methods are that the weak nonlinear model considers nonlinear Froude-Krylov and hydrostatic forces.

A) Linear model

The linear method is based on the linear assumptions, and the problem is solved at the mean free surface, S_0. In this study a BEM tool(Aqwa) is used to solve the equation of motion in the frequency domain (2.62). This equation cannot be directly converted into the following equation in time domain if the external force is not periodic with constant amplitude [5]

$$M\ddot{x}(t) + B\dot{x}(t) + Cx(t) = F(t) \tag{2.65}$$

where M,B and C denotes the inertia, radiation damping and stiffness matrix respectively. For that reason, the equation of motion in time domain is in Aqwa solved with Cummin's equation[11]. It is a second order differential equation with a convolution integral. With his formulation, (2.64) can be written as

$$(m + A)\ddot{x} = -Cx - \int_{-\infty}^{\infty} K_{Ex}(t-\tau)\eta(\tau)d\tau - A_\infty\ddot{x} - \int_{-\infty}^{\infty} K_R(t-\tau)\dot{x}(\tau)d\tau - B_g\dot{x} \tag{2.66}$$

The hydrostatic restoring term $-Cx$ acts as a mass-spring system as described in (2.20). The excitation force is represented by a convolution integral between the excitation-impulse response matrix(K_{Ex}) and the surface elevation(η). The radiation force is expressed by the sum of the asymptotic added mass term($A_\infty\ddot{x}$) and the convolution integral between the radiation impulse-response matrix(K_R) and the velocity of the device. Lastly, it is seen that the PTO force is expressed by a linear PTO damping(B_g).

B) Weak nonlinear model

To improve the accuracy of the linear model, the Froude-Krylov and hydrostatic restoring terms are estimated nonlinearly by integrating the incident wave pressure and hydrostatic force over the instantaneous wetted surface,$S(t)$. The wetted surface will then vary with time and has to be re-calculated for each time step. The diffraction and radiation forces remains linear. Hence, only the second order variations for the incident wave and hydrostatic forces are calculated. Note that the second order potential is not solved. Second order and quadratic terms in the diffraction and radiation potential are neglected, as for any other linear model. Equation (2.64) can be written as

$$\begin{aligned}(m+A)\ddot{x} = F_g - \iint_{S(t)} P_s + P_I \mathbf{n} dS - \int_{-\infty}^{\infty} K_D(t-\tau)\eta(\tau)d\tau - A_\infty \ddot{x} \\ - \int_{-\infty}^{\infty} K_R(t-\tau)\dot{x}(\tau)d\tau - B_g\dot{x}\end{aligned} \tag{2.67}$$

The hydrostatic(p_s) and incident wave pressure(p_I) are integrated over the instantaneous wetted surface $S(t)$. The diffraction force is computed through the diffraction impulse-response matrix(K_D) and the free surface elevation η. It is still linear, but is now estimated independently of the incident wave force. The radiation and PTO force remains the same as for the linear method.

2.3 Software

ANSYS is a powerful multidicsiplinary tool which contains a broad portfolio of engineering simulation software. Aqwa is a module in ANSYS specialized in hydrodynamic analysis. It provides the possibility to investigate environmental loads on floating and fixed marine structures through implementation of three-dimensional radiation/diffraction theory, and/or Morison's equation in regular waves in the frequency domain. Aqwa can simulate first order (Airy wave) and second order regular waves (2nd order Stokes wave) in deep and finite depth water. Additionally, unidirectional or multi-directional irregular waves can be modeled by using the linear superposition approach, and it offers the possibility to include wind and current loads. See the Aqwa Theory Manual[5] for further information.

ANSYS Discovery SpaceClaim is the CAD tool used to create the model geometry. It is a 3D modeling application providing efficient solutions to common modeling tasks, and which is directly compatible with the Aqwa solver.

2.3.1 Mesh generation

Aqwa contains a buildt-in mesh generator, which automatically generates a mesh based on maximum element size and defeaturing tolerance defined by the user. The defeaturing tolerance controls how small details shall be treated in the mesh. For details smaller than

this user defined limit, one element can span over it. Otherwise, the element size will reduce in this area to ensure the feature is meshed properly. When a mesh is created in Aqwa, an interior, imaginary set of panels are introduced, referred to as the internal lid method. The reason is that in cases of surface piercing bodies, irregular frequencies in unsteady hydrodynamic analysis can occur. That causes errors in the solution for a frequency band of considerable size around these frequencies, which Du et al.[12] showed, leads to abrupt and inaccurate variations in the calculation of hydrodynamic coefficients. The internal lid method is applied to avoid these numerical problems. This method will not be be discussed in detail here, other than that it is based on creating a fluid field inside the surface S_0, which satisfies the same free-surface boundary condition as the floating body. The interior imaginary surface is discretized into a number of imaginary panels, denoted N_{Lid}. Thus, the potential function described in equation (2.56) is extended to include integration of the source distribution over the mean wetted surface, S_0, and the imaginary fluid bounded by S_0. All panels included in the source distribution integration is referred to as diffracting panels. The number of diffracting panels is denoted $N_{dif} = N_p + N_{Lid}$, where N_p is the number of panels on S_0 and N_{Lid} is the number of panels used to discretize the imaginary fluid interior of S_0.

Furthermore, Aqwa applies a mesh quality check to ensure sufficient element distribution, size and shape. The following criteria has to be fulfilled:

- The surface has to be represented by triangular and/or quadrilateral panels, and the normal of each panel must point out towards the surrounding fluid.
- The body surface has to be fully covered with panels without any gaps or overlaps between the elements.
- In the source distribution method described in section 2.1.3, the mean wetted body surface is required to perform frequency domain analysis. In cases of nonlinear time-domain analysis, the body surface above the mean water level may be necessary to include. In these cases, it's required that no panel cuts the mean water surface. It's further required that each panel fulfills the following requirements
  - The area of each panel should be nearly similar to all adjacent elements

$$\frac{1}{3} \leq \frac{\Delta S_m}{\Delta S_k} \leq 3 \quad where \quad m = 1, ..., N_p + N_{Lid} \tag{2.68}$$

    ΔS_m is the panel area of the m-th panel and ΔS_k is the panel area of any adjacent element.

  - The aspect ratio of each panel should not be too low

$$C\frac{\Delta S_m}{L_{max}} \geq \frac{1}{3} \quad where \quad m = 1, ..., N_p + N_{Lid} \tag{2.69}$$

    and L_{max} denotes the length of the longest side of the m-th panel. $C = 2.3$ for triangular elements and $C = 1.0$ for quadrilateral elements.

- The wave length should be large compared to the panel size

$$L_{max} \leq \frac{1}{7}\lambda \tag{2.70}$$

  where λ denotes the wave length

- The center of each panel has to be a certain range from any adjacent panel center

$$d_{mk} \geq r_{fm} \quad where \quad m = 1, ..., N_p + N_{Lid} \tag{2.71}$$

  where d_{mk} denotes the distance between the center of the m-th panel and the center of the adjacent panel. r_{fm} is the radius of the adjacent panel, defined as $r_{fm} = \sqrt{\frac{\Delta S_m}{\pi}}$

- There can't be any panel centers below the seabed. That is to avoid any singularities in Greens function described in equation (2.58). Thus, the center of any diffracting panel has to be above the seabed, ensured by

$$z_m + d \geq \frac{1}{2} r_{fm} \quad where \quad m = 1, ..., N_p \tag{2.72}$$

  where z_m denotes the z-coordinate of the m-th panel, d is the water depth and r_{mf} is the panel radius described above.

3 Wave energy

3.1 Absorption of waves is generation of waves

To understand the principle behind a point-absorbing buoy, it is important to note that the term absorbing wave energy is equivalent to removing or stealing energy from the ocean waves. The terms constructive and destructive wave interference are two types of wave interference extremities, illustrated in figure 13 with two sinusoidal waves with unit amplitude. There one can see that constructive interference amplifies the resulting wave, while the waves in destructive interference are canceled out. Let these waves represent any type of energy. As we all know, energy doesn't disappear. Hence, what figure 13b shows is that in the case of destructive interference, the energy is removed from the waves. This removed energy is what one tries to utilize and convert into electrical power.

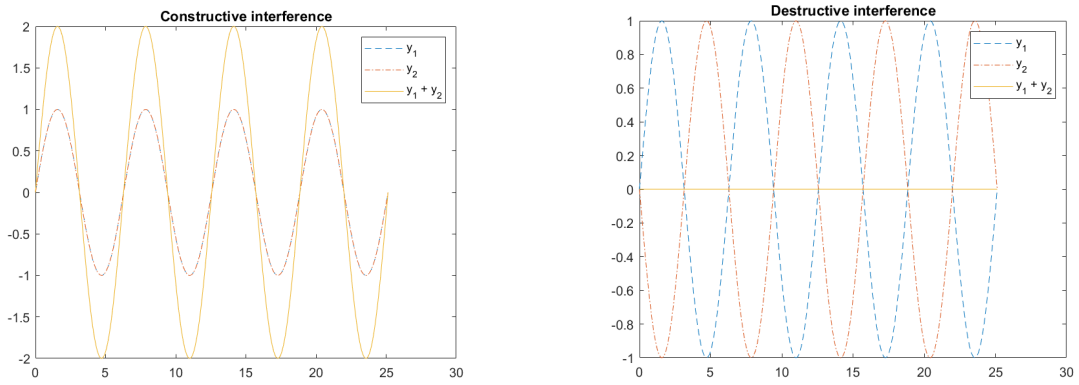

(a) (b)

Figure 13: Illustration of constructive(a) and destructive(b) interference between two sinusodial waves y_1 and y_2 with unit amplitude. In (a) y_1 and y_2 are in phase, while in (b) y_1 and y_2 are 180 °out of phase

Thus, to absorb wave energy one somehow need to reduce or cancel the waves passing the wave energy device. Such a reduction can be achieved with an oscillating body configuration which creates waves in counter-phase with the incoming and/or reflected waves. In other words, the basic principle is to arrange for a WEC to generate waves which interferes destructively with the sea waves [7]. Budal and Falnes [25] illustrated (figure 14) the principle with an example where 100% power absorption is theoretically possible. Figure 14a represents an undisturbed incident wave. Figure 14b illustrates a symmetric wave generation due to a body oscillating in heave, while figure 14c is non-symmetric radiated waves due to pitch motion. 14d represents the super positioning of the three above. Fully absorption of the incident wave is possible in this two-dimensional case when the body is

oscillating vertically and horizontally in an optimum manner, which is illustrated in figure 14d. The radiated waves from case 14b and 14c cancel out towards the left, and amplifies towards the right. This amplification cancels out the incoming wave on the right hand side, i.e 100% of the wave is absorbed. Nevertheless, when a symmetric body generates fully symmetric waves through one mode of motion only(14b), it can be shown that it is theoretically possible to only absorb up to 50% of the incident wave energy. This upper limit also applies for a symmetric body radiating anti-symmetric waves(14c). However, when a sufficiently anti-symmetric body is restricted to oscillate in one mode, it's possible to exceed the 50% limit, and extract almost all of the incident wave energy. The principle of an anti-symmetric geometry was investigated by Stephen Salter at the University of Edinburgh, resulting in the device known as the Duck [51], which came rather close to ideal conditions. This was the origin of the concept "Salter's Duck", which many later ideas have been based on.

While Salter's concept is based on a anti-symmetric body configuration fixed to one mode of rotation, this thesis will focus on a axisymmetric point-absorber fixed to oscillate in heave, which principle is illustrated in figure 9. The heave motions of the buoyant relative to the base is converted into electrical power by directly transmitting the motions to a Power Take Off(PTO) system. The PTO system is the part of the device which uses the relative motion to generate electricity. The PTO system applies an extra damping to the oscillatory motion, which is equivalent of absorbing energy. Models of a point absorber with a non-linear PTO system has shown to give quite accurate results compared full-scale experiments(see e.g. [17]). This thesis will for simplicity consider a linear PTO force.

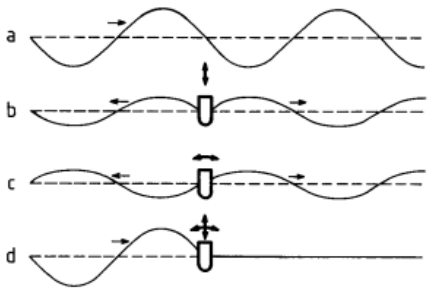

Figure 14: Illustration of two-dimensional interference: (a) represents an undisturbed incident wave; (b) illustrates a symmetric wave generation due to a body oscillating in heave; (c) non-symmetric radiated waves due to pitch motion; (d) superposition of the three above. Retrieved from [22]

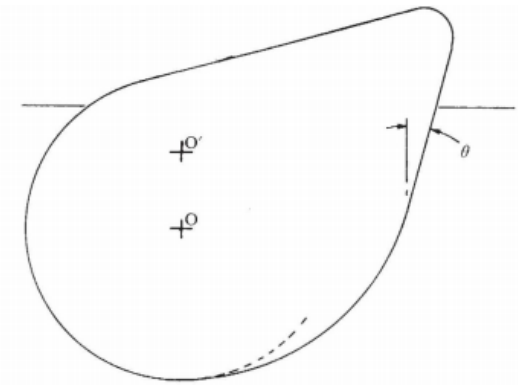

Figure 15: Principal sketch of the duck. Designed to rotate around O. Incoming waves from the right. Retrieved from [51]

3.2 Optimum energy absorption

Size

In terms of size, the fundamental idea is that the larger the buoy, the more volume can be used to displace the fluid and thus more energy can be absorbed. However, it is seen that this is not the case when the size of the buoy gets too large, as the diffraction forces starts to dominate[15]. Moreover, several proposals of large buoy configurations have had relatively large proportions of "dead" volume[24], volume which doesn't participate in the wave generation. The dimensions of the device are in fact often small compared to the wave length, and Budal and Falnes actually defined a point absorber buoy as a floating body with characteristic length much shorter than the length of the incoming waves [7]. One are not necessarily interested in the amount of power that is absorbed, but rather how much of the available power that is actually converted. Thus, the point absorber configuration has to be optimized in such a way that it absorbs as much power as possible from the incoming waves, where effects such as damping from the PTO and control system, size of the buoy and the systems inertia, has to be accounted for. These parameters, geometry, inertia and PTO damping are in fact the controllable parameters regarding the hydrodynamic behaviour of an oscillating body configuration.

Phase and amplitude

The body is ideally oscillating in resonance with the incoming waves, which is referred to as optimum destructive interference. In order to achieve this state of oscillation, the system needs to have optimum amplitude and optimum phase response. Optimum amplitude response for a given geometry can be found through estimating a proper PTO damping to the incoming wave loads. However, when considering a real sea state, several frequencies are present. Hence, an optimum amplitude response is not necessarily equivalent to maximum overall power production, as a small but large resonance peak merely covers a

fraction of all the frequencies in the sea state. Consequently, a wider an lower resonance peak might be better in terms of overall power production. The optimum phase response on the other hand, can be achieved through optimization of the draft. A WEC of reasonable size normally has an optimal phase response which lies outside the normal range of wave frequencies. This is a consequence of the low inertia of this type of configuration. Thus, by increasing the draft, one can increase the inertia until desired phase response is achieved. This is the foundation of a dilemma within point-absorbing buoys; an increased draft to improve the phase response reduces the amplitude response. Thus, in order to achieve both optimum amplitude response and optimum phase response, control mechanisms which forces the phase response to coincide with the incident waves have been developed.

Control methods

A method for controlling the motion of a point absorber configuration was independently suggested by Budal[8], French[28] and Guenter[31] in the 1970's, and is referred to as *latching*. The principle behind this method is to lock the body motion at the turning points of the oscillations(i.e at zero velocity), and then release the body when the velocity is in phase with the predicted excitation force from the incident ocean waves. Another, relatively new concept to increase the power capture is the use of a pneumatic machinery component referred to as WaveSpring. The component was invented at NTNU and a WEC which utilizes this idea is currently under development by the company CorPower Ocean [2]. The idea is based on reducing the heave-motion stiffness of the body and thus increase the response bandwidth. The component can be tuned to give both broad-banded response and resonance, as well as it can be detuned to decrease the response in high-energy sea states. An experimental laboratory test performed in 2014 [53] showed that, compared to pure linear damping, the WaveSpring unit typically gave a three-fold increase in delivered energy. This is of the same order as for phase control methods such as latching in terms of captured power. However, the required force from the machinery is less, which reduces PTO costs. The motion of the device is continuous, unlike the latching method which has a rather abrupt motion. This improves the lifetime, as it avoids the wear and fatigue challenges connected to such motions.

3.3 Mathematical description of wave energy extraction

This section contains a brief and step-wise mathematical description of the principle behind wave-energy extraction. A more thorough description can be found in Engstrøm, 2011[15] and Falnes, 2007[24].

[2] http://www.corpowerocean.com/corpower-technology/wave-spring-technology/

3.3.1 Active and reactive power. Exemplified with a linear mass-spring-damper system

In order to understand the mathematical principle behind extraction of wave energy, it's important to fully understand the concept of active and reactive power. Let's start by looking at the mass-spring-damping system described by a linear differential equation with constant coefficients

$$m\ddot{x}(t) + b\dot{x}(t) + cx(t) = F(t) \tag{3.1}$$

where a mass m is connected to a spring c and a mechanical damper, b. $F(t)$ represents an external force applied to the system. The overdot represents differentiation with respect to time. We shall now look at the mechanical power delivered to the oscillating system by the external force $F(t)$, and how this energy exchanges between absorbed or consumed energy in the damping resistance b, and the kinetic and potential energy stored in the spring c. The mechanical power delivered by the external force $F(t)$ is

$$P(t) = F(t)u(t) = F(t)\dot{x} \tag{3.2}$$

where

$$F(t) = F_m(t) - F_b(t) - F_c(t) = m\ddot{x}(t) + b\dot{x}(t) + cx(t) \tag{3.3}$$

The mechanical power can now be described as

$$P(t) = P_R(t) + [P_k(t) + P_p(t)] \tag{3.4}$$

where

- $P_R = -F_b\dot{x} = b\dot{x}^2$ is the power delivered to the mechanical damper
- $P_k(t) = F_m(t)\ddot{x} = m\ddot{x}\dot{x}$ is the power delivered to the mass
- $P_p(t) = -F_c(t)\dot{x} = c\dot{x}\dot{x}$ is the power delivered to the spring

Thus, when looking at equation (3.4), one can say that the delivered power consists of two components; 1) $P_R(t)$ which is consumed by the system's damping resistance and is referred to as the instantaneous active power, and 2) $P_k(t) + P_p(t)$ which exchanges between the stored kinetic energy in the mass and stored potential energy in the spring, and is referred to as the instantaneous reactive power. We shall further look at active and reactive power with harmonic oscillations. Let's start by defining an sinusoidal oscillation as

$$x(t) = x_0 cos(\omega t + \theta) \tag{3.5}$$

where x_0 is the amplitude, ω is the angular frequency and θ is a phase angel. The complex amplitude is here denoted with a hat, and yields

$$\hat{x} = x_0 e^{i\theta} \tag{3.6}$$

This can be used to express $x(t)$ on a complex form as

$$x(t) = \frac{\hat{x}}{2}e^{i\omega t} + \frac{\hat{x}}{2}e^{-i\omega t} \tag{3.7}$$

By assuming that the delivered power is harmonically oscillating, and applying the identity above, the expression in equation (3.2) can be expanded as follows

$$\begin{aligned} P(t) = F(t)u(t) &= \Big(\frac{\hat{F}}{2}e^{i\omega t} + \frac{\hat{F}^*}{2}e^{-i\omega t}\Big)\Big(\frac{\hat{u}}{2}e^{i\omega t} + \frac{\hat{u}^*}{2}e^{-i\omega t}\Big) \\ &= \frac{1}{4}(\hat{F}\hat{u}^* + \hat{F}\hat{u}^* + \hat{F}\hat{u}e^{2i\omega t} + \hat{F}^*\hat{u}^*e^{-2i\omega t}) \end{aligned} \tag{3.8}$$

where $\hat{F}^*$ and $\hat{u}^*$denotes the complex conjugate of $\hat{F}$ and $\hat{u}$. The reason for this expansion is that one can now see that the last two terms are harmonically oscillating with a frequency 2ω, and are complex conjugates of each other. When taking the time-average during one period of oscillation of the delivered power, the sum of these last two terms is zero. Thus, one can write the time-average delivered power as

$$P \equiv \overline{P(t)} = \frac{1}{2}Re(\hat{F}\hat{u}^*) \tag{3.9}$$

Note that one takes the real part of the expression to obtain the physical power. To give more meaning to the above equation, we shall introduce the mechanical impedance. Impedance in general is the complex generalization of resistance, and the mechanical impedance is a measure of a structures ability to resist motion when subjected to a harmonic force. It relates the forces and velocities acting on the mechanical system. The mechanical impedance can be expressed through the following relation

$$F(\omega) = Z(\omega)u(\omega) \tag{3.10}$$

where $Z(\omega)$ denotes the impedance. It's a complex value, where the real part is the resistance and the imaginary part is the reactance, here denoted R and X respectively.

$$Z = R + iX \tag{3.11}$$

In other words, the real part represents the resistive effect and the imaginary part represents the reactive effect. Let's take a short digression to set this into a hydrodynamic context; the mechanical impedance can be related to the radiation problem when evaluating an oscillating body in waves, and can be expressed as[4]

$$Z = R + iX = -i\omega\rho \int_{S_0} \phi_{rk}\mathbf{n}_j dS = B_{jk} + i\omega A_{jk} \tag{3.12}$$

Thus it is seen that R and X are directly related to the radiation damping and added mass respectively. Back to the mass-spring-damper system; when relating (3.11) to the mass-spring-damper problem described in (3.1), the resistance is $R = b$ and reactance

$X = \omega m - \frac{c}{\omega}$. Now, inserting the impedance into equation (3.9), the time-average delivered power yields

$$P \equiv \overline{P(t)} = \frac{1}{2} Re(\hat{Z}\hat{u}\hat{u}^*) = \frac{1}{2} b|\hat{u}|^2 \tag{3.13}$$

Note that the real part of Z includes the damping coefficient only. We continue by looking at the consumed power P_R described above. By following the same logic as for the time-average delivered power, one can derive an expression for the time-average consumed power as

$$P_R = \overline{P_R(t)} = \frac{1}{2} b|\hat{u}|^2 = \overline{P(t)} \tag{3.14}$$

Thus, consumed and delivered power is equal when time-averaged. This is not the case for the instantaneous values, hence generally $P(t) \neq P_R(t)$. However, the important remark here is that the time-average of the active power, P_R, describes the average power taken up in the system by the delivered power P. The reactive power simply describes the energy exchanging between kinetic and potential, and therefore contributes zero to the average power taken up by the system. When relating this to wave energy conversion, the time-average or mean power absorbed by a WEC corresponds to the mean power consumed by the mechanical damper of the PTO system during one wave period.

3.3.2 Oscillating body in one mode in regular waves

The underlying principle of energy and power relations in the mass-spring-damper system described above are the same as for a system consisting of a body subjected to harmonic ocean waves. The mathematical description is for simplicity based on a oscillating body in one mode only(e.g. heave), and the notation used is adapted from Falnes[24]. Both the waves and oscillations are assumed small in order for linear theory to be applicable. The dynamic equation governing the problem can be described by Cummin's equation[11]. In this case, when the movement of the structure is generated by the incident waves only, the Cummin's equation is a second order differential equation with a convolution integral in it. An additional damping term due to mechanical losses in the machinery is also included, which results in the following dynamic equation[20]

$$(m + A_{r\infty})\ddot{x}(t) + B_f\dot{x}(t) + k_r(t) * \dot{x}(t) + Cx(t) = F_e(t) + F_u(t) \equiv F_{ext}(t) \tag{3.15}$$

where m is the body mass, C is the restoring-force coefficient, F_e is the excitation force due to incoming waves and F_u is an intentionally applied force from the control and PTO system. The added mass is denoted $A_r(w)$, and $A_{r\infty}$ is the asymptotic value when $\omega \to \infty$, i.e $A_{r\infty} = A_r(\infty)$. B_f is the damping from mechanical loss due to for example friction and viscosity. This contribution is referred to as the loss force, denoted $F_f(t) = -B_f\dot{s}(t)$, which in in this case is simplified and could for a more realistic approach be replaced with a non-linear loss force. The sign $*$ represent the mathematical operation of convolution.

Furthermore, $k_r(t)$ is the impulse-response function for the radiation force, which is zero for all $t < 0$. It is the inverse Fourier transform of $K_r(\omega)$, which is written as

$$K_r(w) = Z_r(\omega) - i\omega A_{r\infty} = B_r(\omega) + i\omega(A_r(\omega) - A_{r\infty}) \tag{3.16}$$

where $Z_r(\omega)$ is the mechanical(or radiation) impedance(see (3.12)) and B_r is the radiation damping coefficient. The last term of the expression, which regards the added mass is often denoted by $iD(\omega)$. Thus, by implementing this into $K_r(w)$ and take the Fourier Transform, $k_r(t)$ can be separated into $k_r(t) = b_r(t) + d_r(t)$ where $b_r(t)$ contains the contribution from the radiation damping and $d_r(t)$ from the added mass. The dynamic behaviour described by equation (3.15) can now be written in a more compact way with the impulse response function $g_i(t)$

$$g_i(t) * s(t) = F_e(t) + F_u(t) = F_{ext} \tag{3.17}$$

where

$$g_i(t) = B_f\dot{\delta} + \dot{b_r}(t) + \dot{d}_r(t) + (m + A_{r\infty})\ddot{\delta(t)} + C\delta(t) \tag{3.18}$$

$\delta(t)$ is the Dirac-Delta function and $g_i(t)$ is zero for $t < 0$. Each term in the dynamic equation describes a force. Thus, the power can be found by multiplying each term by the velocity $\dot{x}(t)$. The instantaneous power delivered to the PTO and control system, $P_u(t)$, can then be found as

$$P_u(t) \equiv -F_u(t)\dot{x}(t) = P_b(t) + P_d(t) \tag{3.19}$$

where $P_b(t)$ is the instantaneous active power and yields

$$P_b(t) = F_e(t)\dot{x}(t) - \big[b_r(t) * \dot{x}(t)\big]\dot{x}(t) - B_f(\dot{x}(t))^2 \tag{3.20}$$

P_d is the instantaneous reactive power, and can be written as

$$P_d(t) = -(m + A_{r\infty})\ddot{x}(t)\dot{x}(t) - \big[d_r(t) * \dot{x}(t)\big]\dot{x}(t) - Cx(t)\dot{x}(t) \tag{3.21}$$

An important remark is that, as explained in section 3.3.1, the reactive power doesn't contribute to the average power delivered to the PTO system. The active power, $P_b(t)$, contains all the resistance (or damping) terms. The instantaneous reactive power, $P_d(t)$, simply describes how the stored energy exchanges between the machinery(PTO and control system) and the moving oscillatory system. By time-averaging the instantaneous active power over a time interval, one can find the average power delivered to the PTO and control system

$$P_u \equiv \overline{P_u(t)} = \overline{P_b(t)} = \overline{F_e(t)\dot{x}(t)} - \overline{\big[b_r(t) * \dot{x}(t)\big]\dot{x}(t)} - \overline{B_f(\dot{x}(t))^2} \tag{3.22}$$

The actual wave absorption lies within the two first terms. The third term contains the damping coefficient B_f which is the mechanical loss resistance. One can write the absorbed power with the first two terms as $P_a = \overline{F_e(t)\dot{x}(t)} - \overline{\big[b_r(t) * \dot{x}(t)\big]\dot{x}(t)}$, where the radiated power is subtracted from the power from incident wave forces. Falnes writes that "one should note think of this as a loss of energy, but a necessity"[24]. By this he refers to the principle that the equivalent of absorbing wave energy is to generate waves which interferes destructively with the incident waves.

3.3.3 Estimation of optimum PTO damping coefficient

The dynamic equation describing a floating buoy oscillating in 1DOF was described in the time-domain by Cummin's equation. When evaluating the force from the PTO system, it is practical to express the equation of motion in the frequency domain, as the force is represented with a frequency dependent damping coefficient, B_g. It is assumed that the mooring force is sufficiently small to be neglected, and that the PTO force is linear, that is, it is proportional to the vertical buoy velocity as described in (3.2). The frequency domain transformation of Cummin's equation is often referred to as the Ogilvie equation, which for uncoupled heave motion and with additional PTO damping yields

$$X(i\omega) = \frac{F_{ext}(i\omega)}{-\omega^2(m + A_{33}) + i\omega(B_{33} + B_g) + C_{33}} \tag{3.23}$$

When speaking in wave energy terms, X is referred to as the capture displacement. This can be rewritten in terms of the velocity in heave, U, which gives

$$U(i\omega) = \frac{F_{ext}(i\omega)}{i\omega(m + A_{33}) + (B_{33} + B_g) + C_{33}/i\omega} \tag{3.24}$$

From (3.14) it is seen that the time-averaged useful power absorbed by the PTO is dependent on the damping coefficient due to the PTO and the square of the velocity. By substituting the velocity, the time-averaged absorbed power can be expressed as

$$\overline{P_u} = \frac{1}{2} B_g \left|U(i\omega)\right|^2 = \frac{1}{2} \frac{B_g F_{ext}(\omega)^2}{(B_{33} + B_g)^2 + (\omega(m + A_{33}) - (C_{33}/\omega))^2} \tag{3.25}$$

To maximise the amount of absorbed energy one can estimate the optimal PTO damping through following optimum condition; $\frac{\partial \overline{P_u}}{\partial B_g} = 0$(see [38]). The optimum PTO damping coefficient is then found to be

$$B_{g,opt} = B_{33}\sqrt{1 + \Big(\frac{C_{33} - \omega^2(m + A_{33})}{\omega B_{33}}\Big)^2} \tag{3.26}$$

This damping coefficient is the input utilized by Aqwa to simulate the optimum PTO force. Note that $B_{g,opt}$ indicates that the optimum damping is independent of the wave height. The time-averaged absorbed power can further be expressed as [54]

$$\overline{P_{u,opt}} = \frac{\left|F_{ext}\right|^2}{4(B_{33} + B_{g,opt})} \tag{3.27}$$

which is at it's maximum at resonance, i.e $B_{g,opt} = B_{33}$. The maximum absorbed power is therefore

$$\overline{P_{u,max}} = \frac{\left|F_{ext}\right|^2}{8B_{33}} \tag{3.28}$$

at resonance, which suits with previous and well known results(see for example Evans[18]).

3.3.4 Energy in waves and theoretical limitations of absorption

The energy in surface gravity waves consists of potential energy which arises from the wave elevation and kinetic energy due to the fluid motion. For harmonic waves in deep water, the total amount of energy can be retrieved from the power spectrum of the waves

$$E = \rho g \int_0^\infty S(f) df \tag{3.29}$$

where $S(f)$ denotes the wave spectrum as a function of the frequency, f. The wave power spectra is a way of representing the wave elevation. It is defined as

$$S(f) = \frac{2}{T_0} | \int_0^{T_0} \zeta(t) e^{2\pi f t} dt|^2 \tag{3.30}$$

where $\zeta(t)$ is the time-dependent wave elevation and T_0 denotes the total measured time. By including directions of the propagating waves, one obtains a directional wave specter. Convenient statistical information can be estimated through the power spectrum moments, defined as

$$m_n = \int_0^\infty f^n S(f) df \tag{3.31}$$

The significant wave height, $H_s = H_{m_0} = \sqrt{m_0}$ and the energy period $T_p = T_{-1,0} = \frac{m_{-1}}{m_0}$ are two examples of such statistics. The transportation of wave energy is denoted J and is the energy flux through a vertical wall of unit width. It's defined as

$$J = \rho g \int_{-\infty}^0 p u_x dz \tag{3.32}$$

where u_x is the particle velocity in the horizontal direction, and p is the pressure. The energy in sinusodial waves with period $T = 1/f$ is transported with the group velocity of the waves. Thus, one can express a relation between the energy end the energy transport as follows

$$J = c_g E \tag{3.33}$$

where c_g is the group velocity. From this relation one can further express the wave-power level(average energy transport) for a real wave in terms of the wave spectrum

$$J = \rho g \int_0^\infty c_g(f) S(f) df = \frac{\rho g^2}{4\pi} m_{-1} = \frac{\rho g^2}{64\pi} T_{-1,0} H_{m0}^2 \tag{3.34}$$

where $c_g = \frac{g}{4\pi f}$ in deep water. For a heaving, axisymmetric body exposed to harmonic waves, it can be shown[7] that the system can absorb at most

$$P_{max} = J\lambda/2\pi \tag{3.35}$$

where $\lambda = \frac{gT^2}{2\pi}$ is the wave length and T is the wave period. This corresponds to the optimum destructive interference for this geometry and motion. By inserting (3.34) and $\lambda = \frac{gT^2}{2\pi}$ into (3.35), the upper limit for absorbed power yields

$$P_A = c_\infty T^\delta H^2 \tag{3.36}$$

where H is the wave height, $c_\infty = \frac{1}{128}\rho(g/\pi)^3$ and $\delta = 3$[24]. There is also a theoretical upper bound due to the volume of the body, of how much power possible to absorb when in optimum destructive interference. It is dependent on the wave period and height [15] and yields

$$P_B = c_0 \frac{VH}{T} \tag{3.37}$$

where $c_0 = \pi\rho g/4$. V is referred to as maximum swept volume and is for a semi-submerged heaving buoy the difference between maximum and minimum water displacement. P_B is referred to as *Budal's upper bound*, and a derivation of this expression can be found in Falnes[21]. Together with the incident power from the incoming energy transport which is expressed as $P_c = LJ$, where L denotes the characteristic length of the body, it sets the upper limits for the energy absorption as illustrated in figure 16. These are theoretical values which holds for any axisymmetric body oscillating in heave. The actual amount of absorbed power is however unique for every system, and depends on the geometry, PTO damping, control system etc.

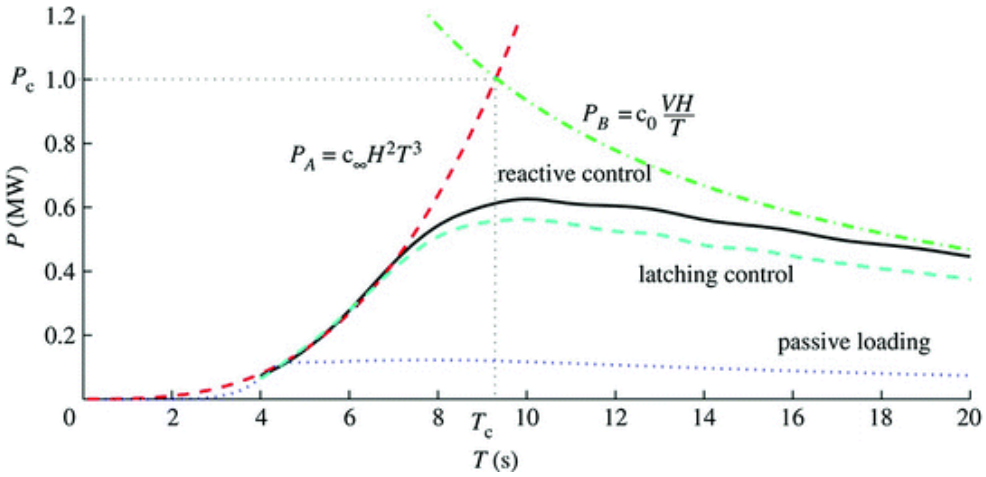

Figure 16: Budal diagram. Amount of power possible to absorb for a semi-submerged sphere exposed to a sinusoidal wave in optimum conditions for three different control techniques. In this specific case $H = 2.26m$, $V = 524m^3$ and deep water is assumed. Retrieved from [26]

4 Hydrodynamic assessment of a sphere

The numerical simulation performed with the sphere follows the cases from the first phase in the task 10 project; a free-decay test with different initial displacements and two different configurations in regular waves. The results of the numerical simulations are presented and discussed consecutively. Lastly a conclusive summary will follow. The main focus throughout the analysis is to investigate the difference between analysis with and without weak nonlinearities. Weak nonlinearities reffers in this case to the calculation of nonlinear hydrostatic and Froude-Krylov forces as described under section 2.1.

4.1 Geometrical model description

The model created in ANSYS SpaceClaim is defined as a surface body with surface normal pointing outwards and with the mass of the model defined as a point mass located in the centre of gravity. The origin of the coordinate system is located at the geometric centre of the sphere, with the $z-axis$ positive upwards. The free water plane is defined at $z = 0$ and splits the sphere such that the model consists of two hemispheres of equal size, one above and one below the free surface. As linear potential theory solves the problem at the mean surface(i.e $z = 0$), only the lower half of the sphere is necessary to obtain a solution. The upper part was however added for visualization purposes, but could be suppressed during simulations. The physical properties of the sphere are described in table 3. The natural period of the heave motion of the sphere can be computed analytically as [23]

$$T_0 = \frac{2\pi}{1.025}\sqrt{\frac{R}{g}} \tag{4.1}$$

where R is the sphere radius and g is the gravitational acceleration. This yields a natural period of $T_0 = 4.4$s.

Parameters	**Values**
Radius of the sphere	5 m
Initial sphere location	0.0,0.0,0.0 m
Centre of gravity	0.0,0.0,-2.0 m
Mass of sphere	261800 kg
Natural period	4.4 s
Water depth	Infinite
Water density	1000 kg

Table 3: Physical properties

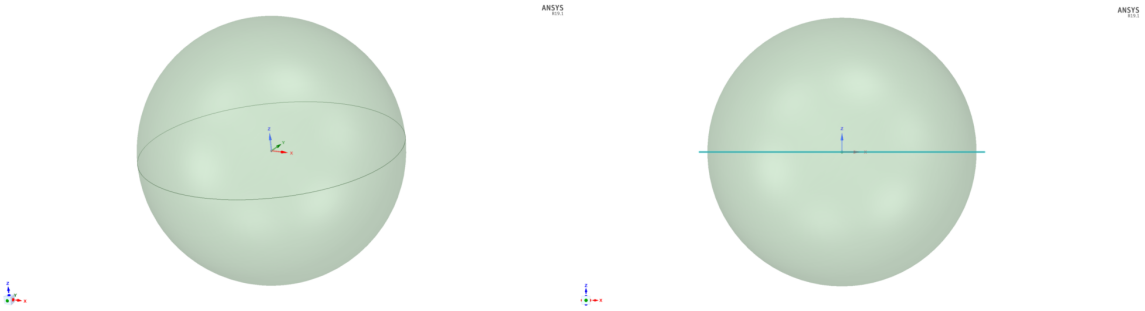

(a) Isometric view

(b) The blue line marks the water line

Figure 17: Display of the model in ANSYS SpaceClaim. Radius of 5m. The z-axis is positive upwards.

4.2 Mesh refinement by validation of hydrodynamic coefficients

The element size and it's impact on the solution is an important aspect of numerical solutions based on a finite number of elements. Analytic solutions of the added mass and damping associated with the periodic motions of a half-immersed sphere exists. An analytic solution was first given by Havelock[32] and later simplified and generalized by Hulme [35]. The numerical solutions of the added mass and damping should converge towards these analytic solutions, which therefore are suitable to use as reference in a mesh refinement study. Furthermore, the asymptotic value of the added mass when $\omega \to \infty$ can be estimated by studying the linear free surface condition(2.10). It is seen that $\phi \to 0$ on $z = 0$ as $\omega \to \infty$. This problem is equivalent to a sphere in infinite fluid and the analytic solution is (see Newman [45])

$$A_\infty = \frac{m}{2} \tag{4.2}$$

where m denotes the mass of the sphere. The asymptotic value of the analytical and numerical solution of the added mass should therefore converge towards a value equal to half of the mass. The asymptotic value of the heave damping is zero. Table 4 below contains the general properties of the investigated mesh refinements, which are the total number of elements on the model, N_{ele}, the number of diffracting elements, N_{dif}(see section 2.3.1 regarding diffracting and non-diffracting elements), the element size ΔS, and the corresponding maximum allowed wave frequency f_{max}. The element size is in Aqwa explicitly related to the maximum frequency which can be utilized in the diffraction analysis, where finer mesh allows for analysis of higher regular wave frequencies.

$\mathbf{N}_{ele}$	$\mathbf{N}_{dif}$	$\mathbf{\Delta S}$ $[m]$	$\mathbf{f}_{max}$ $[Hz]$
1064	532	1.00	0.574
5610	2805	0.40	0.884
14522	7261	0.25	1.122
39424	19712	0.15	1.444

Table 4: Properties of the mesh refinement. The 64-bit version of the Aqwa solver is limited to 40000 elements, of which 30000 may be diffracting.

The dimensionless added mass, $\mu_{33} = \frac{A_{33}}{m}$, is in figure 18 plotted for the different mesh refinements. The numerical solution coincides quite well with Hulme, and it is seen that the solution converges toward the asymptotic value of 0.5 for high frequencies. The 64-bit version of the Aqwa solver is limited to a maximum 40000 elements, of which 30000 may be diffracting. The finest mesh described in table 4 consists of 39424 elements, which is close to the maximum capacity of Aqwa. The corresponding added mass is described with a blue line in figure 18 and 19. It is observed that for values between 2 and 10 along the axis of abscissa, which is equivalent of a frequency between $0.32Hz$ and $0.71Hz$(or a period between $1.41s$ and $3.13s$), the numerical solution seem to diverge slightly from Hulme. Thus, the numerical solution converges towards a slightly erroneous value in this

frequency range. The reason for this deviation is not clear. A mesh refinement allowing a maximum element size of 0.25 was chosen(marked with * in figure 18 and 19), as the solution converges toward the same value as for finer mesh refinements. The dimensionless radiation damping for this mesh is plotted and compared to Hulme's solution in figure 20. It follows the analytic solution without any significant deviations.

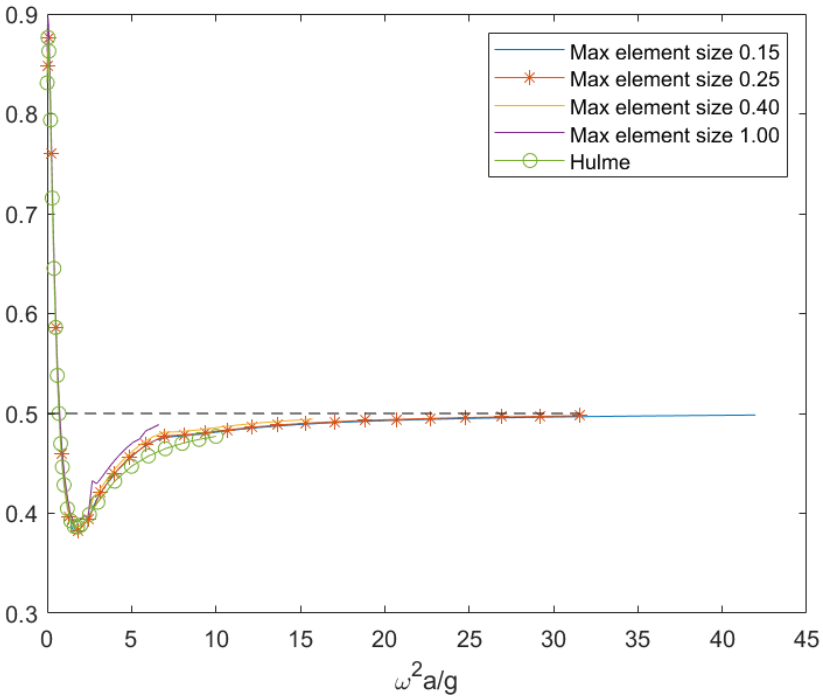

Figure 18: Non-dimensional added mass for different mesh refinements. Max element size refers to the maximum allowed element size generated by Aqwa. The dotted line represents the analytic value

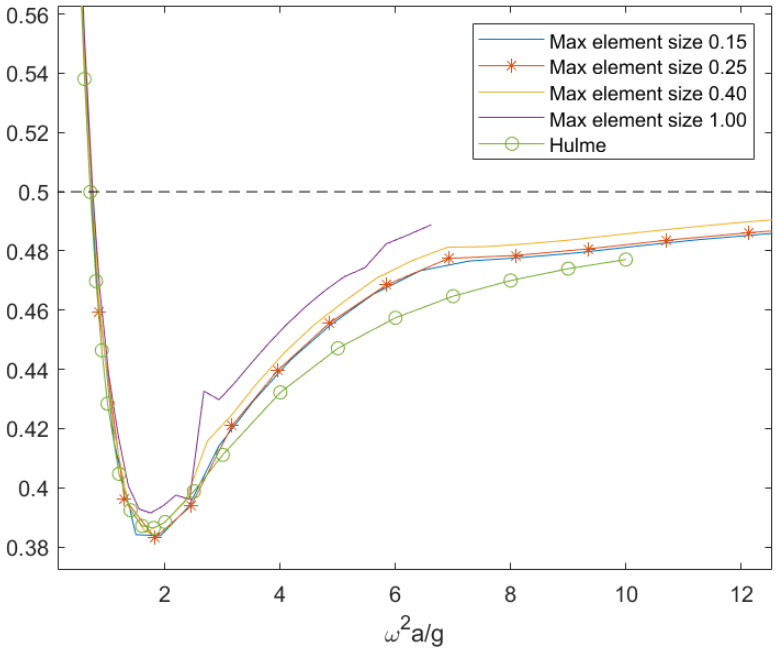

Figure 19: Non-dimensional added mass, μ_{33} for different mesh refinements. Close-up of the plot in figure 18, focused on the frequency range where Hulme's solution applies.

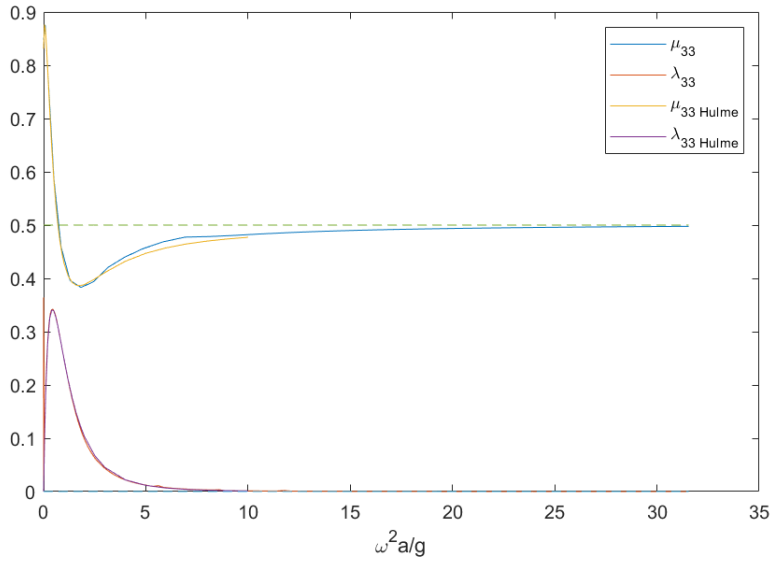

Figure 20: Non-dimensional added mass, μ_{33}, and damping, λ_{33}, compared to analytic results from Hulme [35]. The dotted lines represents the analytic value. $\Delta S = 0.25$

4.3 Observation of fundamental assumptions

The foundation of complex simulation tools such as Aqwa boils down to simple assumptions and phenomenons. From a learning perspective, it was interesting to investigate and observe some of the basic assumptions of potential theory.

Soluiton up to the mean free surface

Figure 21 shows the hydrodynamic pressure distribution over the sphere for an arbitrary incoming wave. The main purpose of this plot is to visualize that the potential is solved up to the mean free water level, a result of the linearization in (2.10). It is seen that the dynamic pressure is large under the wave crest, and low in a wave through. The green color along the upper half denotes zero, which can bee seen in the color scale.

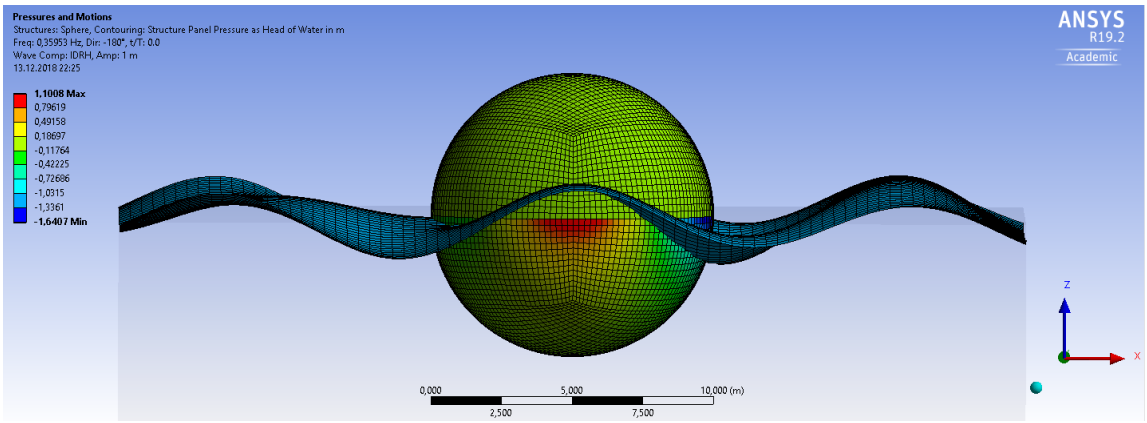

Figure 21: Dynamic pressure distribution for an arbitrary incident wave

Furthermore, the mean wetted body surface, which is the lower hemisphere, is constant and previously denoted S_0.

Particle behaviour at the free surface

When the sphere is exposed to waves with significantly long periods, the sphere would according to theory(see for example [27] or [47]) act as a particle at the surface, as described in figure 11. Hence, the occurrence of this motion was investigated. The position of the sphere during one wave period is illustrated with a series of pictures below, when exposed to a wave with unit amplitude and period of $200s$. The expected circular motion is observed.

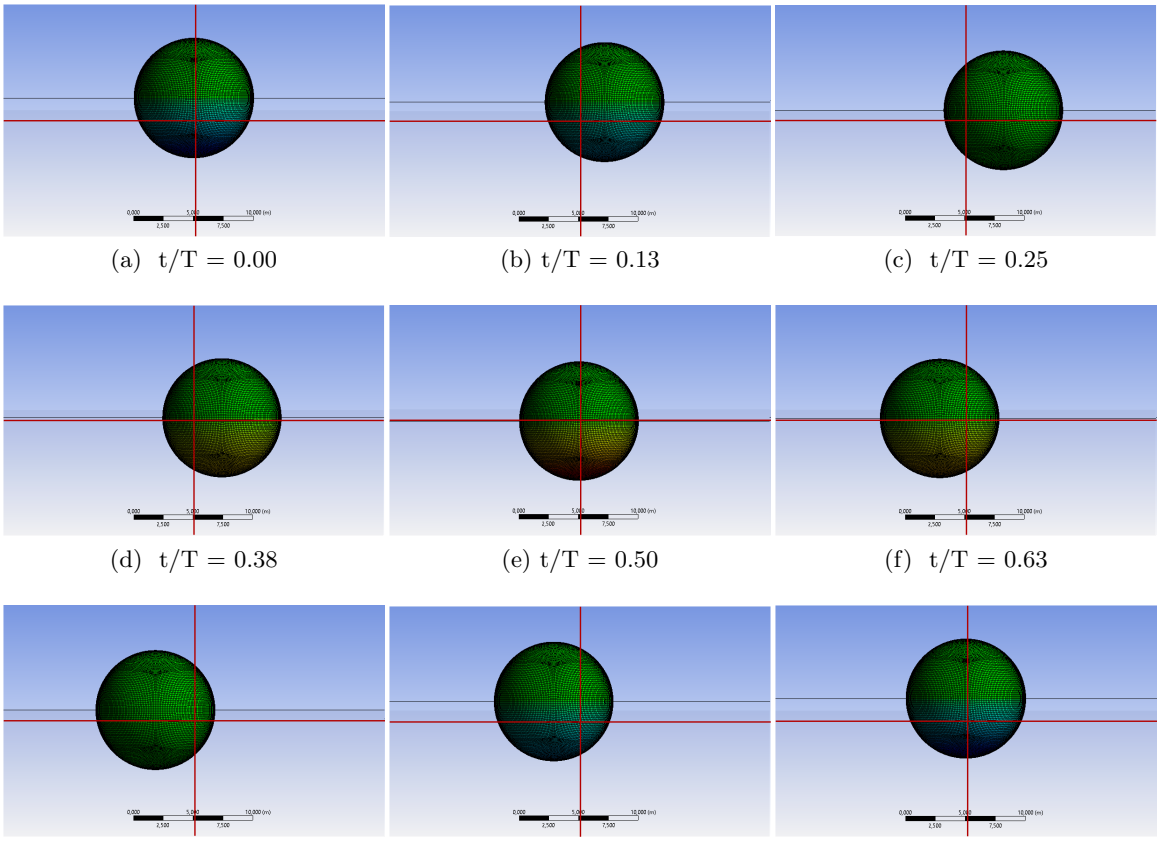

(a) t/T = 0.00 (b) t/T = 0.13 (c) t/T = 0.25

(d) t/T = 0.38 (e) t/T = 0.50 (f) t/T = 0.63

(g) t/T = 0.75 (h) t/T = 0.88 (i) t/T = 1.00

Figure 22: Illustration of the sphere motion at the surface for a wave with unit amplitude and period $T = 200s$. The illustrations from (a) to (i) shows that the sphere acts as a fluid particle with circular motion at the surface when exposed to a sufficiently large wave. The motion can be seen relative to the red, fixed coordinate system.

4.4 Free decay test

In a free-decay test the initial displacement of the body is ascended to desired heights above the mean water line. The test is initiated with the sphere falling back into the water. It is initially immersed below the equilibrium position before it floats back up again but with lower amplitude than the initial displacment. The result is a damped oscillation around the equilibrium position, which highlights geometric nonlinearities.

A decay test was performed for three different initial displacements; 1m, 3m and 5m above the mean waterline from the geometric centre of the sphere in the initial mean position(see figure 23). It is important to note that the validity of the results themselves for the largest

initial displacement, 5m, are highly questionable, as the premise for both linear and weak nonlinear solutions are small motion amplitudes. The initial drop height would give rise to slamming and other water entry effects which are outside of the area if evaluated effects in this thesis. Hence, one would expect deviations to solutions in which considers these effects such as heavy CFD simulations. Nevertheless, these tests were in the task 10 project part of a numerical code-to-code comparison with focus on detecting similarities and differences, and is why these extreme cases were included.

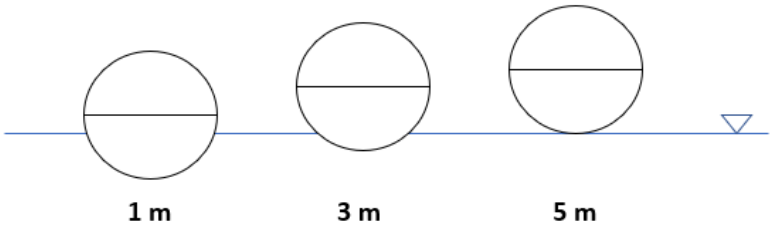

Figure 23: Illustration of the initial displacements of the free-decay test

In accordance with the task 10 project, 40 second long time-series of the free-decay tests in heave were performed. The linear and weak nonlinear time-series are illustrated figure 25 to 27 below. From the power spectral density(see figure 24) it is seen that the natural frequency obtained numerically in Aqwa is 0.225 Hz for all three initial displacements. It almost coincides up to three decimals with the analytic value of 0.227 Hz. For an arithmetic precision of one, that corresponds to a numerical natural period of 4.4 s, which is the same as the analytic value described in section 4.1.

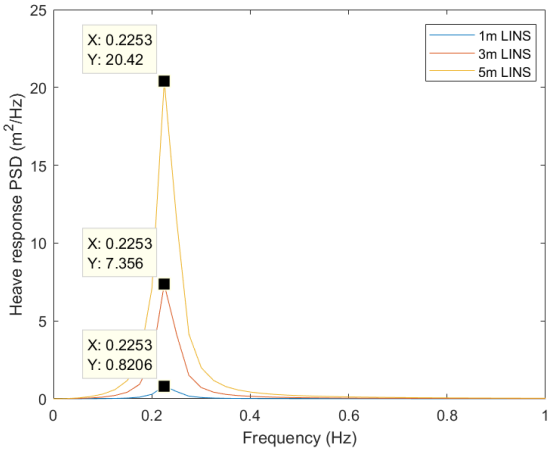

Figure 24: Power spectral density of the heave motion, for an initial displacement of 1 m, 3 m and 5 m. The marked points describes the frequency(X-value) at the first order peak in the heave response PSD(Y-value) for each initial displacement

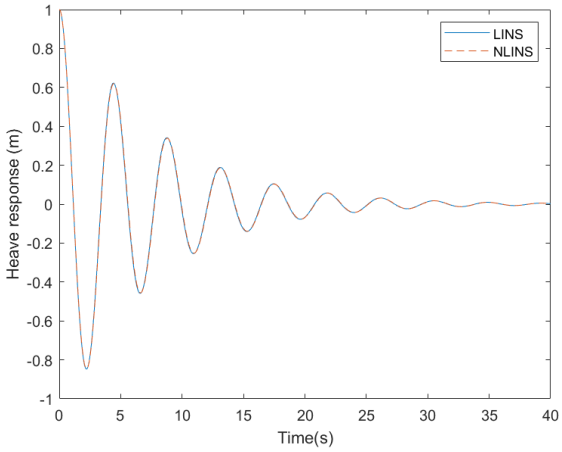

Figure 25: Initial displacement of 1 m

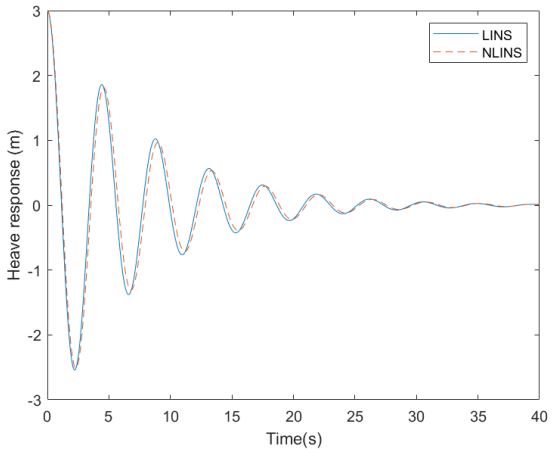

Figure 26: Time-series of the free decay test with initial displacement of 3 m

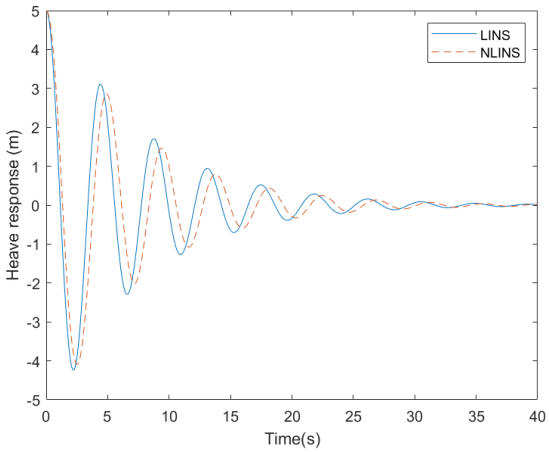

Figure 27: Time-series of the free decay test with initial displacement of 5 m

The linear model describes the motion well for the two lower initial displacements. For the highest displacement the nonlinear calculation of hydrostatics caused a phase shift in the motion response. Remember that the weak nonlinear model considers the instantaneous wetted surface when calculating the restoring force. For a sphere, which geometry is nonlin-

ear, the impact of these effects increase with larger oscillation amplitudes. For a geometry with constant CSA, such as a long vertical cylinder, these effects would not be prominent.

An important remark is that the linear solution coincides with the weak nonlinear solution for the low initial displacements. It illustrates that the linear assumption is reasonable for small motions, and simulation tools based on pure linear theory gives realistic solutions when used appropriately.

4.5 Regular waves

Several runs for a wide range of wave periods and heights were tested(table 5). Ten wave periods were tested for three different levels of wave steepness and two different model configurations; free to move in heave and free to move in heave with additional optimum PTO damping. That is a total of 60 regular wave simulations. The wave steepness S was computed for deep-water conditions as

$$S = \frac{H}{gT^2} \tag{4.3}$$

Note that the wave steepness formally is the relation between the wave height and wave length, which in deep water yields $\frac{H}{\lambda} = 2\pi\frac{H}{gT^2} = 2\pi S$. Hence, a factor of $\frac{1}{2\pi}$ is implemented in the expression of S. The different heights for each wave period described in table 5 are determined from (4.3) in order to maintain the desired wave steepness. Figure 28 illustrates the regular waves in a context with the wave breaking limit and the relative importance of mass and diffraction forces.

T[s]	f [Hz]	λ [m]	H1 [m] S = 0.0005	H2 [m] S = 0.002	H3 [m] S = 0.01
3.0	0.333	14.04	0.044	0.177	0.883
4.0	0.250	24.96	0.078	0.314	1.570
4.4	0.227	30.20	0.095	0.380	1.899
5.0	0.200	39.00	10.123	0.491	2.453
6.0	0.167	56.16	0.177	0.706	3.532
7.0	0.143	76.44	0.240	0.961	4.807
8.0	0.125	99.84	0.314	1.256	6.278
9.0	0.111	126.36	0.397	1.589	7.946
10.0	0.100	156.00	0.491	1.962	9.810
11.0	0.091	188.76	0.594	2.374	11.870

Table 5: Regular wave properties

Similarly to the diffraction test, the waves are propagated according to (equation)

Figure 29 illustrates the estimated validity limits of several theories for predicting ocean waves. The vertical axis expresses the steepness while the water depth is expressed along the horizontal axis. The red dots marks the validity area in which the waves tested in this report are located. Based on this model, Airy waves are only sufficient to accurately model the lowest steepness, $H1$. It is seen that Stokes 2nd and 3rd order wave theory is preferable to fully capture the waves of steepness $H2$ and $H3$ respectively. However, the primary goal is to study the effects of nonlinear device modeling and not those of nonlinear wave modelling. Thus, regular Airy waves are used to ensure that the background for the observed nonlinear effects are well understood. This do however highlight that the representation of the steep waves with Airy's theory does not necessarily describe a realistic wave shape, and that associated nonlinear wave modelling effects will not be captured in this study.

Lastly, it is common practice to calculate the response amplitude operator(RAO) when evaluating the motion of a body oscillating in a certain sea state and direction. The heave-motion response amplitude operator for each regular wave was calculated as

$$RAO = \sqrt{m_{peak}/\eta_{peak}} \tag{4.4}$$

where m_{peak} is the first order peak in the power spectral density(PSD) of the heave motion, and η_{peak} is the first order peak in the wave elevation PSD. This equation arises from the connection between the spectrum of a single input, $S_x(\omega)$ and the spectrum of the corresponding single output $S_y(\omega)$

$$S_y(\omega) = |H(\omega)|^2 S_x(\omega) \tag{4.5}$$

where it is seen that the RAO is a transfer function, commonly denoted $H(\omega)$. A thorough description is found in Newland[44]. The RAO described in (4.4) was computed likewise by the participants in the IEA OES Task 10.1. Note that this RAO only contains information of the first order response of a system. To evaluate eventual response of higher order it is necessary to investigate the PSD over a broader frequency range.

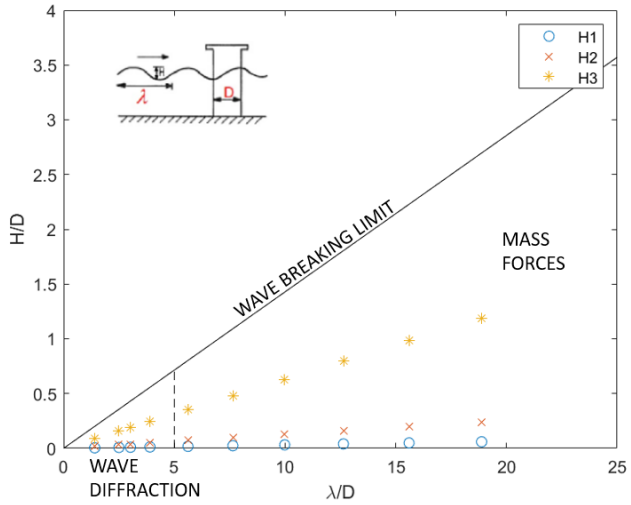

Figure 28: Relative importance of mass and diffraction forces for the regular waves. The figure shows the importance of mass, viscous drag and diffraction forces on marine structures. Viscous drag forces are not dominant until λ/D is approximately 90, and for that reason is not visible in this plot. The figure is adopted from Faltinsen[27] and Pettersen[47]

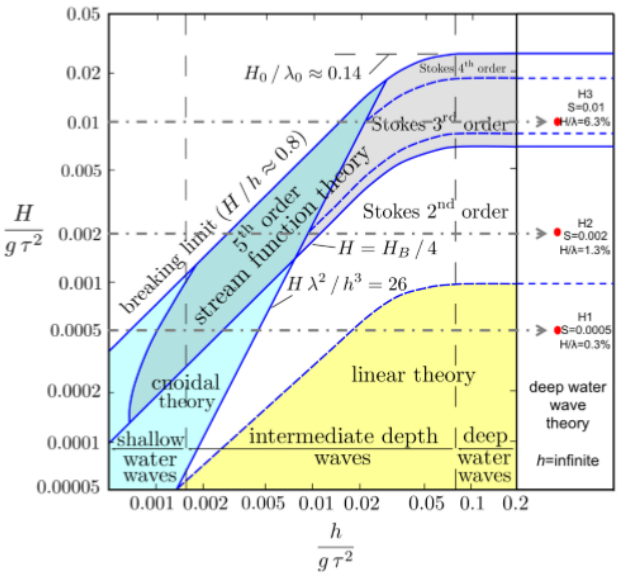

Figure 29: The steepness of the analyzed waves and validity limits. H is the wave height, g is the gravitational acceleration, τ is the wave period and h is the water depth. Retrieved from IEA OES Task10[56], who adopted it from Le Méhauté[40]

4.5.1 Freely floating in heave

Linear solution

The behaviour of the sphere in regular waves was first investigated with the linear model. The RAO of the heave motion, retrieved directly from Aqwa, is illustrated in figure 30. A peak occurs at a frequency that coincides with the natural frequency of the heave motion, which implies resonance. The RAO has a value of one in the stiffness dominated area(i.e when the load frequency is lower than the eigen frequency of the structure) and goes towards zero in the inertia dominated area(i.e when the load frequency is higher than the eigen frequency). The behaviour of the heave motion is in accordance with theoretical expectations(see for example[39]).

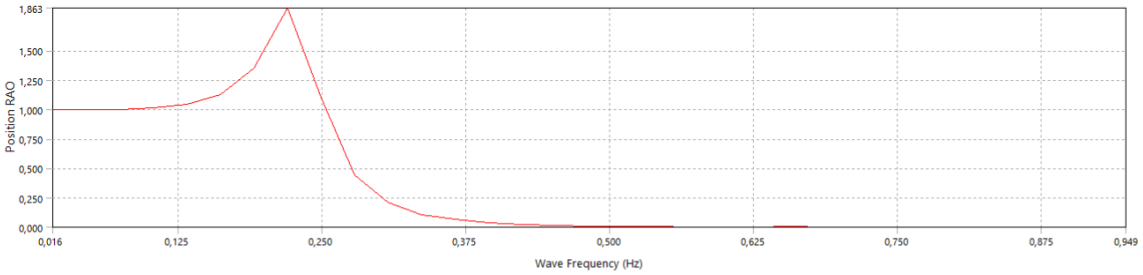

Figure 30: Response Amlitude Operator of the heave motion

The time-series of the heave motion of the sphere when exposed to incoming waves with periods of 3s, 4.4s, 11s and steepness $S = 0.0005$, are illustrated in figure 31 to 33, and illustrates the foregoing. These wave periods are highlighted in specific, as they corresponds to the cases where the system is strongly inertia dominated, in the resonant area and stiffness dominated. As expected, and in accordance with the RAO, the motion of the sphere is clearly larger than the wave elevation when $T = 4.4s$. The sphere is barely moving for high frequencies, and follows the wave elevation one to one when the frequency is low.

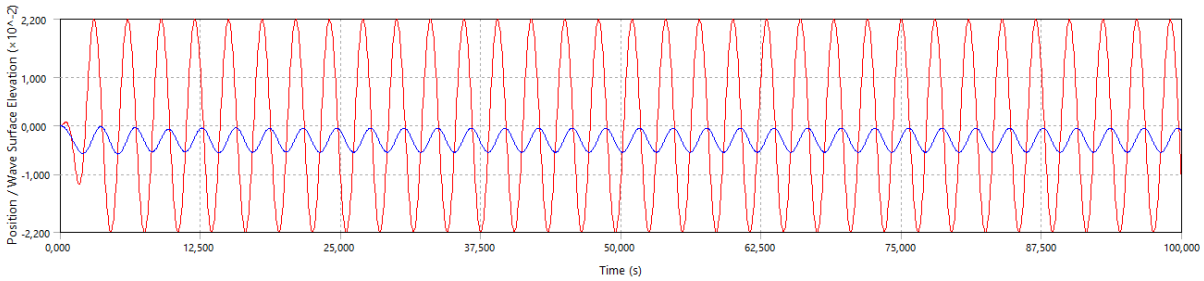

Figure 31: Response in heave for an incoming regular wave with period $T = 3.0s$. The blue line represents the heave motion and the red line is the wave elevation

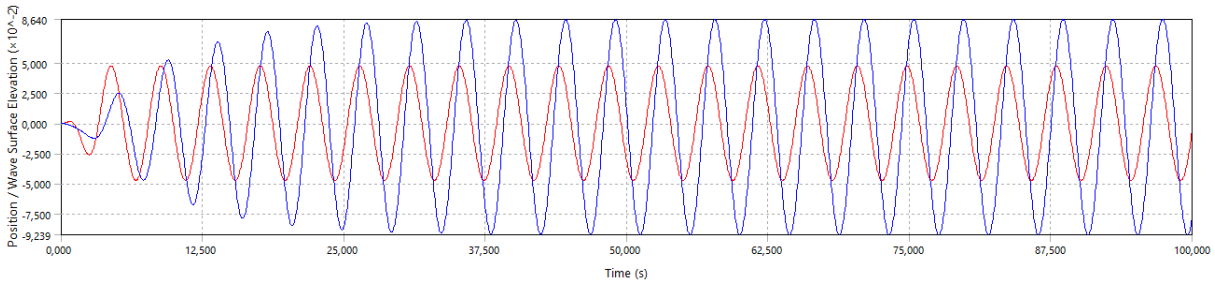

Figure 32: Response in heave for an incoming regular wave with period $T = 4.4s$. The blue line represents the heave motion and the red line is the wave elevation

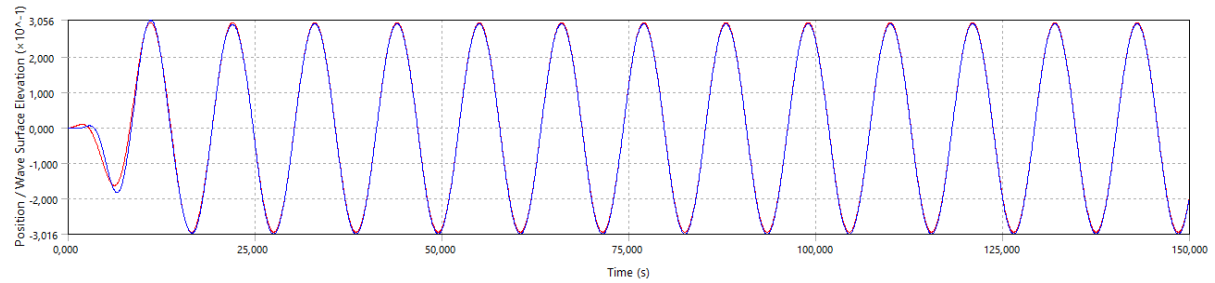

Figure 33: Response in heave for an incoming regular wave with period $T = 11.0s$. The blue line represents the heave motion and the red line is the wave elevation

The oscillating behaviour observed above gives rise to variation in the impact from different force components. Figure 34 to 36 shows the heave force contributions from the radiation force, diffraction force, Froude-Krylov force and the hydrostatic restoring force. For $T = 3s$, in the inertia dominated area, the diffraction force amplitude is of highest magnitude. The diffracted wave field is a result of the interaction between the incident wave and a fixed body. As a result, the diffraction force is large compared to the other force terms as the body motion is small(see figure 31).

For $T = 4.4s$(resonance) the hydrostatic restoring term is dominant. It is directly related to the displacement of the body from the equilibrium position (see equation (2.20)). Due to the resonant motions which are large relative to the wave amplitude (see figure 32), this term increases. Analogously, the radiation force is of greater impact due to large motions. The radiation force is caused by the displacement of water in the vicinity of the body when the body moves. Therefore, when the body oscillation is large compared to the surface elevation, this term increases.

Figure 36 illustrates the force components for the longest wave, $T = 11s$. In that case the Froude-Krylov and hydrostatic restoring forces are dominant. The radiated wave field as well as the disturbance from the incident waves are small as the sphere acts as a wave

follower(see figure 33). This a typical load condition for point-absorbers since they are small compared to the wave length. For this reason, as previously mentioned in section 2.1.1, the diffraction force is often neglected in practical applications and early design stages as the Froude-Krylov force is a good representation of the wave excitation force[4]. By avoiding to solve the body boundary condition for the diffraction potential one can reduce computational costs.

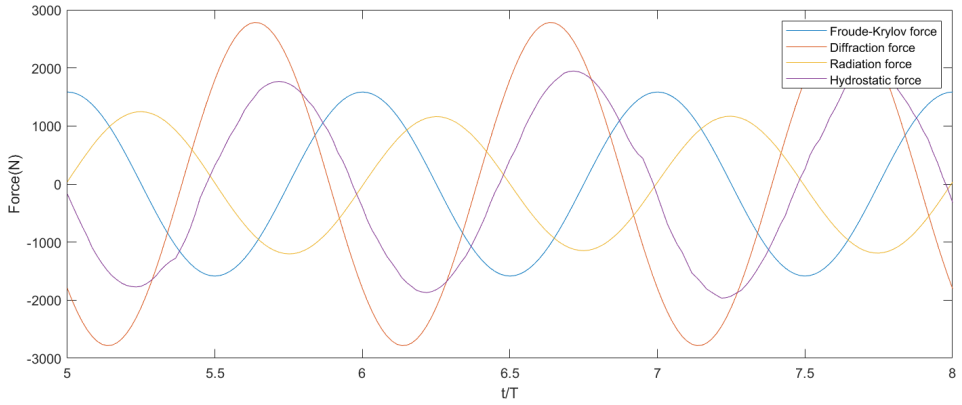

Figure 34: Froude-Krylov, diffraction and radiation force in heave for $T = 3s$ and $S = 0.0005$. The diffraction force is largest

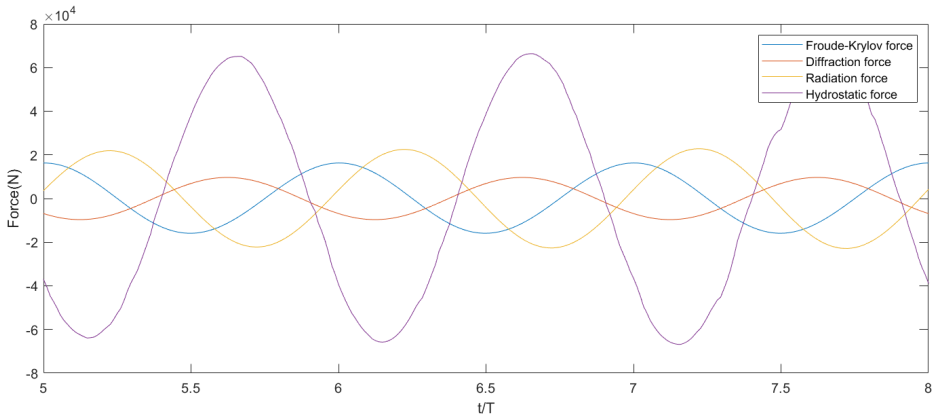

Figure 35: Froude-Krylov, diffraction and radiation force in heave for $T = 4.4s$(resonance) and $S = 0.0005$. The hydrostatic force is largest. The radiation force amplitude is higher than the diffraction and Froude-Krylov force amplitudes.

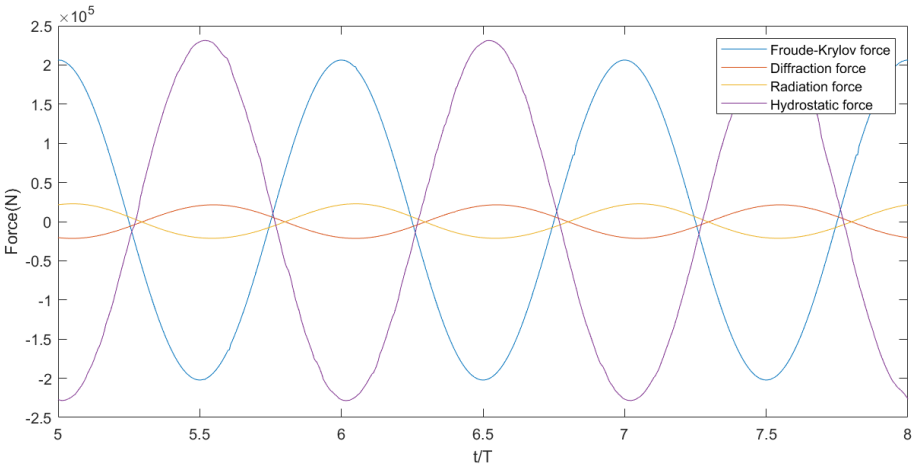

Figure 36: Froude-Krylov, diffraction and radiation force in heave for $T = 11s$ and $S = 0.0005$. The Froude-Krylov and hydrostatic forces are dominant.

Weak nonlinear solution

The effect of including weak nonlinearities was further investigated. Figure 37 to 39 below shows the amplitude of the Froude-Krylov(F_I), diffraction(F_d), radiation(F_r) and hydrostatic restoring(F_S) forces for the linear(LINS) and weak nonlinear(NLINS) solution for the floating sphere. Due to nonlinearities, forces may in general be asymmetric[29]. The force amplitude is therefore calculated as half of the variation between the crest and through. The force amplitudes in the transient part of the time series are excluded.

Firstly, it is clearly visible how the hydrostatic restoring and Froude-Krylov term dominates for long wave periods. It highlights the importance of properly estimating these forces when point-absorbers operates in such conditions. In figure 39 it is also observed that the Froude-Krylov force is increasingly dominating compared to the restoring term for steeper waves. That is reasonable as the steep waves are substantially larger than the small waves, and the corresponding force is therefore greater. For evaluation of heaving point-absorbers in survival mode, this term will most likely dominate.

Secondly, it is seen that the linear and weak nonlinear solution coincide quite well in small waves and shows decent agreement in steep waves. For the small waves($S = 0.0005$), the difference is neglectable. The wave heights are in that case too small compared to the dimensions of the device to induce motion amplitudes large enough to see any significant nonlinear effects. For the steep waves($S = 0.01$), noticeable deviations are observed in the case of resonance and in long waves. That follows the expectations as the nature of the problem is increasingly nonlinear with increased steepness, and especially in resonance where the relative motions between the surface and buoy are large. In the resonant case,

the linear solution predicts a somewhat smaller Froude-Krylov force and overpredicts the hydrostatic restoring force relative to the weak nonlinear solution. For the longest and steep wave(figure 39(b)) on the other hand, the linear solution underpredicts the restoring force. These differences are a result of the geometric nonlinearities related to the spherical shape, which most likely are better captured when the instantaneous wetted surface is considered. This should preferably be validated with a strong nonlinear simulation or experimental results before one concludes that the weak nonlinear solution is a better approximation.

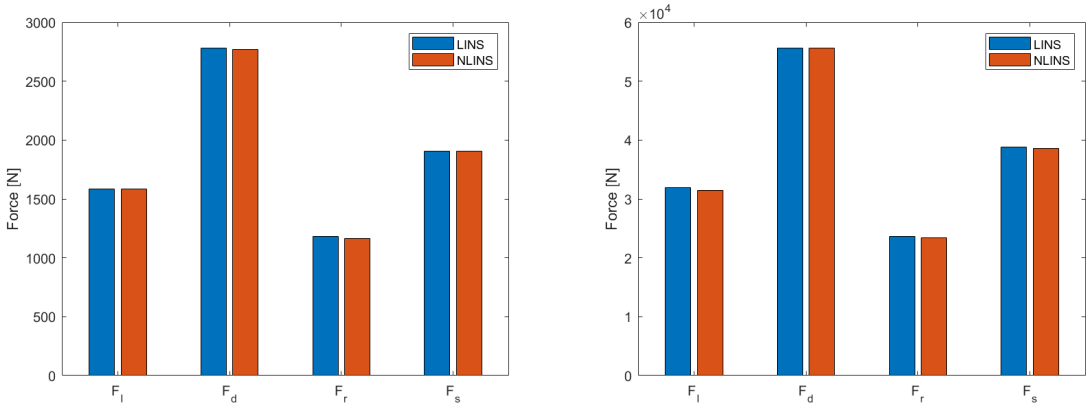

(a) S = 0.0005 (b) S = 0.01

Figure 37: T = 3s. Amplitude of the Froude-Krylov(F_I), diffraction(F_d), radiation(F_r) and hydrostatic restoring(F_S) force

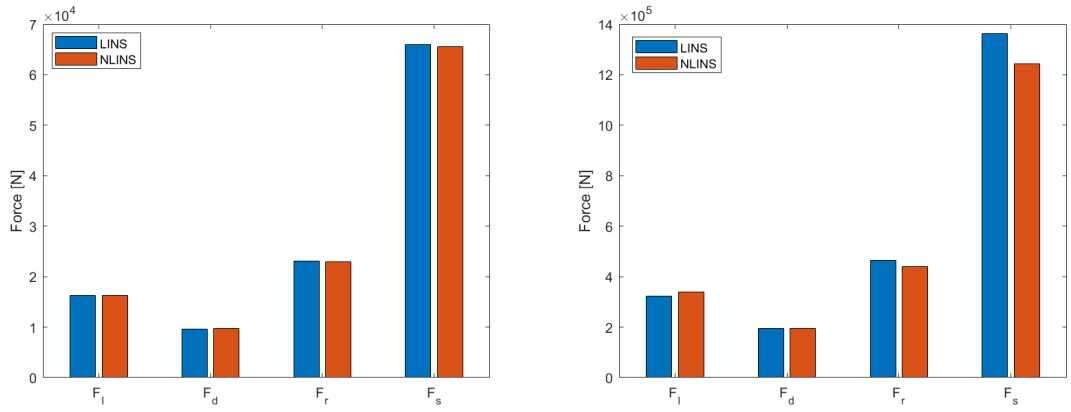

(a) S = 0.0005 (b) S = 0.01

Figure 38: T = 4.4s. Amplitude of the Froude-Krylov(F_I), diffraction(F_d), radiation(F_r) and hydrostatic restoring(F_S) force

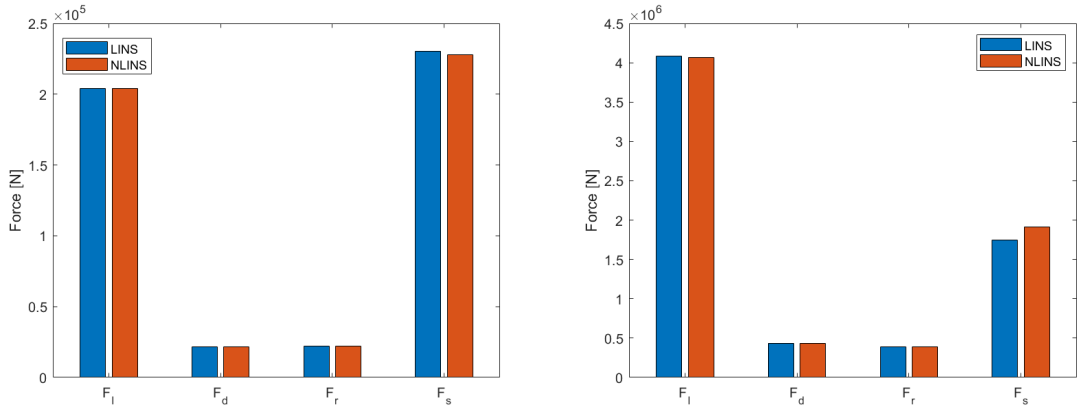

(a) S = 0.0005 (b) S = 0.01

Figure 39: T = 11s. Amplitude of the Froude-Krylov(F_I), diffraction(F_d), radiation(F_r) and hydrostatic restoring(F_S) force

Figure 40 shows the RAO's for the linear and weak nonlinear solution for the lowest and highest steepness respectively. As can be seen, there are some slight deviations in the first order motion response when the waves are steep. Although the deviations are small, it's arguably largest in the resonant area, where the linear solution is slightly over predicting the heave response compared to the weak nonlinear solution. That is reflected through figure 38, where the linear solution predicts a higher restoring force. Other than that, the

differences observed in the force components between the linear and weak nonlinear solution for the steep waves does not greatly affect the first order motion response.

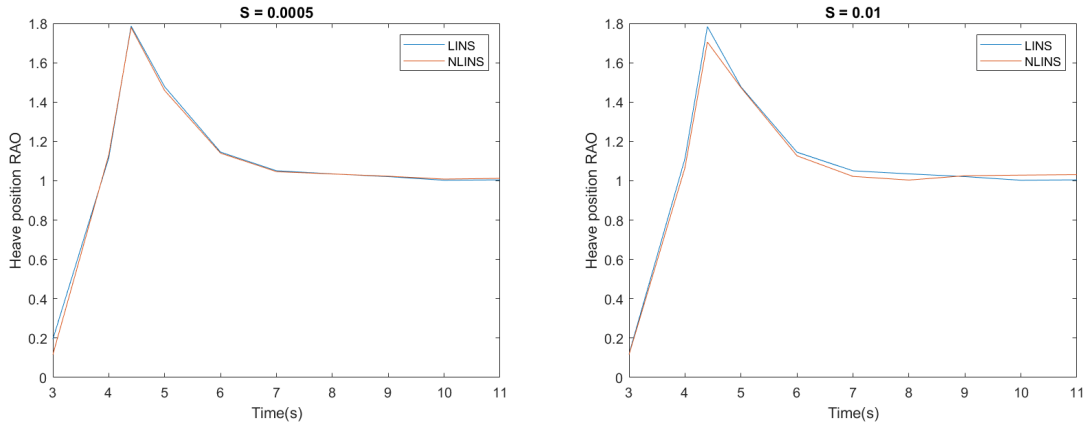

(a) S = 0.0005 (b) S = 0.01

Figure 40: First order heave response RAO, no PTO damping

The RAO's above only contain information about the first order motion of a system, as described in(4.4). By taking a look at the force power spectral densities, one can evaluate higher order motion and force responses. The PSD is generated through a Fast-Fourier transform(FFT) of the respective time-series. In general, the force and heave motion PSD's of the linear and weak nonlinear solution coincide in relatively linear load cases. In increasingly nonlinear cases, such as when resonance is induced in steep waves, higher order effects in the form of energy peaks at sub-harmonics are observed when the instantaneous wetted surface is considered. Figure 41 illustrates the foregoing for the Froude-Krylov and restoring force. The first order peak at the wave frequency is well captured for both codes. In the PSD of the weak nonlinear Froude-Krylov force, peaks occur at frequencies equal to higher multiples of the wave frequency($2f_w$, $3f_w$), which are not captured by the linear solution. Although not so apparent, two higher order peaks are also present at $2f_w$ and $3f_w$ for the restoring force. The second peak is seemingly captured by the linear solution, while the third order peak is only captured by the weak nonlinear solution. This illustrates that some higher order force effects are mitigated when only accounting for linear effects in rather nonlinear conditions. That might sound self explanatory, but it is important to note as point-absorbers designed for optimum energy capture most often are under the effect of a control system(i.e latching) and consequently operates in relatively nonlinear conditions. Similar observations were recently found by Giorgi and Ringwood[30] who investigated the possibility of analytical representation of nonlinear Froude-Krylov forces. They stated that in terms of energy absorption, this may transfer some energy from the exciting frequency to its multiples.

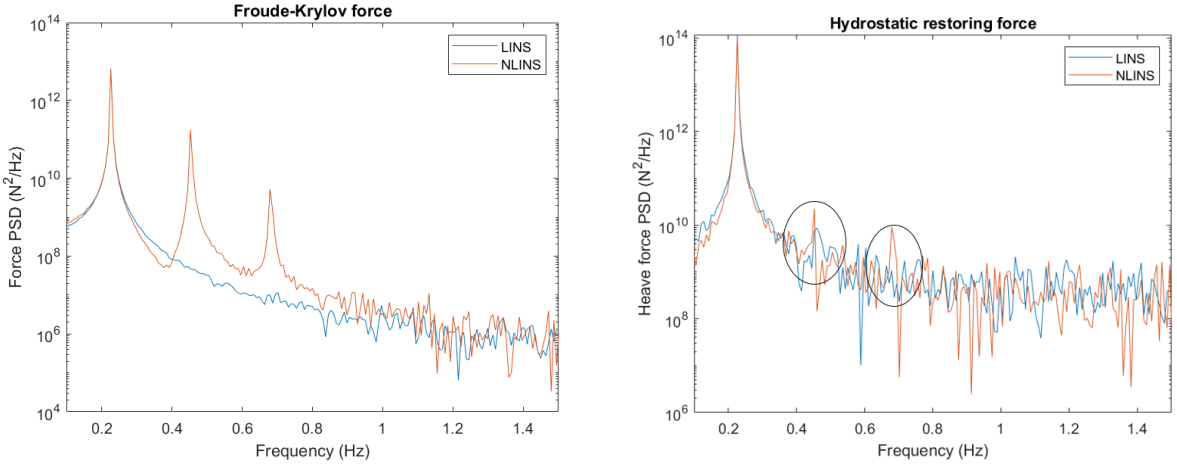

(a) PSD Froude-Krylov force

(b) PSD restoring force

Figure 41: PSD of the Froude-Krylov and restoring force. T=4.4s, S=0.01

Lastly, the impact of including the instantaneous wetted surface also affect the phase. Similarly to what one observed in the free decay test for a high initial displacement, a difference in the phasing between the two solutions occur when the waves are steep. For small waves, the phase is not affected by excluding weak nonlinearities. As an example, figure 42 illustrates phase difference for the heave force when the sphere is exposed to a wave with $T = 3s$ and $S = 0.01$. The heave force is the sum of the foregoing force terms; F_I, F_d, F_r, F_S.

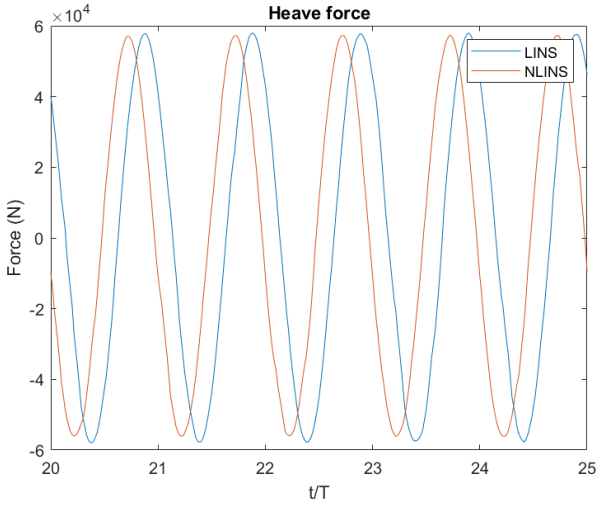

Figure 42: Heave force for a wave with T=3s and S=0.01. Phase difference between LINS and NLINS for steep waves

4.5.2 Oscillating in heave with optimum PTO damping

An additional linear damping force in heave was applied to simulate the optimum PTO damping. The damping is for simplicity linear, and calculated as described in section 3.3.3. In this study the hydrodynamic coefficients estimated in section This method of estimating optimum PTO damping is also used by the participants in IEA OES Task 10 [56]. The resulting damping coefficients for each wave are described in table 6. b

T[s]	Optimum Damping [Ns/m]	T[s]	Optimum Damping [Ns/m]
3.0	398736.034	7.0	479668.979
4.0	118149.758	8.0	633979.761
4.4	90080.857	9.0	784083.286
5.0	161048.558	10.0	932117.647
6.0	322292.419	11.0	1077123.445

Table 6: Optimum PTO damping properties. Retrieved from IEA OES Task 10[56]

Freely floating vs external PTO damping

The heave response RAO for each regular wave was calculated as for the case with zero additional damping(4.4). The effect of the PTO system can be observed in the heave position RAO in figure 43. The heave response amplitude is drastically reduced, and the RAO is below one for all periods. It converges towards 0.7 for large wave periods, which illustrates that the body will to a larger extent meet the waves, compared to the freely oscillating case where the sphere acts as a wave follower for long waves. This gives reason to expect that nonlinear effects are more prominent. The reduction in relative motion between the structure and the surface elevation can in a sense be seen as the energy absorbed from the system through the power take-off system.

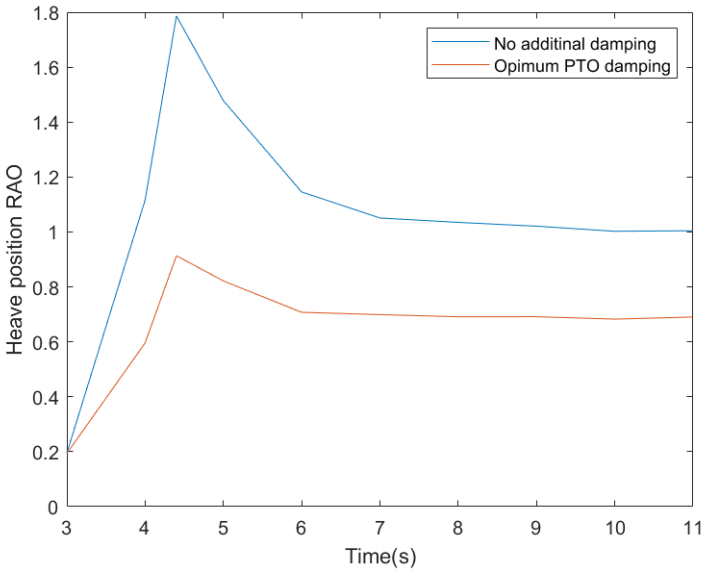

Figure 43: Linear solution. Heave position RAO

Figure 44 shows how the force amplitudes are affected by implementing the external damping. The force amplitudes for the case with and without PTO damping for the weak nonlinear solution are plotted. It is seen that the wave excitation forces(F_I, F_d) are equal in both cases. The incident wave potential is found by evaluating the wave without the body being present, which is corrected through the diffraction potential. Since the incident waves are the same in the two cases, and the diffraction potential is linearly calculated, they remain the same and independent of external damping. The radiation and restoring force on the other hand are both significantly reduced due to the reduction in heave response when PTO damping is applied.

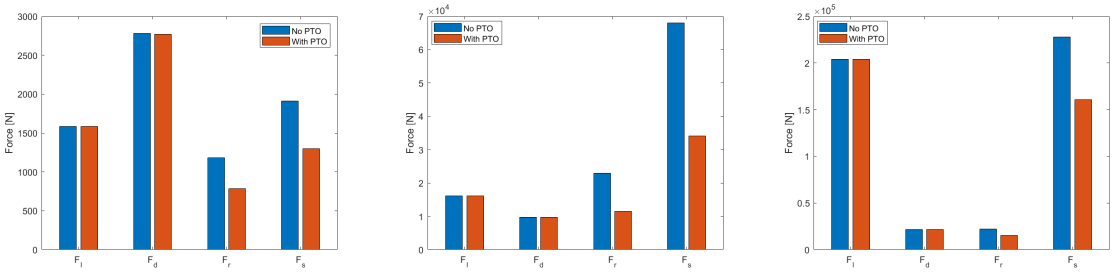

(a) T = 3s (b) T = 4.4s (c) T=11s

Figure 44: Force amplitudes with and without external damping for three different wave periods with $S = 0.0005$. The plots are from the weak nonlinear model

Linear model vs weak nonlinear model

The effect of accounting for the instantaneous wetted surface are initially studied by looking at the force amplitudes of the the Froude-Krylov, diffraction, radiation and hydrostatic restoring forces separately for the linear(LINS) and weak nonlinear(NLINS) solution. Similarly to the case with no external damping force. The force amplitudes are plotted in figure 45 to 47 below. As expected, the Froude-Krylov and restoring force are of most importance in long waves. The diffraction force is largest for small waves and the restoring force is dominates in resonance. The reason behind this observation is the same as for the sphere without external damping, which was discussed in section 4.5.1. It is seen that the two solutions(LINS, NLINS) coincide well for the lowest waves. For the steepest waves there are observed some differences. In the case of resonance, the linear solution overpredicts the radiation and restoring force and underpredicts the Froude-Krylov force. The same trend was observed for the sphere without external damping(figure 38). For the longest wave it is seen that the linear model substantially overpredicts both the Froude-Krylov and restoring force. As will be discussed later in this section, this greatly affects the heave response and energy output.

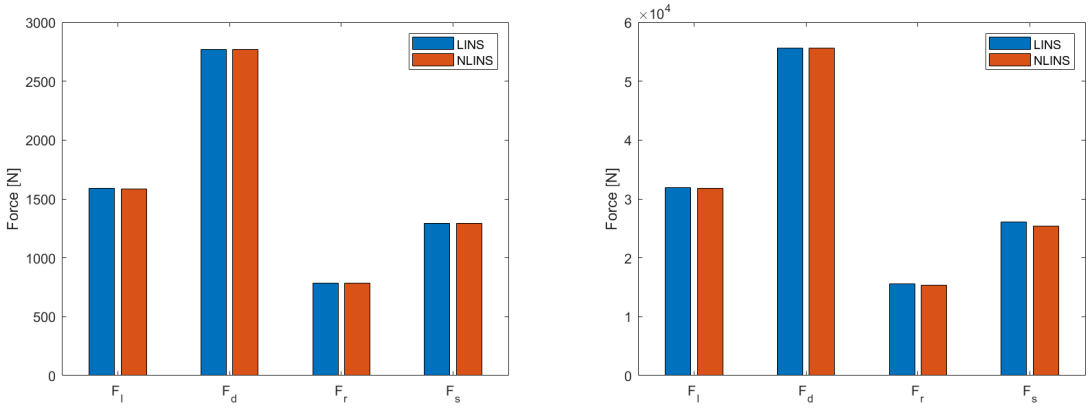

(a) S = 0.0005 (b) S = 0.01

Figure 45: T = 3s. Amplitude of the Froude-Krylov(F_I), diffraction(F_d), radiation(F_r) and hydrostatic restoring(F_S) force

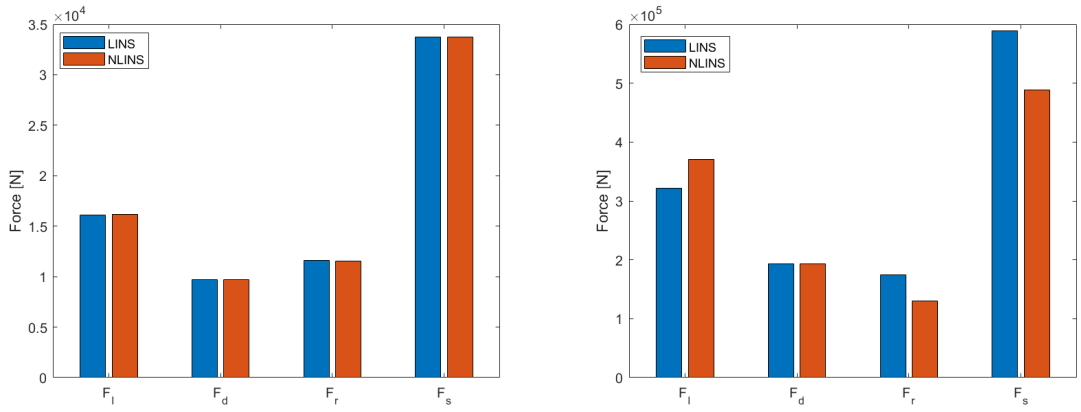

(a) S = 0.0005 (b) S = 0.01

Figure 46: T = 4.4s. Amplitude of the Froude-Krylov(F_I), diffraction(F_d), radiation(F_r) and hydrostatic restoring(F_S) force

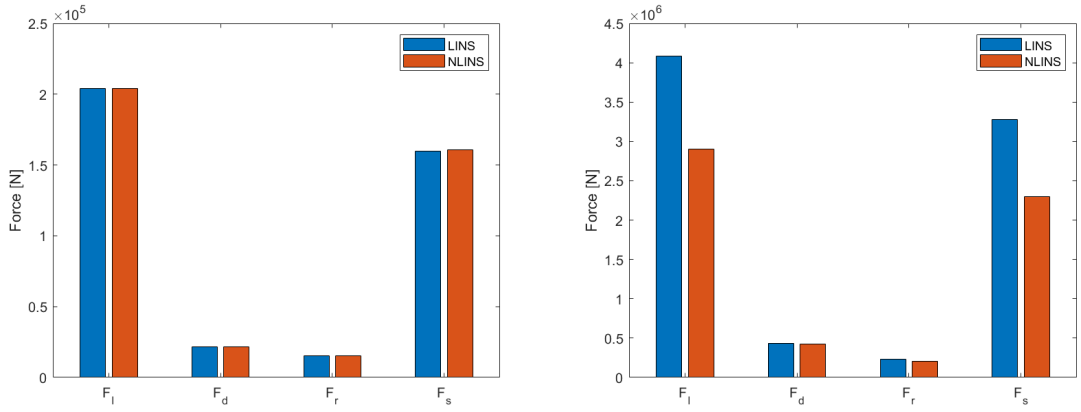

(a) S = 0.0005 (b) S = 0.01

Figure 47: T = 11s. Amplitude of the Froude-Krylov(F_I), diffraction(F_d), radiation(F_r) and hydrostatic restoring(F_S) force

The heave response RAO for the linear and weak nonlinear model are plotted for $S = 0.0005$ and $S = 0.01$ in figure 48. In small waves the motion is well described by the linear solution. The difference is however substantial for wave periods over 6s in steep waves. That is reflected in figure 47(b), where it is seen that the linear model predicts a significantly higher Froude-Krylov and restoring force. This overprediction results in a larger body motion which could give unreasonably optimistic predictions regarding energy harvesting. This

reduction in heave response was also observed between several linear and weak nonlinear codes in Task 10[56]. In the case of the free floating sphere, these effects were not observed. In that case the sphere acts as a wave follower, which implies that nonlinearities induced by changes in relative position between the instantaneous free-water surface and the heaving sphere are mitigated. That is however not the case when PTO damping is considered, which highlights that accounting for linear effects only is not necessarily sufficient to fully capture the behaviour when external damping is applied.

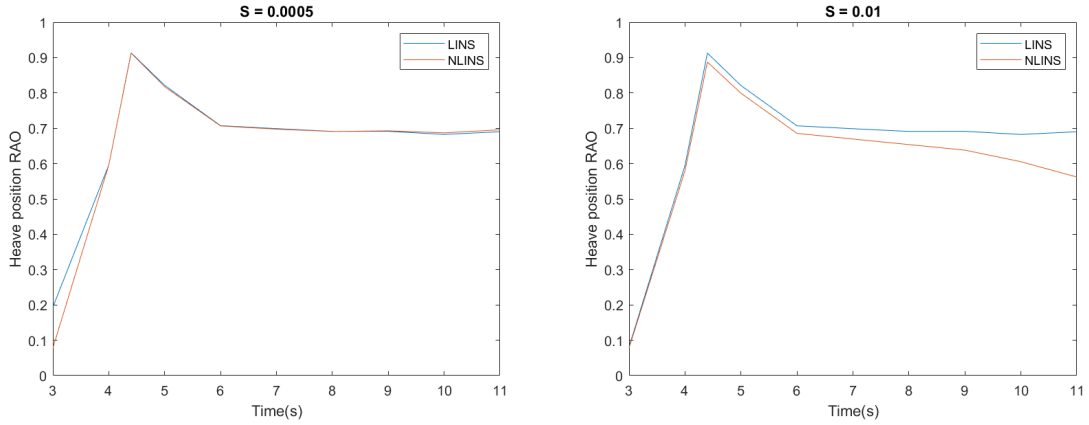

(a) S = 0.0005 (b) S = 0.01

Figure 48: Heave position RAO with optimum PTO damping. LINS denotes the results which only includes linear effects. NLINS includes weak nonlinearities.

Power absorption

The absorbed wave energy is expressed through the mean(time-averaged) useful power. A quick reminder; the mean or time-averaged useful power refers to the power consumed by the mechanical damper of the PTO system during one wave period. A brief derivation in optimal conditions is described in section 3.3.3, where it was seen that the the mean power can be estimated as

$$\overline{P_{u,opt}} = \frac{|F_{ext}|^2}{4(B_{33} + B_{g,opt})}$$

which is dependent on the excitation force, radiation and optimum PTO damping. The relation between the radiation damping and optimum PTO damping are illustrated in figure 49. B_{33} and $B_{g,opt}$ are equal in magnitude when the wave period coincides with the natural period of the body(resonance), which in this case is at $4.4s$. B_{TOT} has a local minimum at this wave period, which by looking at the expression above indicates that the maximum mean power should occur in the proximity of the natural frequency. In the frequency range

spanning from the resonant area and towards longer waves, $B_{g,opt}$ varies approximately linearly with the incoming wave period.

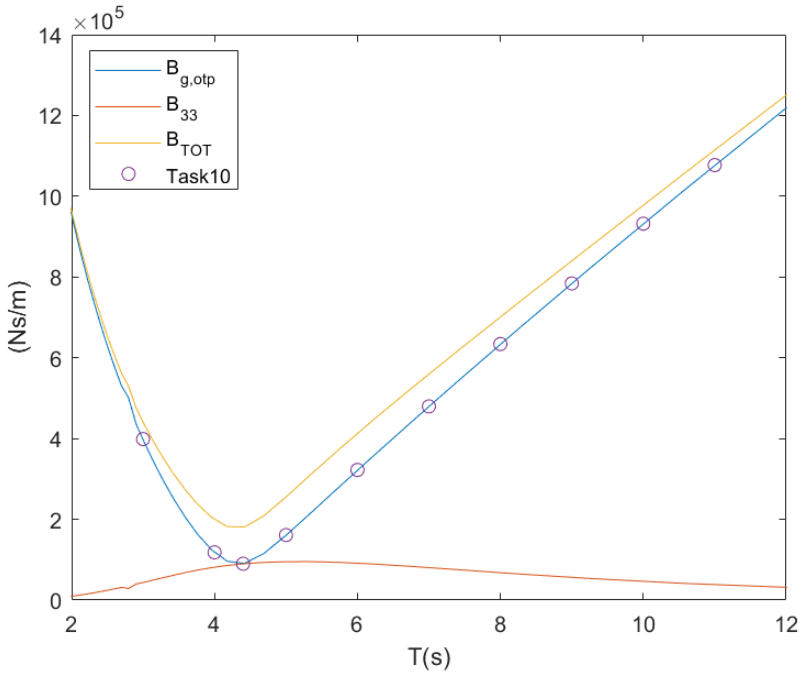

Figure 49: Radiation damping coefficient, B_{33}, and optimum PTO damping coefficient, $B_{g,opt}$ for the studied range of wave periods. B_{TOT} is the sum of B_{33} and $B_{g,opt}$. Task10 denotes the optimum damping coefficient values retrieved from the Task10 project described in table 6

The mean power, normalized by the square of the incident wave height, is plotted for regular waves with steepness $S = 0.0005$ and $S = 0.01$. For incident waves with low steepness, the two models show good agreement. For the steep waves, the models show decent agreement up to wave periods of 6s. For longer wave periods the two models start to diverge, and the effect of including the instantaneous wetted surface is clearly affecting the power estimation. That is directly connected to the reduced heave motion for wave periods over 6s seen in the heave response RAO for the weak nonlinear model in figure 48(b). Small motions generate less power. This divergence between the two models is caused by the geometric nonlinearities related to the spherical shape, which in large waves induces severe nonlinear hydrostatic and Froude-Krylov forces. The difference is seen in figure 47(b). The same trend between linear and weak nonlinear models was generally observed in IEA OES Task10.

In terms of energy production in steep conditions, the linear model suggests that the mean power level maintains a value slightly above 2 W/m^2 for wave periods longer than 6s. This could lead to an overoptimistic estimate of energy generation and related economic

predictions.

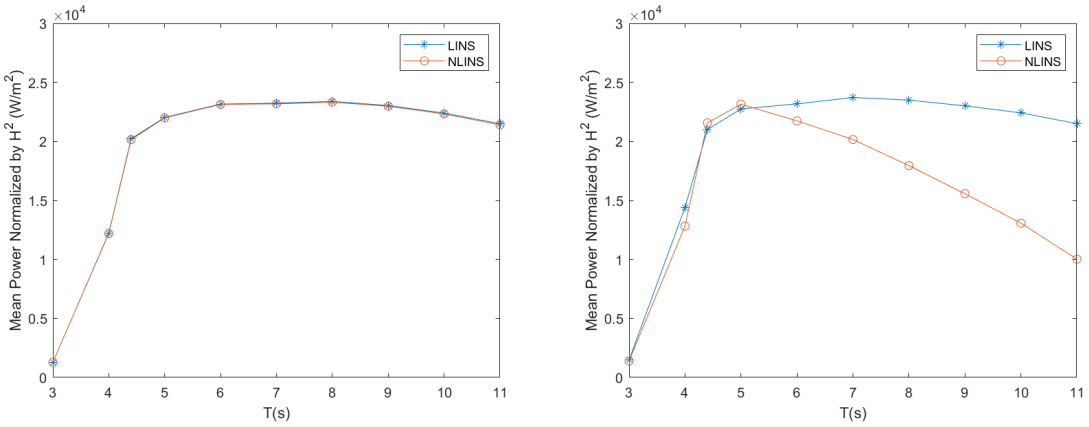

(a) S = 0.0005 (b) S = 0.01

Figure 50: Mean power normalized by the square of the wave height for the studied incident wave periods

4.6 Concluding remarks of the sphere assessment

- The free decay test for small initial displacements showed good agreement between the linear and weak nonlinear solution. For the large initial displacement($5m$), differences in terms of phasing and amplitude were observed, visualizing the effect of accounting for variations in the hydrostatic stiffness. The linear assumption is good for small motions.
- Evaluation of the dynamic behaviour of the freely floating sphere showed that diffraction forces dominates for high wave frequencies, the hydrostatic restoring and the radiation force are largest in resonance, and hydrostatic and incident wave (Froude-Krylov) forces dominates for frequencies lower than the natural frequency. It substantiates the commonly used approximation of the Froude-Krylov force often being a good representation of the excitation forces for point-absorbers operating in long waves(wave periods significantly larger than the natural period). For point-absorbers operating in resonance this approximation is not necessarily valid.
- For the free floating sphere the linear and weak nonlinear solutions showed in general good agreement. For the small waves ($S = 0.0005$) the wave height were too small compared to the dimensions of the device to induce motion amplitudes large enough to see any significant nonlinear Froude-Krylov or hydrostatic effects. Some deviations were observed in steep waves, arguably largest in resonance, where the linear solution seem to over-predict the restoring force. The PSD of the resonant Froude-Krylov

force in steep waves further showed that some higher order force peaks are mitigated in the linear solution. The effect of accounting for the instantaneous wetted surface did however not have a big impact on the resulting first order heave motion response in small or steep waves.

- The impact of including weak nonlinearities showed a greater impact when an external PTO damping was applied to the system. For low waves and wave periods in the diffraction dominated area(wave periods lower than the natural frequency), the two solutions showed good agreement. Deviations were however observed for steep incident waves oscillating with resonant frequency, and waves with higher period than the natural period. The impact of nonlinearities was most prominent for steep waves with period longer than 6 seconds. The weak nonlinear solution predicted a reduced heave response compared to the linear model, which resulted in a drastically reduced mean power estimation. This can be explained by the fact that the linear model significantly overpredicted the hydrostatic restoring and Froude-Krylov force. The reduced estimate from the weak nonlinear solution is caused by accounting for geometrical nonlinearities related to the sphere surface. This effect was not so prominent for the freely floating sphere without PTO damping, as it acts as a wave follower in long waves.
- To summarize; accounting for linear effects only is not necessarily sufficient to fully capture the behaviour when external damping is applied to the system. Based on this study the weak nonlinearities should be considered in steep waves or other nonlinear cases such as resonance where the body motions are large. The linear solution can give an unrealistic and overoptimistic estimate of energy generation and economic predictions in those cases compared to the results from the weak nonlinear model. The weak nonlinear model does only consider the effects of the nonlinear Froude-Krylov and hydrostatic restoring force. Nonlinear effects from higher order modelling of the waves, kinematics above the mean waterline such as Wheeler-stretching, effects related to viscosity or other effects are not considered. Implementation of such effects could affect the results and give rise to different conclusions.

5 Hydrodynamic assessment of the WEC float

The analysed WEC float is a real model stationed in Sandia National Laboratories(SNL). For that reason experimental data is available for validation of the simulations. The analysis will also be compared to results from other participants in IEA OES Task 10.2. The experimental data is available for public usage online at *https* : *//mhkdr.openei.org/submissions/*151.

The steepness of the incident are limited, as a point of the experiment was to avoid oscillations outside of the linear area of the WEC float to ensure comparable results to linear codes. For that reason it is not expected to see large variations between the linear and weak nonlinear model. This section will contain the following

- Description of the WEC float
- Validation of hydrodynamic coefficients. The added mass and radiation damping estimated in Aqwa will be validated against experimental results and a linear WAMIT simulation performed by NREL SNL
- A free-decay test to ensure that the model performs as expected and in accordance with other codes. Will be compared to a linear WAMIT simulation performed by NREL SNL and a strongly nonlinear CFD simulation in OpenFOAM conducted by RISE. No experimental data is available.
- A radiation test to evaluate the numerical radiation model.
- A diffraction test to evaluate the numerical diffraction model.

It was initially intended to perform a regular wave test as well, with the experimentally measured wave elevation and PTO force as input. However, some trouble with the implementation in Aqwa due to a minor bug in the lastest version(ANSYS v/2019 R2) at the time of writing made this difficult. This bug will according to ANSYS be fixed in the next version. The float is exposed to simulated regular waves with and without PTO force in section **??**.

5.1 WEC float model description

The WEC model geometry to be numerically assessed is made in Sandia National Laboratories. It is 1/17 of it's full-scale equivalent, which is not designed with intention of it to be a commercial WEC, but rather as a test reference for numerical WEC dynamics modelling and control. The geometric configuration and set-up is described in figure 51 below. The upper part of the float which pierces the mean water level is shaped as a cylinder, and the bottom half is shaped like a cone. The surface of the float therefore has a linear part(cylinder) and a nonlinear geometrical part(cone). It has the option of locking or unlocking multiple degrees of freedom, and thus able to consider a wide range of complexities. However, the model was in this test campaign restricted to heave motion only. The model was ballasted to obtain

the draft described in figure 51a. The test cases were further designed such that the model would oscillate with linear hydrostatics, i.e within $0.20m$ above and $0.16m$ below the mean water line. The model can be deballasted to provide a system in which the hydrostatics are strongly nonlinear. That is not the intention in this study, but provides possibilities for future research. The physical properties of the model are tabulated in table 7.

Parameters	Values
Rigid body mass(float only)	660 kg
Rigid body mass(float and slider)	858 kg
Displaced volume	0.858 m^3
Float radius	0.880 m
Float draft	0.530 m
Water density	1000 kg/m^3

Table 7: Physical properties

The model is equipped with linear translatory actuators in surge and heave, and a rotary actuator to simulate pitch/roll. Load cells are located at the surface of the model to measure forces experienced by the WEC device. These were used to measure the force output of the actuator and force input from the incident waves. With this set-up the float can be fixed, freely floating or forced to oscillate by the actuator. Further details regarding the experimental set-up and implementation can be found in the Sandia Report[10].

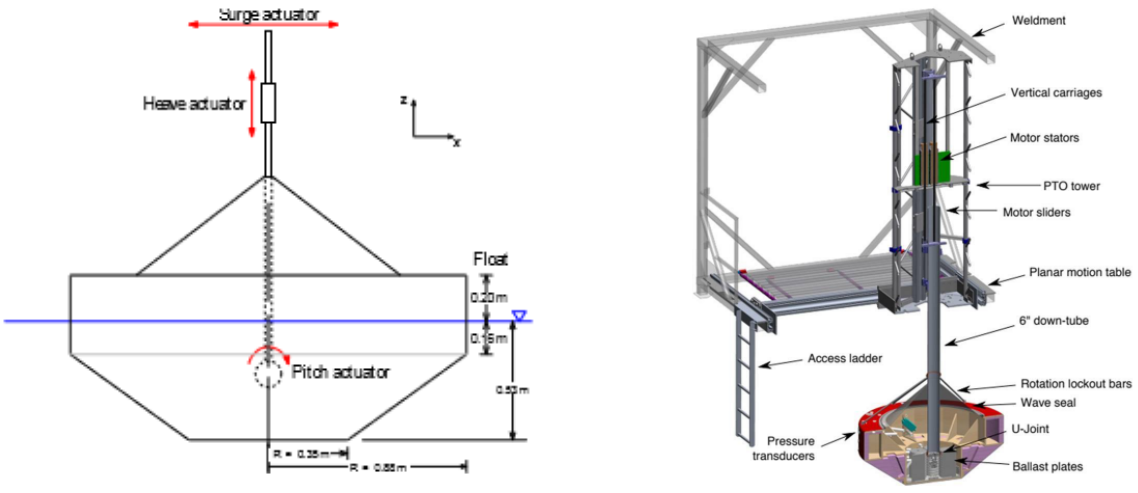

(a) Sketch of the float geometry

(b) Illustration of the set-up

Figure 51: IEA OES Task 10.2 WEC float geometry. The illustrations are retrieved from [10]

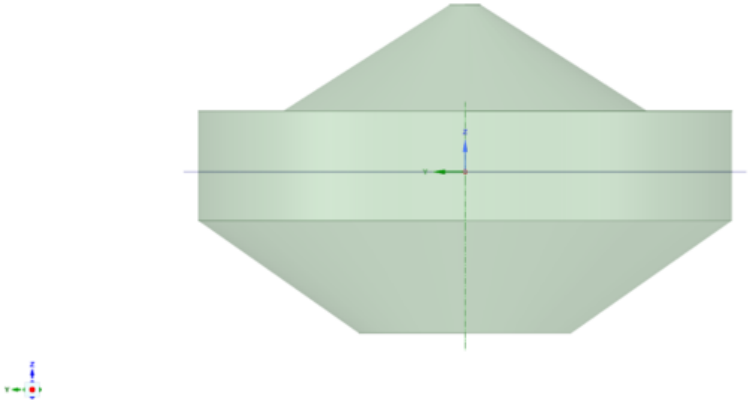

Figure 52: WEC model in ANSYS SpaceClaim

5.2 Validation of hydrodynamic coefficients

Unlike the well studied sphere geometry, there are no analytic solutions to hydrodynamic coefficients such as added mass and radiation damping for the WEC float. In order to validate the modeling in ANSYS, the added mass and radiation damping were compared to experimental and numerical data from Sandia National Laboratories[10]. There WAMIT was used as the tool to conduct the numerical assessment. Both ANSYS Aqwa and WAMIT are based on linear and second-order potential theory, and applies the panel method to solve for the velocity potential and fluid pressure on the submerged surfaces. Thus, similarity in the solutions is to be expected.

The mesh refinement found to be sufficient for the sphere was scaled down by using the ratio between the radius of the two geometries as a scaling parameter.

$$S_{WEC} = \frac{r_{WEC}}{r_{sphere}} \, S_{sphere} = 0.176 \, S_{sphere} \tag{5.1}$$

where S_{WEC} and S_{sphere} denotes the element size of the WEC and sphere respectively, r_{sphere} is the sphere raduis, while r_{WEC} is the radius of the circular water plane area of the WEC in the mean position(see table 7). This resulted in an initial element size of approximately 0.045. As can be seen in figure 53(a) and 53(b) below, the added mass and damping

$\mathbf{N}_{ele}$	$\mathbf{N}_{dif}$	$\mathbf{\Delta S}$ $[m]$	$\mathbf{f}_{max}$
16504	10207	0.045	2.889

Table 8: Properties of the mesh refinement

coincide with the simulations in WAMIT. Deviations here would indicate inaccurate modeling or coarse mesh. Figure 54 contains the plotted experimental and numerical results

from Sandia. It shows that the WAMIT simulation coincide with experimental data. This observation validates the WAMIT data, which also boosts the confidence in the data from the Aqwa simulations. Conclusively, the estimated added mass and damping from potential theory in general suits well with experimental results.

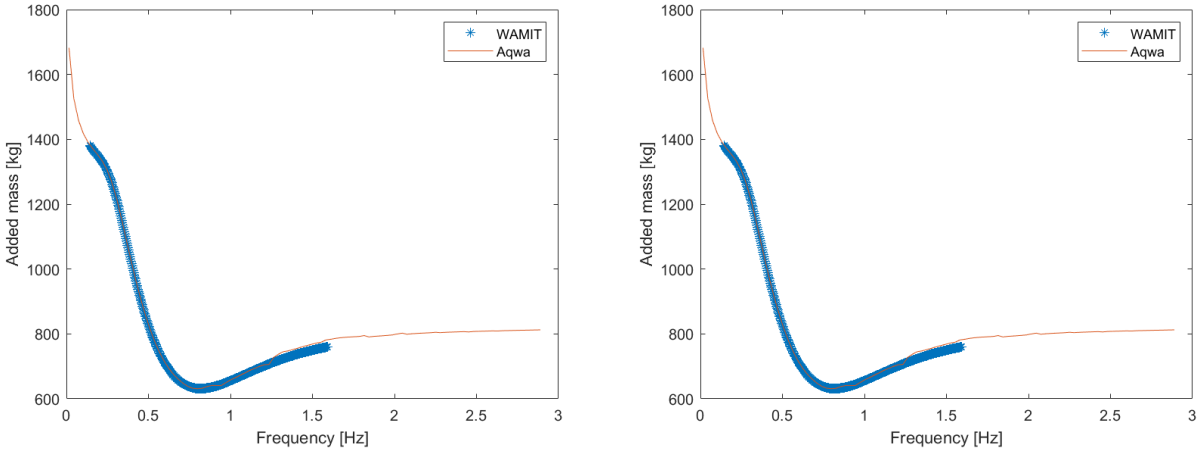

(a) Added mass

(b) Radiation damping

Figure 53: Added mass and damping for simulations in WAMIT(Sandia National Laboratories) and ANSYS Aqwa

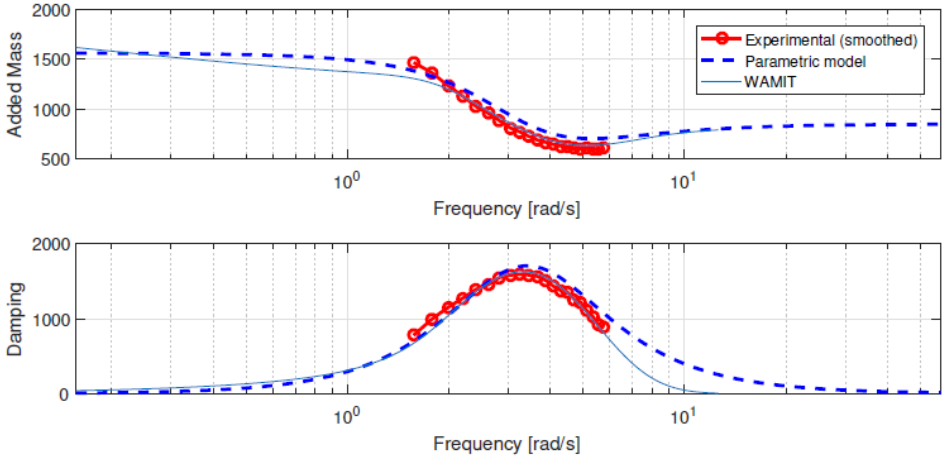

Figure 54: Data from Sandia National Laboratories. Added mass and damping. The plot shows smoothed experimental data and the data obtained in WAMIT. The figure also includes a parametric model, which is not further discussed. Note that the frequency is plotted logarithmic. Retrieved from [10]

5.3 Decay test

Introduction to the case:A free decay test of the WEC model was performed. No experimental data is available for the decay test, thus the results were compared to data from other participants in OES Task 10.2. It is a convenient way to further ensure that the model performs as expected and in accordance with other codes. Both linear and weak nonlinear analysis were conducted in Aqwa. Two decay test were performed with initial displacement of $0.1m$ and $0.2m$, referred to as DC1 and DC2 respectively. The first initial displacement is within the vertical surface piercing cylindrical shape of the WEC. Therefore one avoids geometrical nonlinearities. For the second case, the upper part of the coned surface exits the mean water level by a vertical distance of $0.04m$. That gives rise to occurrence of geometrical nonlinear effects due to a change in water plane area for the first oscillation(s). The water plane area will quickly become constant when the motion is damped.

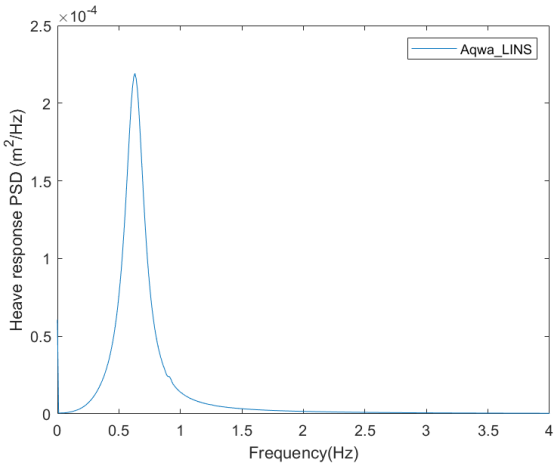

Figure 55: PSD of the heave response for an initial displacement of 0.1m. Peak at a frequency of 0.63 Hz

Results: The results from figure 56 shows that there are no significant deviation between the linear and weak-nonlinear solution. Compared to the free decay test of the sphere, the impact of evaluating geometric nonlinearities is small. A look at the PSD of the motion response in figure 55 shows that the WEC model has a natural frequency of $f_0 = 0.63Hz$, which corresponds to a natural period of $1.59s$.

The linear solution in Aqwa was further compared to a linear solution in WAMIT(conducted by SNL NREL) and a strong nonlinear solution from OpenFOAM(conducted by RISE). The results are described in figure 57. It is seen that the linear codes are good approximations, and are close to identical to the CFD simulation. It is however interesting to observe that in the first oscillation for the highest initial displacement, i.e when the CSA is not constant, the WAMIT code slightly over-predicts the motion amplitude compared to both OpenFOAM and Aqwa. Altough Aqwa and WAMIT are based on the same theory, different BEM softwares utilises different numerics to solve same equations. This might be visible here. Other than that the codes are in good agreement.

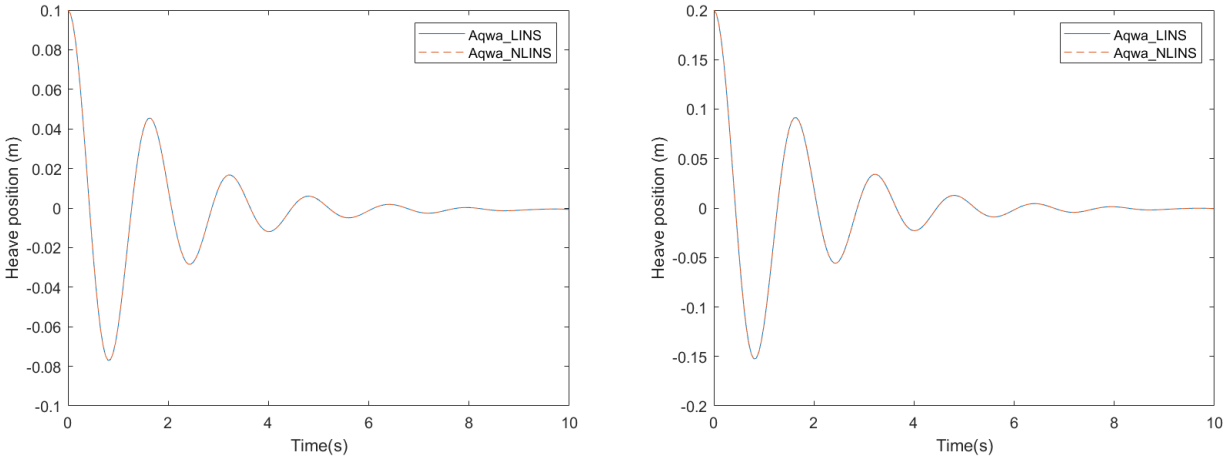

(a) DC1: Initial displacement 0.1m (b) DC2: Initial displacement 0.2m

Figure 56: Linear and weak nonlinear solution of the heave response for DC1 and DC2 in ANSYS Aqwa

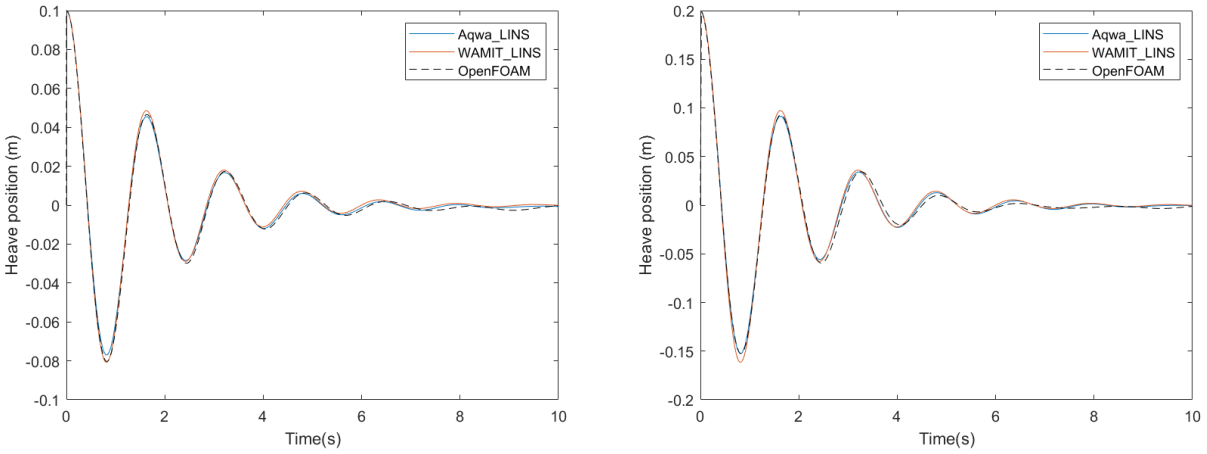

(a) DC1: Initial displacement 0.1m (b) DC2: Initial displacement 0.2m

Figure 57: Code-to-code comparison. Aqwa_LINS and WAMIT_LINS are linear solutions. OpenFOAM is CFD analysis which is strongly nonlinear

5.4 Radiation test

Introduction to the case: A radiation test was performed to evaluate the numerical radiation model. The float is subjected to a harmonically oscillating vertical force in otherwise still water. The test is designed to maintain motions within the linear regime, which means that the coned part of the float will not exit the water. In other word, the cross-sectional area is constant. Differences between the linear and weak nonlinear model are therefore expected to be neglectable. Actuator frequencies in the range 0.25 Hz to 1.00 Hz were conducted experimentally in the Sandia Lab. This range ensures that the natural period is covered, which based on numerical models was predicted to be approximately 0.6 Hz [10]. Table 9 illustrates the cases which were evaluated in this study and by other participants in IAE OES Task10. The time history of the actuator force used in the experiment was used as input in Aqwa. Note that the excitation forces are zero in a radiation test, and the force components of interest are the hydrostatic restoring force,F_S, and radiation force, F_R.

Test ID	Actuator frequency [Hz]	Wave Amplitude [m]	Steepness [m]
RA1	0.25	0.05	0.0006
RA2	0.60	0.05	0.0009
RA3	0.80	0.05	0.0016
RA4	1.00	0.05	0.0025

Table 9: Properties of the radiation test

Results: Figure 58 illustrates the heave response for the selected cases. It is seen that the response is well described by the Aqwa simulations in general. There are no deviations between the linear or weak nonlinear model in any of the cases. When the device is exited with a frequency of $0,6$Hz, which is in the proximity of the natural frequency, the numerical model overpredicts the motions response. This is most likely due to viscous effects which are prominent in the experiment and consequently reduces the motion amplitude. Neither the linear or weak nonlinear model considers viscous effects. Thus, to give some verification to this statement, the effect of including a viscous drag force in the numerical simulation was tested. It was implemented as a Morrison drag force, which can be described as

$$F_{dm} = C_{dm}|u|u \tag{5.2}$$

where C_{dm} is a drag coefficient and u is the vertical water particle velocity. An educated guess of the drag coefficient of $C_{dm} = \frac{Mass\ WEC\ float}{Diameter\ at\ SWL}$ was selected. The result is illustrated in figure 60, where it is seen that the viscous impact indeed improves the estimation of the motion response, and may explain the reduced motion observed in the experiment. The addition of a constant term to represent the effect of viscosity does not increase the computational time an appreciable extent. It could be a good improvement to the simulation with little extra cost in certain load conditions. The applied drag force is linear and the drag coefficient is only a good guess. Hence, this should be investigated further to obtain

more certainty around this observation. Is therefore suggested as an interesting topic for further work.

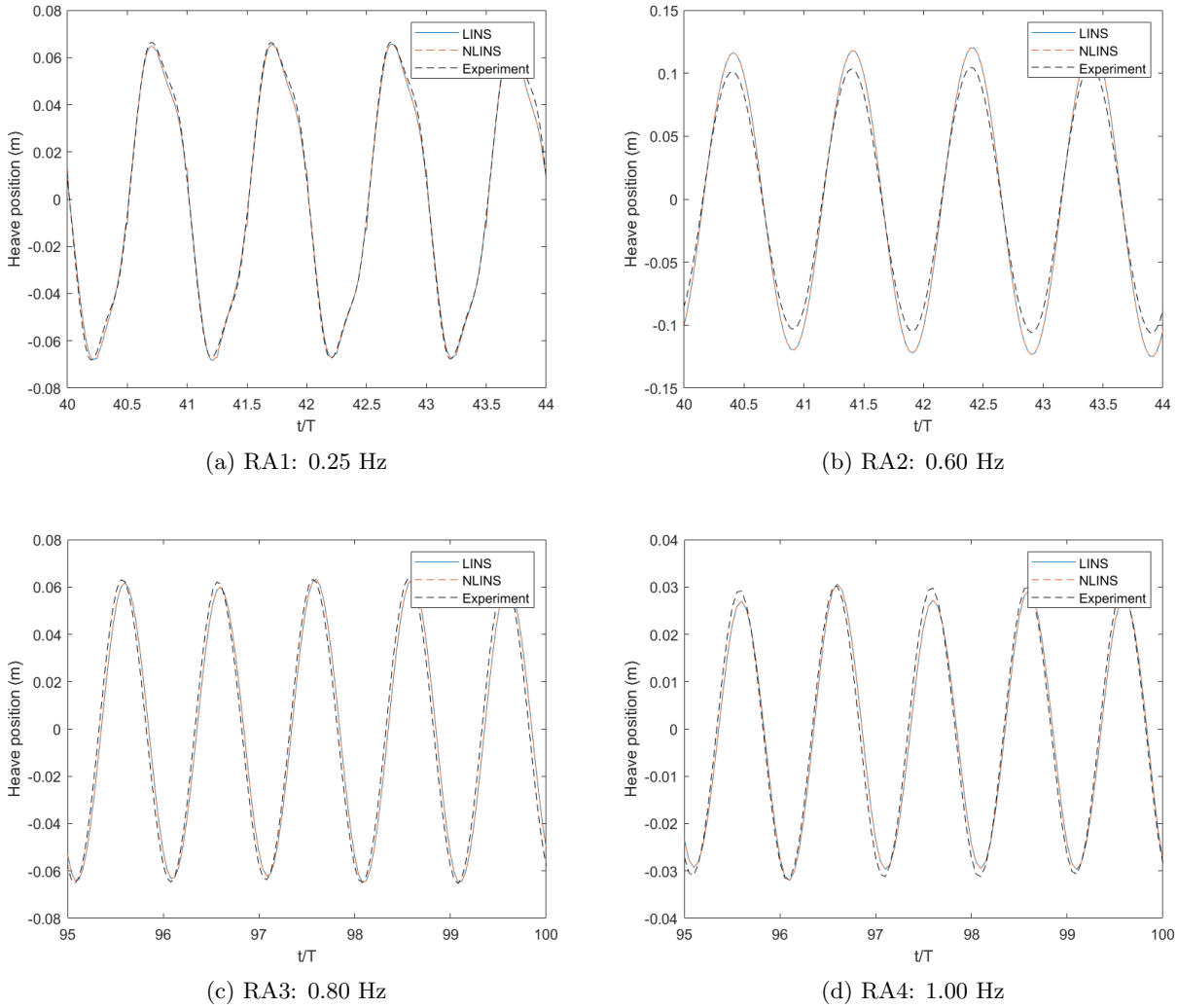

(a) RA1: 0.25 Hz

(b) RA2: 0.60 Hz

(c) RA3: 0.80 Hz

(d) RA4: 1.00 Hz

Figure 58: Compared heave position between experiment and numerical simulations

The PSD of the heave response were also of interest to investigate. The accuracy in the estimation of higher order effects vary for the different actuator frequencies. Firstly, higher order sub-harmonics induced by a harmonic motion are observed. In the experiment they occur at frequencies two and three times the wave frequency. The same phenomenon as was observed in some force PSD's during the sphere assessment. Some discussion regarding this observation can be found there, in the end of section 4.5.1. In the first(RA1) and

last(RA4) case, both higher order peaks are well captured by the numerics. In the case of resonant oscillation(RA2), the first and third order peak(1.8 Hz) are well captured, but the second peak(1.2 Hz) is slightly underpredicted by both numerical models. In the PSD of RA2 the numerical models are in general in good agreement with the experiment. The exception being that the numerical models predict a peak at a frequency of 1.6 Hz, which is not present in the experiment. This is somewhat strange, and it is more evident in RA3. There the first(0,80 Hz) and third(2,40 Hz) order peak are well described in Aqwa, but in the range between 1,2 Hz and 2,2Hz, Aqwa predicts three peaks which are not present in the experiment, as well as the second order peak(1.6 Hz) is not captured.

A part from RA3, the higher order peaks are generally well resolved. It was a bit unexpected that both the linear and weak nonlinear model would capture these effects so well. However, by looking at the PSD of the actuator force(input signal), it was observed that second and third order peaks were present(see figure 61). Hence, the reason the higher order peaks are so well resolved in the numerical simulation is most likely due to the peaks being present in the actuator force input signal.

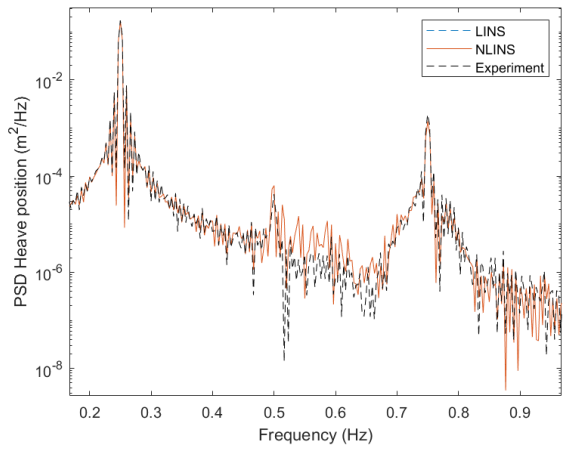

(a) RA1: 0.25 Hz

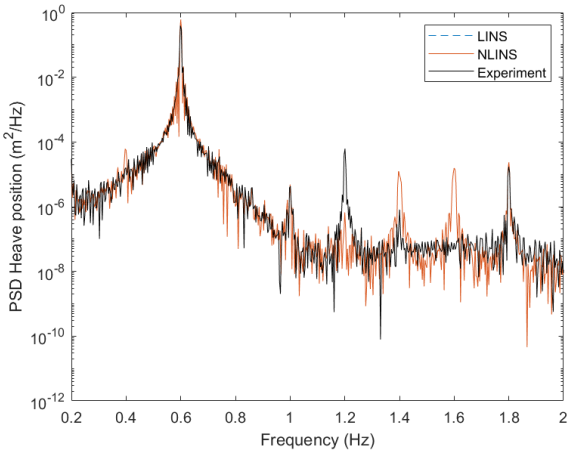

(b) RA2: 0.60 Hz

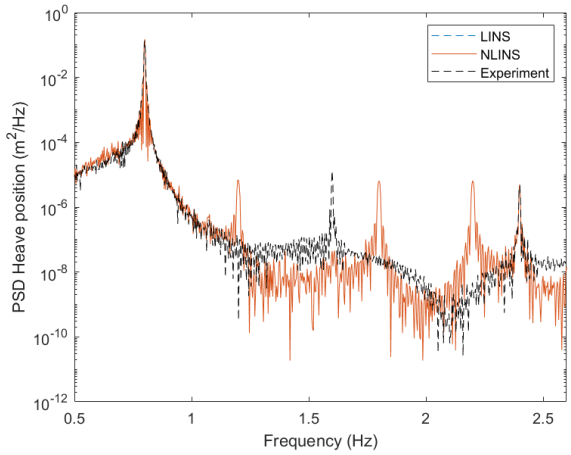

(c) RA3: 0.80 Hz

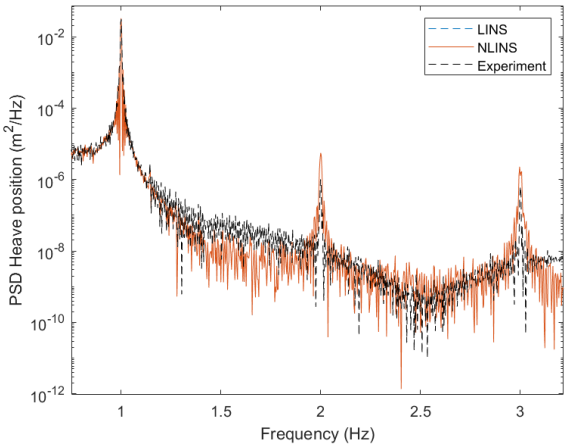

(d) RA4: 1.00 Hz

Figure 59: PSD of the heave response. Comparison between experiment and numerical simulation. Note that the spectrum of the linear solution(LINS) is difficult to see as it aligns with the spectrum of the weak nonlinear solution(NLINS)

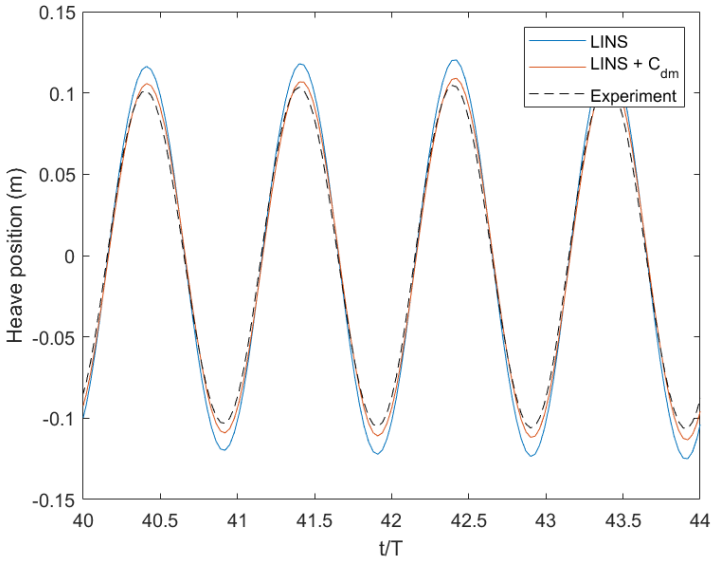

Figure 60: RA2 heave position. Comparison of the linear model(LINS), linear model with implemented Morrison drag(LINS + C_{dm}) and experimental data

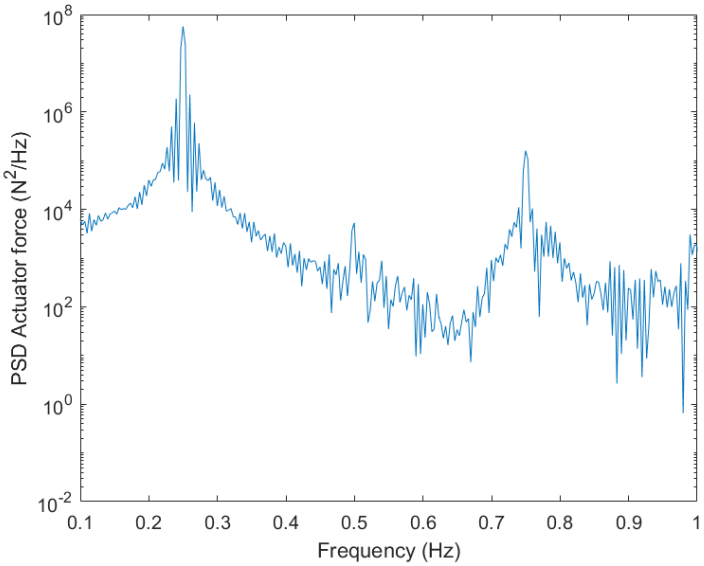

Figure 61: PSD of the actuator force in RA1. It shows that higher order peaks are present in the input force signal

5.5 Diffraction test

Introduction to the case: A diffraction test was performed to investigate the numerical diffraction model. In a diffraction test the float is fixed at the mean position and subjected to incident waves. The forces of interest are the wave excitation forces; Froude-Krylov and diffraction. Waves in the frequency range 0.25 Hz to 0.9 Hz and with amplitude 0.050m were tested in the experiment. An extra wave with frequency 0.60 Hz but half the amplitude (0.025m) was also tested. The waves are within the linear regime and covers the natural frequency of the float. Four cases were selected for numerical evaluation in IEA OES Task 10.2, which are presented in table 10. These cases include low frequency, resonant frequency and high frequency waves. These are also evaluated in this study.

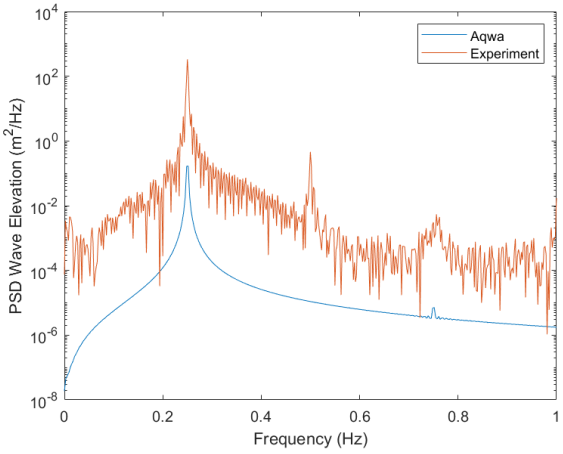

Figure 62: Wave spectrum for the Airy waves simulated in Aqwa and the waves generated in the experiment. Illustrated for waves with frequency 0.25 Hz and amplitude 0.05m

The time-series of the measured wave elevation in the Sandia Lab were supposed to be used as input in order to reproduce model test wave conditions as accurately as possible. However, some trouble with the implementation in Aqwa due to a minor bug in the lastest version(ANSYS v/2019 R2) at the time of writing made this difficult. This bug will according to ANSYS be fixed in the next version. Thus, the waves described in table 10 were simulated as regular Airy waves. Figure 62 illustrates the wave spectrum of the measured experimental waves and the simulated waves in Aqwa for DF1. This shows that higher order peaks are present in the waves generated in the experiment. Hence, eventual effects due to these sub-harmonics will not be captured in this study. Based on the results which will be presented below, this did not have any significant impact when compared to other participants in IEA OES Task 10.2, who used the wave elevation time-series from the Sandia Lab as input.

Test ID	Wave frequency [Hz]	Wave Amplitude [m]	Steepness [m]
DF1	0.250	0.050	0.0006
DF2	0.600	0.050	0.0037
DF3	0.600	0.025	0.0018
DF4	0.900	0.050	0.0083

Table 10: Properties of the diffraction test

Results: Figure 64 below illustrates the heave force related to the selected load conditions for the linear model, weak nonlinear model and the experimental data. Firstly, it is seen that the linear and weak nonlinear solution coincide in all four cases. The CSA is maintained constant, and consequently no weak nonlinearities are observed. Secondly, higher order frequencies are clearly present in the experiment. This could be due to the higher order peaks in the PSD of experimental wave time series in figure 62, which are not included regular waves simulated in Aqwa. However, when comparing to results from participants in IEA OES Task10.2, who used the experimental waves as input, these higher order frequencies are not present in the resulting heave force time series. The high frequency content could therefore rise from effects in the experimental set-up.

It is further observed that the heave force is underpredicted by simulations in the low frequency waves(DF1). The force amplitude seem to be closer for in DF2 and DF3. In DF4 the simulations seem to overpredict the heave force, and it is further noticed that the graph of the experimental heave force is shifted downwards. This latter observation is further discussed below. In figure 63 the heave force estimated in the numerical simulation is separated into contributions from the diffraction and Froude-Krylov forces. As seen before in this study, the Froude-Krylov force dominates when the wave period is long compared to the natural period of the body, and the diffraction forces tends to dominate when the frequency is high. In the experiment, the total heave force is measured through force sensors, and it is difficult to separate the force into incident wave and diffraction forces. However, if one relates the impact of these two force terms described in figure 63 to the comparison in heave force between experimental data and the numerical solutions illustrated in figure 64,it is evident that the heave force is underpredicted by the numerical models when the Froude-Krylov force is dominating and slightly overpredicted when the diffraction force is dominating. This could indicate that the numerical solutions underpredicts the Froude-Krylov force and overpredicts the diffraction force.

Lastly, the impact of including kinematic stretching was investigated. Kinematic stretching is the process of extending the Airy waves to predict the fluid velocity and acceleration at points above the mean water level. This subject is not covered in the theoretical background of this thesis, but information can be found in a study by Du et al.[13] who discussed and developed several approaches. Aqwa applies a method referred to as Wheeler stretching[57]. Figure 65 illustrates the estimated heave force acting on the float with and without the inclusion of Wheeler stretching for the weak nonlinear model. It is seen in figure 65(a) that there are no significant difference in DF1. In DF2 the waves are steeper and the kinematics above the mean water level are consequently more prominent. As can bee seen figure 65(b), the graph is shifted downwards. To physically interpret this, it is of importance to note that the heave force is in phase with the surface elevation. Positive heave force values occur during a wave crest and negative values occur during a wave through. Thus, the fact that the graph is shifted downwards implies that the magnitude of the estimated heave force during a crest is reduced and oppositely increased during a through when Wheeler stretching is applied. It is difficult to say weather this improves the estimation of the heave

force or not, due to the severe impact of higher order frequencies in the experimental data. However, when looking at the experimental data from DF2(figure 65(b)), one can see that the force graph is shifted downwards in a similar manner as for the numerical simulation with kinematic stretching. Meaning that the magnitude of the heave force is larger during a wave through than it is during a wave crest. This is not captured when considering the weak nonlinear model only, as the force amplitudes are equal during a wave crest and wave through. Furthermore, higher order effects are better described when Wheeler stretching is accounted for. Figure 66 shows the PSD of the heave force acting on the float during DF1 for the weak nonlinear model with and without Wheeler stretching. There on can see that the weak nonlinear model captures the first(0.25Hz) and third(0.75Hz) order peak, but not the one of second(0.50Hz) order. This peak is however somewhat captured when Wheeler stretching is included in the analysis.

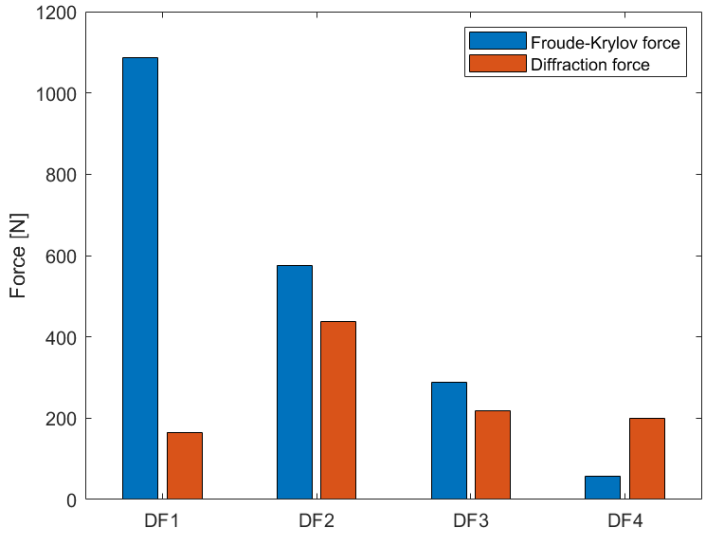

Figure 63: Impact of the Froude-Krylov and diffraction force for the selected test cases. The force amplitudes are here shown for the weak nonlinear model. The results from the linear solution were more or less identical.

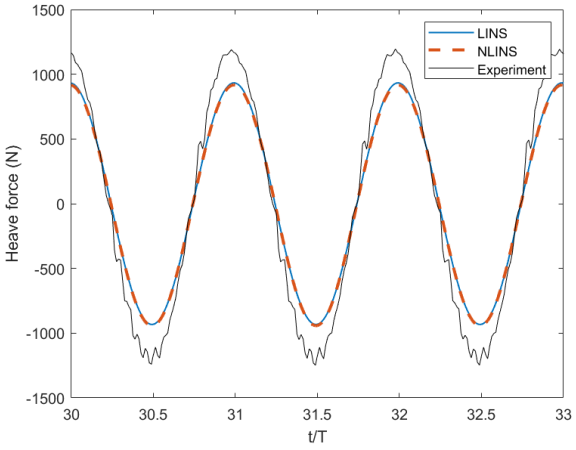

(a) DF1: Wave frequency 0.25 Hz, amlitude 0.050m

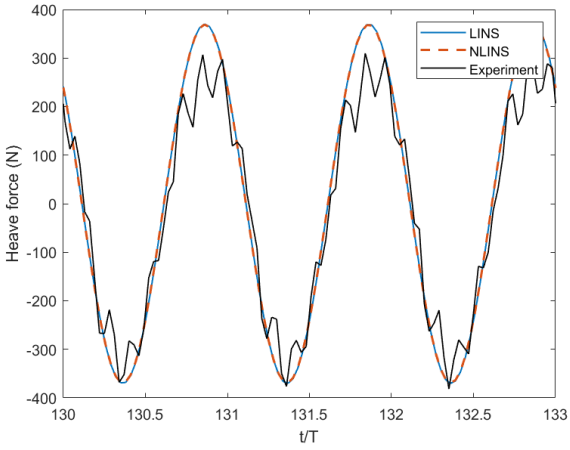

(b) DF2: Wave frequency 0.60 Hz, amlitude 0.050m

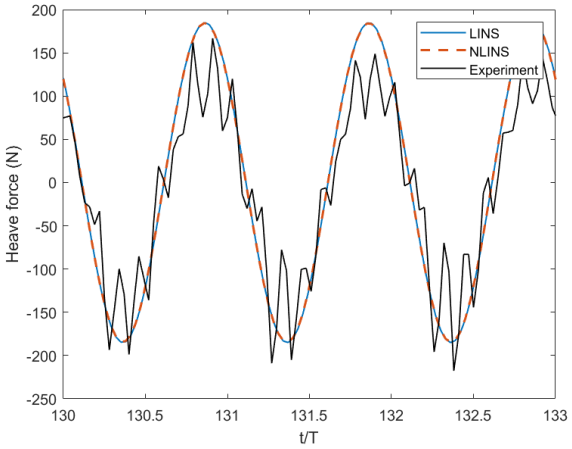

(c) DF3: Wave frequency 0.60 Hz, amlitude 0.025m

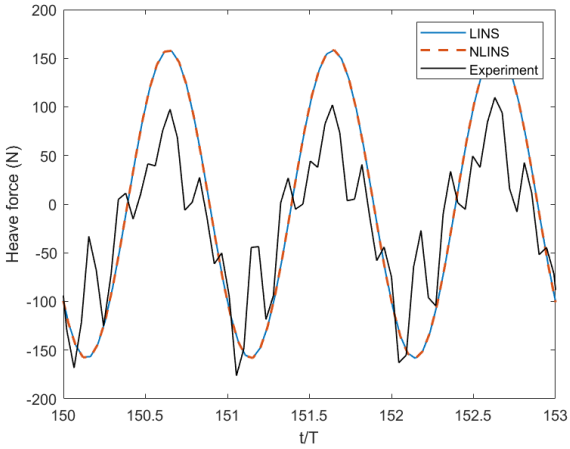

(d) DF4: Wave frequency 0.90 Hz, amlitude 0.050m

Figure 64: PSD of the heave force acting on the float during the tabled diffraction tests.

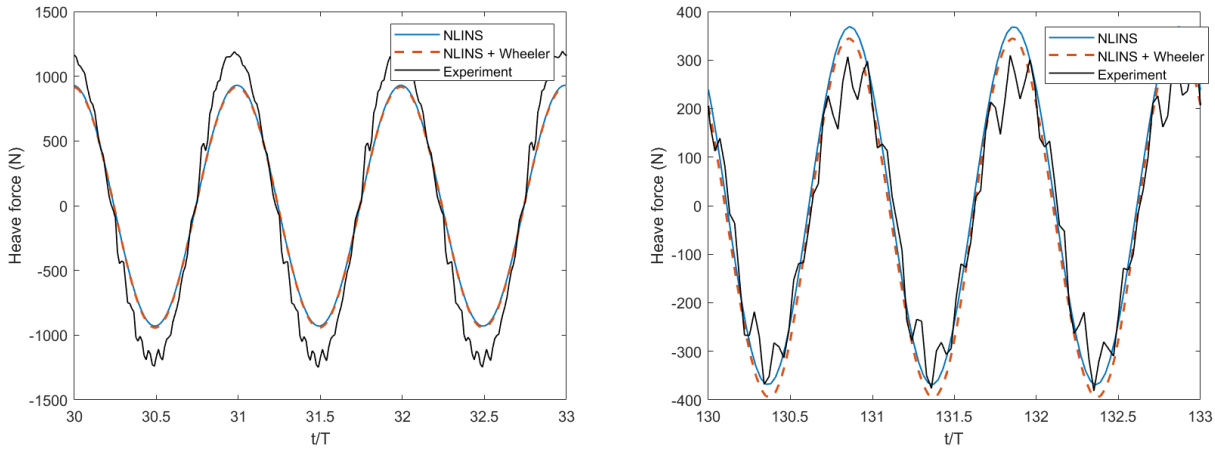

(a) DF1: Wave frequency 0.25 Hz, amlitude 0.050m (b) DF2: Wave frequency 0.60 Hz, amlitude 0.050m

Figure 65: Heave force acting on the float. Comparison of the weak nonlinear solution with and without Wheeler stretching and experimental data

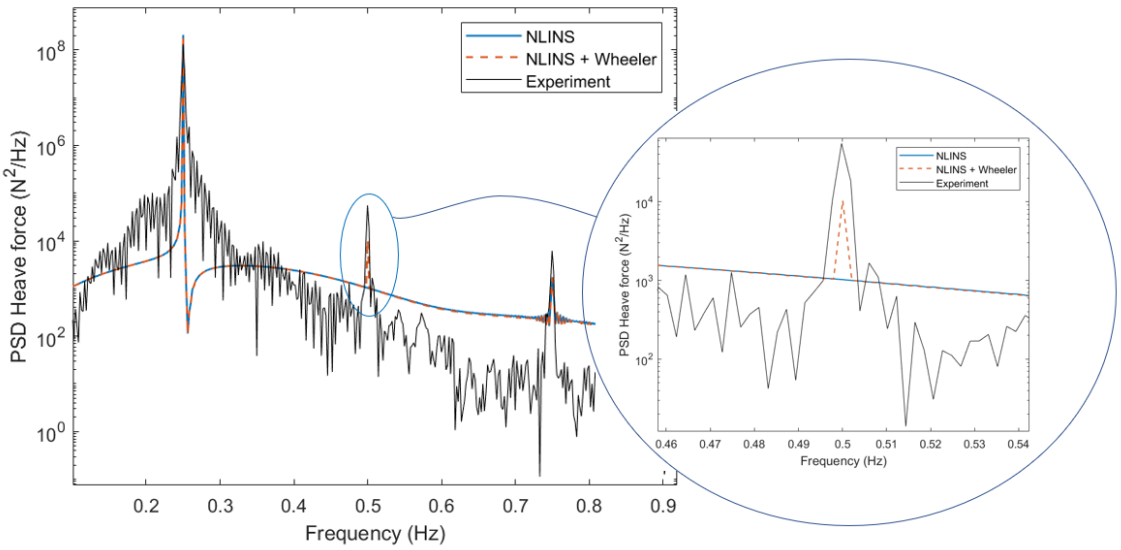

Figure 66: PSD of the heave force acting on the float in DF1. NLINS denotes the weak nonlinear model and NLINS+Wheeler implies that Wheeler stretching is included. In the magnification of the graph around the second order peak, one can clearly see that the peak is somewhat captured by the numerical solution when Wheeler stretching is applied. The third order peak is captured by both models.

5.6 Concluding remarks of the WEC float assessment

- The estimated added mass and radiation damping estimated with potential theory in Aqwa suited well with results from WAMIT and experimental data from Sandia Lab, which improves the vaidation of the numerical model.
- In the free-decay test the linear and weak nonlinear solution showed good agreement. The heave motion further coincided well with a strong nonlinear CFD simulation conducted in OpenFOAM.
- Weak nonlinear effect were generally not observed in any of the cases. That is because the load conditions in the test cases were remained within the linear regime, meaning that the CSA was kept constant. Thus, from this study it appears that when the immersed CSA is constant and the waves are rather linear, the linear model is sufficiently accurate. At least in terms of the Froudy-Krylov and hydrostatic forces.
- One of the advantages with validation against experimental data, is that it is easy to see weather certain effects improves the numerical modelling or not. Hence, during the radiation test a Morrison drag force was applied to simulate the effect of viscosity. An educated guess of the drag coefficient improved the numerical estimation. This have to be studied more closely before stating a conclusion. The addition of a viscous force term is however not computationally heavy, and could prove to be an efficient improvement for point-absorber analysis.
- On a similar basis as for the inclusion of a viscous term in the radiation test, the effect of kinematics above the mean water level was briefly evaluated in the diffraction test. Aqwa applies the method of Wheeler stretching. Due to the severe effect of higher order frequencies in the experimental data, it was rather difficult to see to what extent the inclusion of Wheeler stretching was an improvement or not. An effect that was observed however, was that the heave force amplitude during a wave through was larger than during a wave crest. This resulted in the time series of the heave force being shifted downwards. This was effect also evident in the experiment, but not in the weak nonlinear solution without Wheeler stretching. Lastly, it was seen that higher order peaks in the heave force PSD were better described.

6 Comparison of three float geometries with focus on absorbed power

This section compares three different geometries with focus on assessing the relevance of modelling nonlinear Froude-Krylov and hydrostatic forces in normal operating conditions, and to see how the geometry itself affects the absorbed power. The studied geometries are the sphere, a cylinder and the WEC float presented in section 5. The previous study of the sphere showed that nonlinear modelling of Froude-Krylov and hydrostatic forces are increasingly significant in steeper waves. The dimension of the sphere are however different in this case, as it is adapted to be comparable to the model scale WEC float. The cylinder is also dimensioned to be as comparable as possible to the WEC model.

Firstly, the geometries and load conditions as well as relevant body characteristics will be presented, followed by a decay test to ensure all geometries oscillates at the same and desired natural frequency. The geometries are thereafter evaluated when floating freely in regular waves without any PTO force. Lastly, the geometries are evaluated with focus on absorbed energy. A damping coefficient is applied to simulate a PTO force. The same formulation as described in (3.26) and (3.27) are used for the optimum damping and mean power.

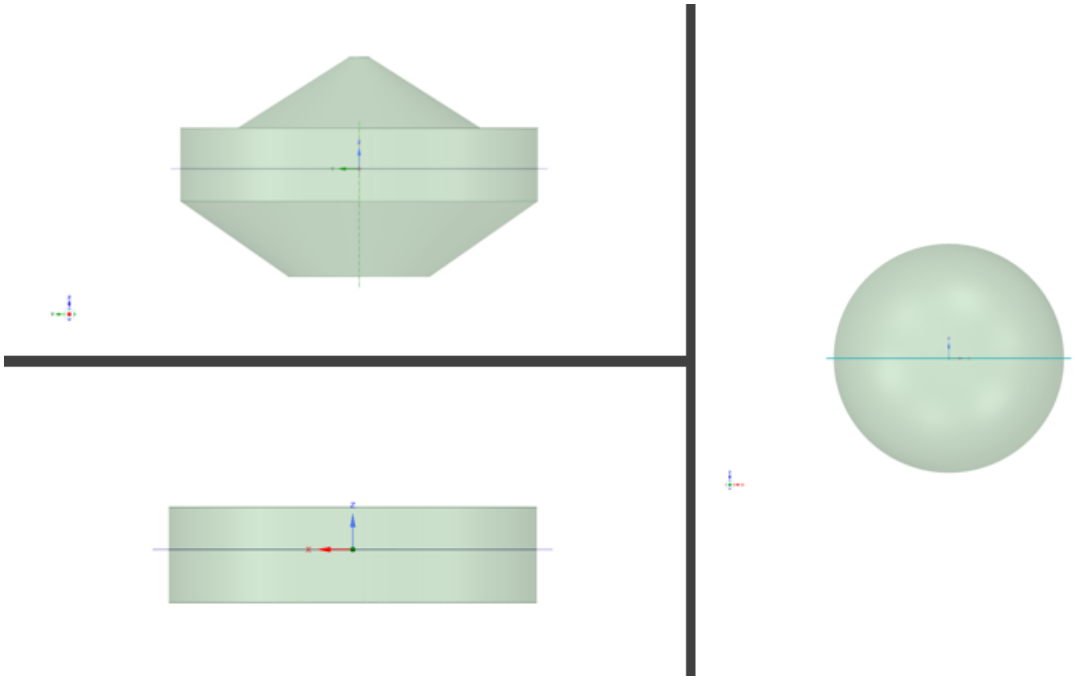

Figure 67: ANSYS SpaceClaim. Illustration of the investigated geometries

6.1 Model geometries and sea-states

The geometries are designed to have as much comparability as possible, to be able to compare the result. Obviously, it is not possible to obtain similar natural period, draft, radius or displaced volume etc. for all three geometries. Equality in the natural period was chosen as the main comparability criterion. That ensures that the body response characteristics are similar when exposed to the same load conditions. As a consequence the body mass and draft will be different.

To achieve similarity in the natural period, the body geometries had to be adapted appropriately. For the sphere, the radius is the controllable parameter. It was found through equation (4.1) with the desired natural period as input. For the cylinder the radius and draft can be adjusted. To obtain similar force magnitudes as the WEC float the radius was set equal to the WEC float, and the draft was adjusted to achieve the desired natural frequency. The algebraic equation for the natural frequency in heave for a cylinder as described in (6.1)was applied

$$\omega_0 = \sqrt{\frac{C_{33}}{M + A_\infty}} = \sqrt{\frac{\rho g \pi R_c^2}{\pi \rho R_c^2 d_c + \frac{4}{3}\rho R_c^3}} = \sqrt{\frac{\pi g}{\pi d_c + \frac{4}{3} R_c}} \tag{6.1}$$

where R_c is the cylinder radius and d_c is the draft. The expression used for the added mass is the analytical formulation for a heaving cylinder at infinite frequency $A_\infty = \frac{4}{3}\rho R_c^3$ [27]. This equation was solved with respect to the draft, which resulted in a rather flat cylinder with the same radius as the WEC float. This will lead to equality in the linear hydrostatic stiffness and forces acting on the bodies will be of similar magnitude. The sphere has the same natural period as the other two other geometries and consequently different radius. Table 11 summarizes the geometrical characteristics.

Parameters	**Sphere**	**WEC float**	**Cylinder**
Radius	0.658 m	0.880 m	0.880 m
Draft	0.658 m	0.530 m	0.253 m
Body mass	596 kg	858 kg	615 kg
Natural period	1.59 s	1.59 s	1.59 s
Natural frequency	0.63 Hz	0.63 Hz	0.63 Hz

Table 11: Physical properties

The WEC float is a model scale buoy. Hence, the size of the regular waves are determined thereafter, meaning that the incident waves in this study are smaller than operational ocean waves. The steepness can however remain the same as for full scale waves to simulate realistic conditions. A study by Retes et al.[49] investigated modelling with nonlinear Froude-Krylov forces on two full scale point absorbers. There it was argued that a steepness of 0.018, based on a wave with 6s period and 1m height in deep water, is appropriate. It describes realistic waves in operating conditions. This philosophy was adopted in this study,

and the steepness of the waves were set to 0.018. Note that this steepness is the direct ratio between the height and length of the wave. In terms of the expression for steepness used during the sphere assessment in section 4 and in IEA OES Task 10, it corresponds to $S = 0.0029$. Similarly to the sphere assessment, the steepness of the waves is remained constant to easily be able compare responses for different wave periods. Thus, the wave heights vary with the wave periods. The range of wave frequencies is chosen to cover the natural frequency of the geometries and to obtain some information of the behaviour in the diffracted and inertia dominated area. From the sphere assessment it was evident that the inertia dominated area is the one of interest regarding energy absorption. For that reason only one wave period lower than the natural period is investigated. The properties of the investigated waves are described in table 12.

Wave period [s]	**Wave frequency[Hz]**	**Wave height[m]**	**Wavelength[m]**
1.00	1.00	0.0281	1.5613
1.59	0.63	0.0708	3.9323
2.00	0.50	0.1124	6.2452
2.50	0.40	0.1756	9.7582
4.00	0.25	0.4497	24.9810

Table 12: Wave properties for the analysed sea-states with steepness 0.018

6.2 Decay test

To ensure that the sphere and cylinder have the natural frequencies estimated algebraically and to see weather the impact of nonlinearities are prominent or not, a decay test was performed. A third purpose with the decay test was to see how the hydrostatic characteristics differs for the geometries. The draft of the cylinder is rather limited, as it is only 0.253m. A decay test with initial displacement of 0.2m was therefore considered suitable, as the cylinder don't exit the water. A free-decay test with the WEC float is previously conducted in section 5.3. Those results showed that the linear and week nonlinear solution were in good agreement. Figure 68 shows the linear and weak nonlinear simulation of the free-decay for the sphere and cylinder. As for the WEC float the two models produce close to identical results. That is expected for the cylinder as the CSA is constant. The initial displacement was too low to induce any geometrical nonlinear effects in the sphere simulation.

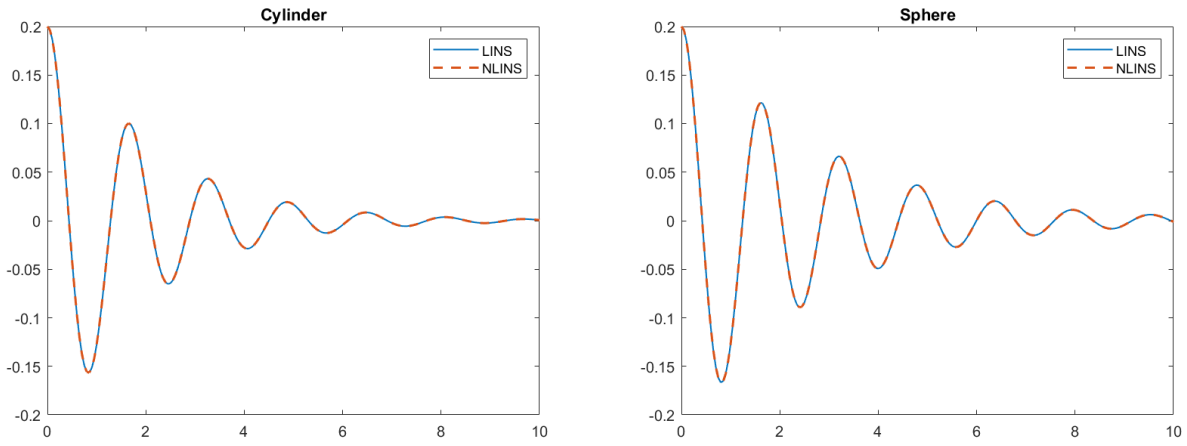

(a) Cylinder

(b) Sphere

Figure 68: Linear(LINS) and weak nonlinear(NLINS) free-decay simulation for the sphere and cylinder

More importantly, a look at the PSD in figure 69(b) verifies that all three geometries have a natural frequency of approximately 0.63 Hz. That implies that the design based on the algebraic equations were reasonable. One quickly notices that the sphere oscillates with highest amplitude. The behaviour of the WEC float and the cylinder are rather similar, with the cylinder oscillating with a slightly higher amplitude. This is also reflected in the height of the peaks in the heave position PSD plot. These differences arise from the fact that the geometries have different body mass and different added mass and damping characteristics. Figure 70 and 71 illustrates the hydrodynamic coefficients for all geometries. They are also plotted dimensionless to better illustrate the effect of the geometry regardless

of the mass difference. By looking at the radiation damping, one can clearly see that the one of the sphere is lowest. This is in line with the large motion amplitudes seen in the free-decay test. It comes as no surprise that the sphere geometry is more hydrodynamic in the vertical direction, which is visible in the relatively low added mass value. Regarding the two other geometries, it is seen in figure 70(a) that the damping coefficient for the WEC float is larger than for the cylinder, which is why the motion amplitudes of the WEC float is slightly smaller than the cylinder motion in the free-decay test. In the graph of the dimensionless radiation damping on the other hand, it is seen that the cylinder has a substantially larger damping coefficient than the WEC float. Hence, the reason for the lower WEC float motion amplitude is due to it being heavier than the cylinder. When the mass is excluded(dimensionless), and one only evaluates the geometry, it is seen that the WEC float has a lower damping than the cylinder. Furthermore, it is evident in the plot of the added mass that the coned shape of the lower part of the WEC float reduces the added mass compared to a cylinder, and one can state that the coned shape makes the WEC float more hydrodynamic.

As a short side note, in figure 71(a) one can see the added mass for the WEC float for low frequencies differs from the previously estimated added mass in the WEC assesment in section 5(see figure 53(a)). The reason for this observation is simply different water depths. To be able to compare the simulations to the experiment, the depth of the basin in the Sandia Lab of 6.1m was used, as opposed to in this section, where the water depth is deep. It somewhat highlights the importance of accounting for shallow water in cases where the deep water assumption is not viable.

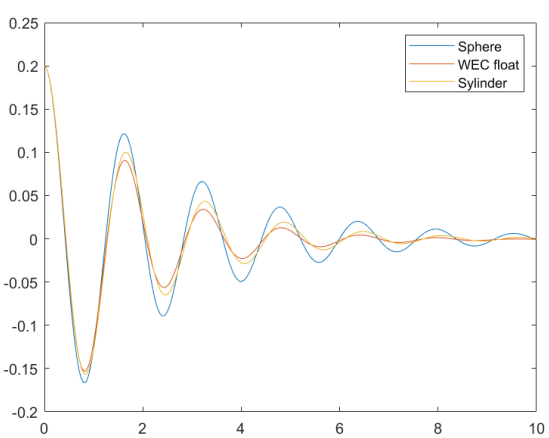

(a) Heave position time series

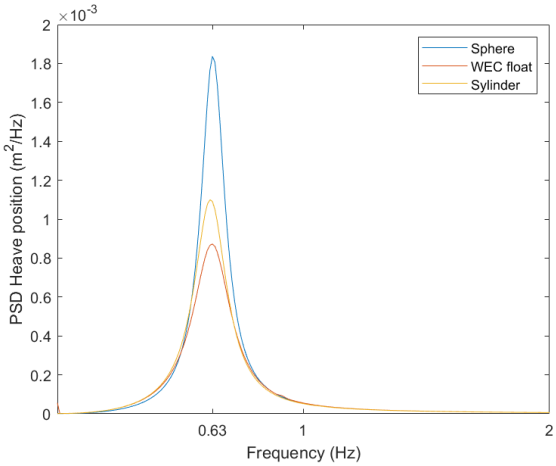

(b) Heave position PSD

Figure 69: Free-decay simulation for all three geometries. Initial displacement of 0.2m

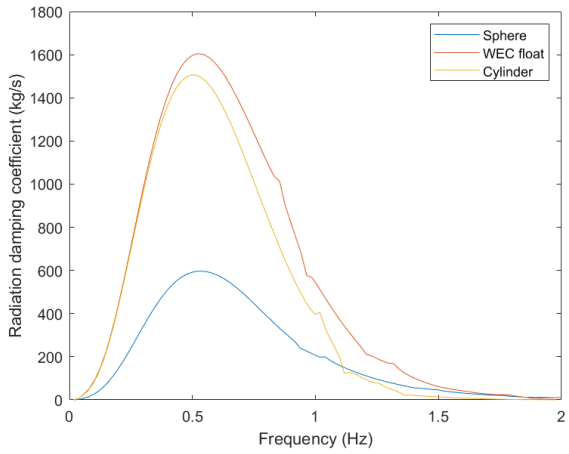

(a) Radiation damping coefficient

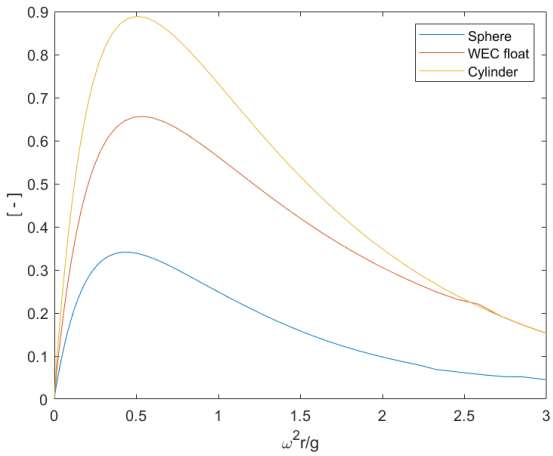

(b) Dimensionless radiation damping coefficient

Figure 70: Radiation damping for all three geometries. The dimensionless damping coefficient is expressed as $\lambda = \frac{B_{33}f}{m}$

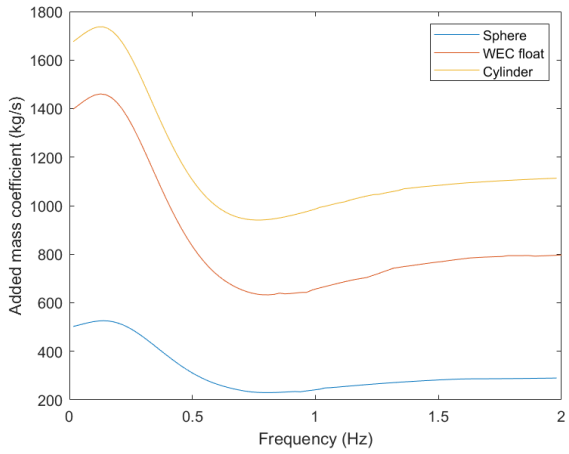

(a) Added mass coefficient

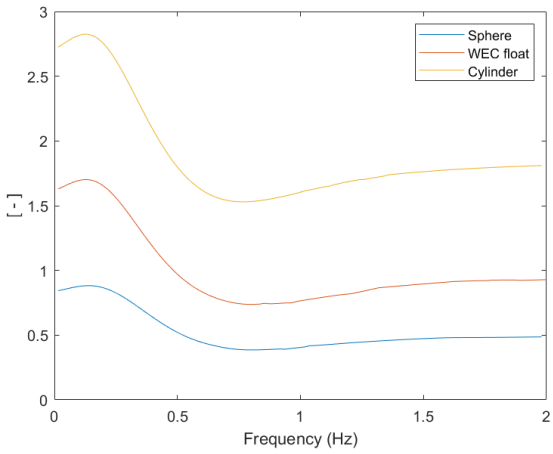

(b) Dimensionless added mass coefficient

Figure 71: Added mass for all three geometries. The dimensionless added mass coefficient is expressed as $\mu = \frac{A_{33}}{m}$

6.3 Uncontrolled motions in regular waves

Although the previous sphere assessment in section 4 highlights the effect of weak nonlinearities during uncontrolled motions in regular waves, it is interesting to analyse the effect the different geometries have in terms of motion response and the importance of modelling weak nonlinearities. It is of course expected that the effect of accounting for the instantaneous wetted surface is more prominent for the sphere than for both the WEC float and the cylinder. The responses of the devices are first analysed through the heave response RAO in the case where they move freely without any PTO damping. The results are plotted in figure 72 to 74. It is seen that there are little difference between the linear and nonlinear computation of Froude-Krylov and hydrostatic forces for all geometries. This is similar to what was observed during the assessment of the sphere, even for substantially steeper waves. It is further seen that the sphere is substantially excited in resonance compared to the two other geometries. Firstly, it is important to note that due to the steepness of the waves being maintained constant, the wave amplitude at resonance is quite low compared to the draft(see table 11 and 12). Hence, even though the RAO of the sphere at resonance is slightly below, it does not exit the water. This is also why no weak nonlinearities are induced at resonance, as the motions not are sufficiently large. Based on these results it is seen that the sphere obtains the largest motion amplitudes at resonance when the natural frequency is used as a similarity constraint. For longer wave periods it is seen that the geometry does not affect the motion response, as they all act as wave followers.

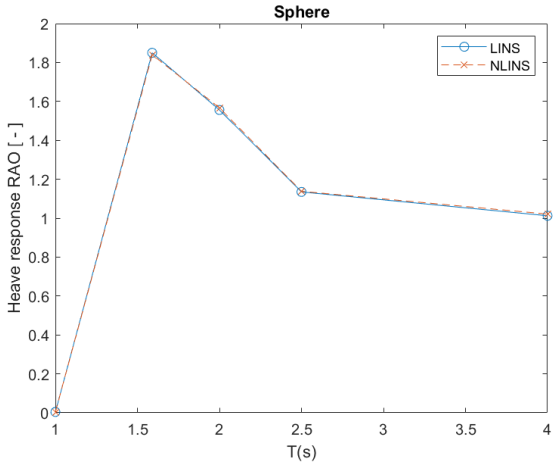

Figure 72: Heave response RAO in regular waves for the sphere

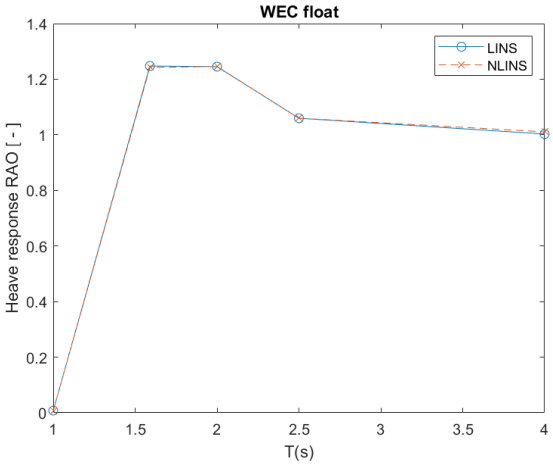

Figure 73: Heave response RAO in regular waves for the WEC float

A quick look at the force components described in figure 76 shows that the excitation forces are significantly larger for the WEC float and cylinder than for the sphere. That arises from the small radius of the sphere, which results in the pressure from the incident wave

and diffraction potential being integrated over a smaller area and consequently the force acting on the body is less. The radiation force is larger for the cylinder and WEC, which is reflected in the plots of the added mass and radiation damping under the free-decay test.

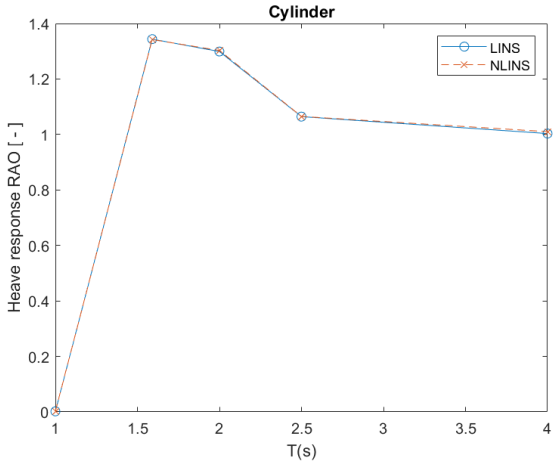

Figure 74: Heave response RAO in regular waves for the sphere

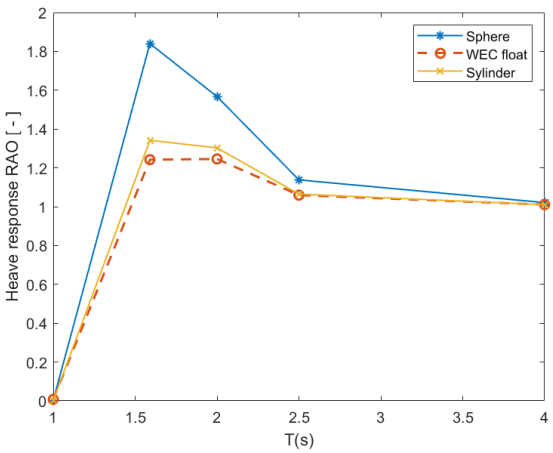

Figure 75: Heave response RAO in regular waves for all geometries for the weak nonlinear solution

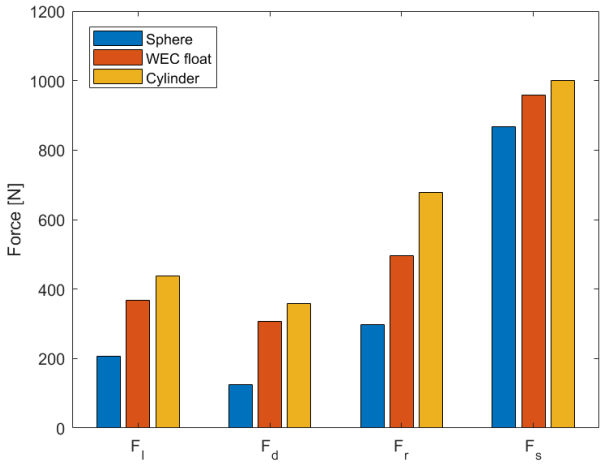

Figure 76: Amplitude of the Froude-Krylov(F_I), diffraction(F_d), radiation(F_r) and hydrostatic restoring(F_S) forces for all three geometries at resonance

6.4 Motions with optimum PTO force in regular waves

The geometries are further analysed in the same regular wave conditions but with an applied PTO force. The mean absorbed power and optimum PTO damping coefficient are estimated as previously described in section 3.3.3. The resulting optimum PTO damping for all three geometries are plotted for the relevant frequency range in figure 87. The optimum PTO damping for the sphere is smaller than for the cylinder and WEC float, which means that the required PTO force is less. For the two latter geometries the PTO damping coefficients are quite similar, and for wave periods in the inertia dominated area, they are close to identical.

T[s]	Sphere $B_{g,opt}[Ns/m]$	WEC float $B_{g,opt}[Ns/m]$	Cylinder $B_{g,opt}[Ns/m]$
1.00	3175	5753	6236
1.59	571	1527	1381
2.00	1556	2803	2675
2.50	2906	5012	4992
4.00	6777	11751	11705

Table 13: Optimum PTO damping properties

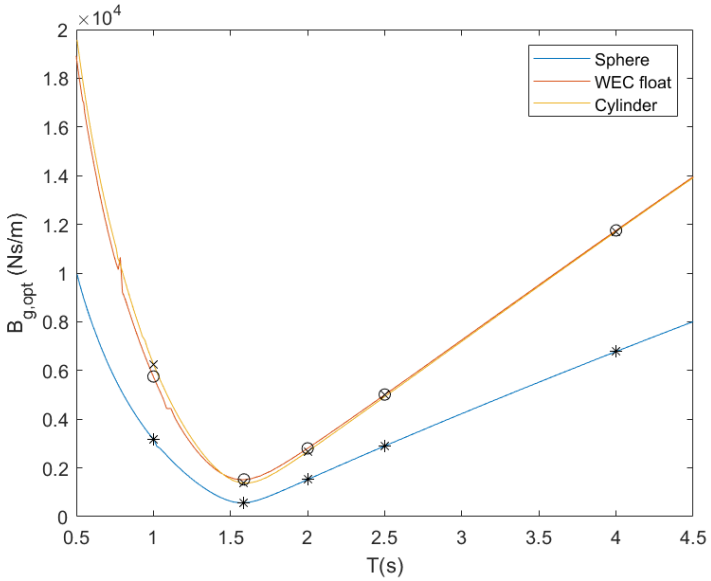

Figure 77: Optimum PTO damping coefficient for the studied frequency range. Tabulated values in table 13 are marked with $*$, o and x for the sphere, WEC float and cylinder respectively

The resulting RAO's are plotted in figure 78 to 81. Firstly, one can see that the linear and weak nonlinear models are in good agreement. The nonlinear solution is barely lower than the linear model in the sphere RAO. For the cylindrical geometries with constant CSA the models are seemingly identical. Secondly, the RAO of the sphere has a steeper resonance, and the relative motion is substantially larger than the two other devices. That is much due to the low optimum PTO damping, which can be seen in table 13. When looking at the mean power absorbed by the devices in figure 85, it is seen that the WEC float has the best performance, slightly above the cylinder. In spite of the large motions seen in the RAO, the sphere is inferior in terms of energy capture for large wave periods. It is important to note that this is highly effected by the fact that the excitation forces acting on the devices are larger for the cylindrical geometries due to the difference in size. In the formulation of the mean power in (3.27), it is seen that it is proportional to the square of the excitation force. Since the excitation force acting on a body increases with size, so do the absorbed mean power. Figure 86 illustrates the foregoing for the longest wave(T=4s). This is a consequence of forcing the devices to oscillate with similar natural period.

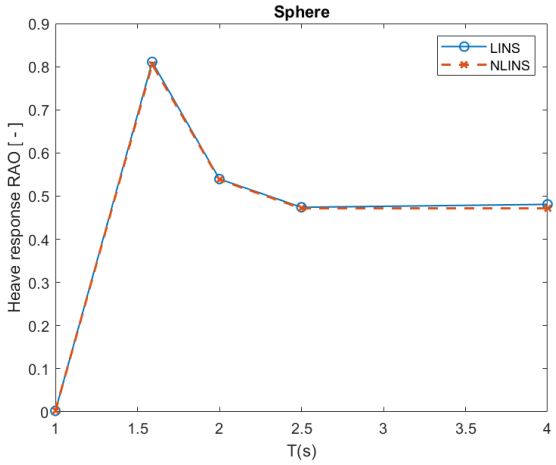

Figure 78: Heave response RAO in regular waves for the sphere

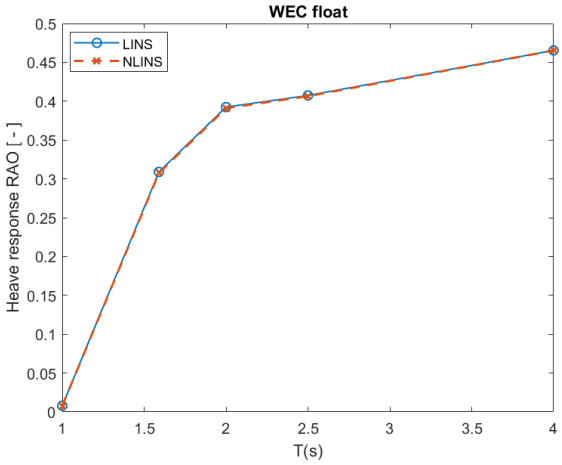

Figure 79: Heave response RAO in regular waves for the WEC float

An effort was done to better visualize the geometrical effects regarding absorbed power by plotting the mean power normalized by the weight of each device. The result showed that the cylinder geometry is superior in terms of captured energy per body weight in long wave periods. At resonance the sphere and cylinder performs at the same rate, while the WEC float is slightly below. Thus, according to this finding, a cylinder is more mass effective when designing a heaving point-absorber with respect to a predetermined natural frequency. Note that the cylinder is rather flat, and the impact from other rotational degrees of freedom is expected to be significant. Inclusion of such effects could give rise to other conclusions. The sphere performs well at resonance, but absorbs less power for increased waves periods.

A previous study by Eriksson [16] argued that the shape of the buoys of similar size don't have a significant impact considering energy absorption when the body is operating off resonance. That is in line with the resulting mean power for the WEC float and cylinder in figure 85, who are considered of similar size. It is seen that absorbed power is increasingly similar further away from the resonant wave period. At resonance on the other hand, the geometry has a greater impact. This can be seen in the same figure, where it is evident that the WEC float performs slightly better than the cylinder. This do highlight that in practical applications where control methods such as latching is applied to force the device to oscillate in resonance, the geometry is indeed of importance.

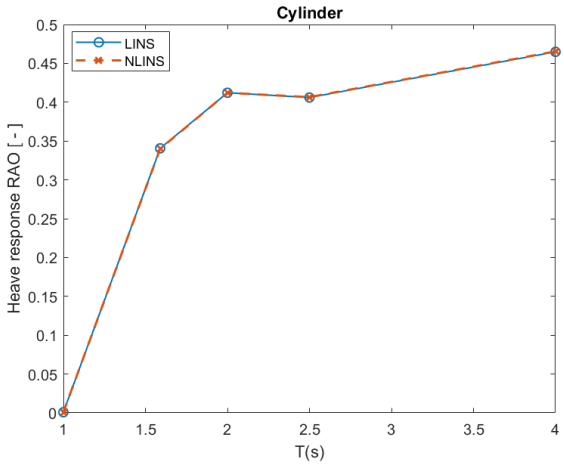

Figure 80: Heave response RAO in regular waves for the cylinder

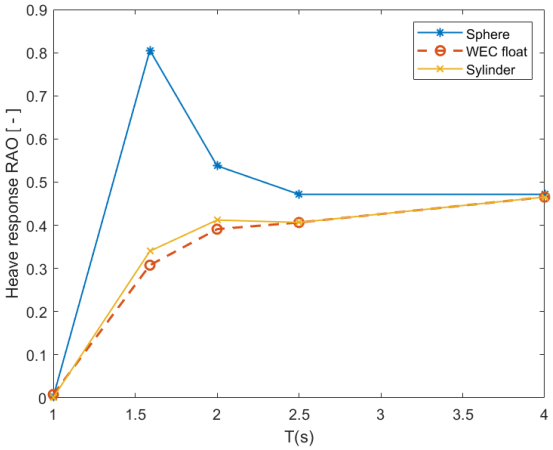

Figure 81: Heave response RAO in regular waves for all geometries

Based on the results regarding nonlinear modelling of Froude-Krylov and hydrostatic forces, it appears that the linear model remains a good approximation when the CSA is constant. It has to be mentioned that the regular waves applied in this section are linear, and the amplitude of the motion in relation to the free surface elevation did not exceed the dimensions of the devices. For the sphere , the effect of weak nonlinearities were only prominent when a PTO force was applied(see figure 82). The same observation was done in the sphere assessment, where it was seen that the weak nonlinear solution predicts a significantly lower vertical Froude-Krylov force.

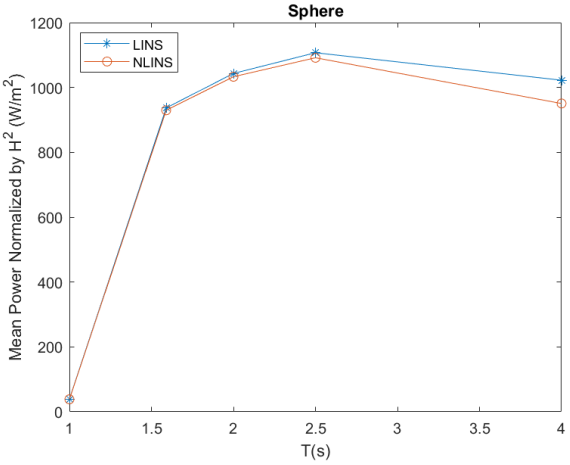

Figure 82: Mean power normalized by the square of the wave height for the sphere

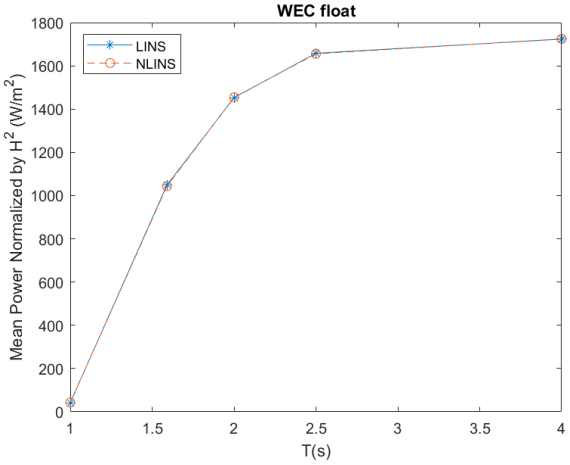

Figure 83: Mean power normalized by the square of the wave height for the WEC float

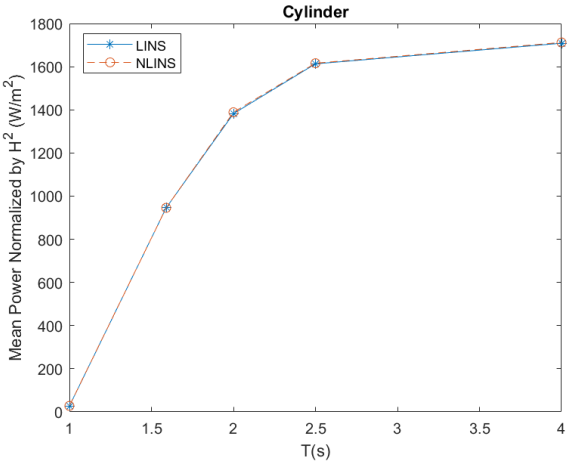

Figure 84: Mean power normalized by the square of the wave height for the cylinder

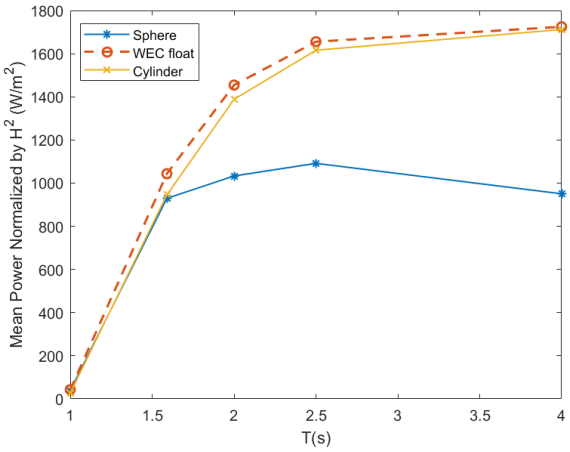

Figure 85: Mean power normalized by the square of the wave height for all geometries. The weak nonlinear model is plotted here

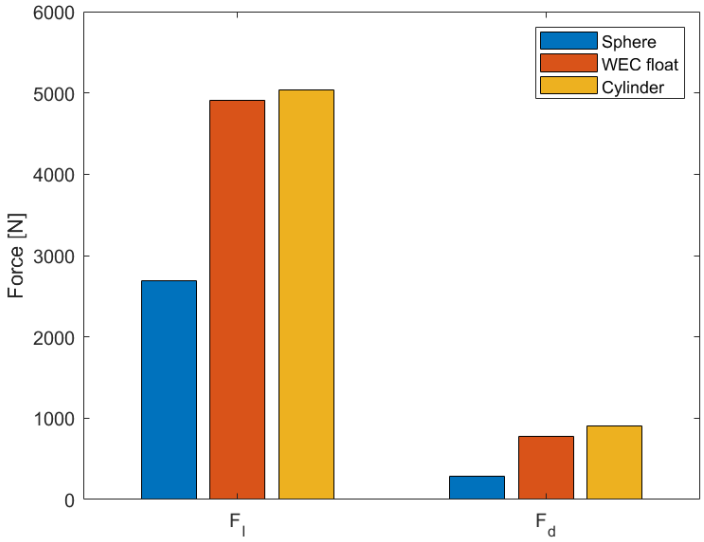

Figure 86: Amplitude of the Froude-Krylov(F_I) and diffraction(F_d) forces for $T = 4s$

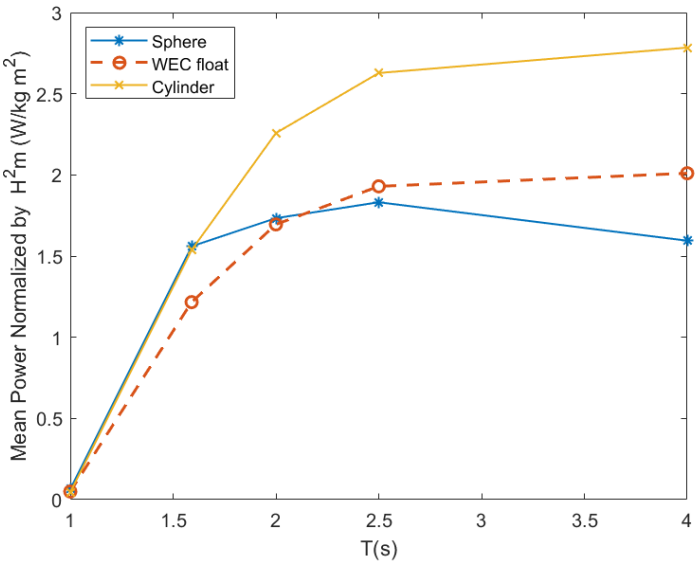

Figure 87: Mean power normalized by the square of the wave height and the weight of the devices for the weak nonlinear solution

6.5 Concluding remarks

- **Free-decay:**The free-decay test showed that designing the size of the cylinder and sphere based on analytical formulations for the natural period were good, as the same natural frequencies were obtained numerically. No deviations between the linear and weak nonlinear model were observed for any of the geometries. It was further seen that the coned shape of the WEC float reduces the added mass. The WEC float is heavier than the cylinder, and therefore has a higher radiation damping. However, the dimensionless radiation damping coefficient, which excludes the mass and highlights the geometrical effects, showed that the coned shape reduces the damping. The vertical added mass and damping of the sphere is substantially lower, illustrating it's hydrodynamic shape.
- **Uncontrolled motions in regular waves:** The same trend as observed in the free-decay test regarding motion amplitudes were seen in the heave response RAO's. The sphere oscillates with the highest amplitude of the geometries at resonance. The WEC float and the cylinder oscillates rather similar, with the cylinder having a slightly higher amplitude. The devices acts as wave followers for longer periods. The linear and weak nonlinear model coincides and are in good agreement for all three geometries. The excitation force acting on the sphere was reduced compared to the two other geometries due to the short radius, which turned out to affect the mean power.
- **Motions with optimum PTO force in regular waves:** Based on the results regarding nonlinear modelling of Froude-Krylov and hydrostatic forces, it appears that the linear model remains accurate when the CSA is constant. For the sphere where the immersed CSA varies over time, the weak nonlinear effects were prominent when PTO damping was considered. This is the same observation which was seen during the sphere assessment under section 4. More detailed discussion is found there. In terms of absorbed energy the WEC float performed best out of the three geometries, both in resonance and for longer periods given the constraint of similar natural period. For the longest period(T=4s), the mean power coincided with the mean power absorbed by the cylinder. Based on these result the geometry is of less importance when oscillating off resonance. The size of the device is then of major importance, which was evident in the performance of the sphere. This was explained as follows: the magnitude of the exciting forces acting on the body increases with size due to the pressure from the incident and diffracted waves being integrated over a larger area. Since the mean power is proportional to the square of the excitation forces, an increase in size will subsequently increase the mean power. That is why the sphere captures less power in large waves, i.e when the incident wave force is dominant. In resonance, where the waves and consequently Froude-Krylov forces are smaller, the sphere performs at a similar rate as the two other geometries despite the small radius.

7 Conclusion

The first objective of the thesis was to assess the effect of accounting for the instantaneous wetted body surface in the estimation of Froude-Krylov and hydrostatic forces. It appears from the results of this study that when the immersed cross-sectional area(CSA) is constant and the waves are rather linear, the linear model can remain accurate. At least in terms of the Froudy-Krylov and hydrostatic forces. When the immersed CSA changes over time, which is the case for the sphere, nonlinear geometrical effects were induced in large waves and in resonance. The effect was most prominent when an additional damping was applied in large incident waves. There it was seen that the weak nonlinear solution predicted a reduced heave response compared to the linear model, which resulted in a drastically reduced mean power estimation. Based on the findings in this thesis, the linear solution can in this case give an overoptimistic estimation of mean power and consequently give a misleading guide to economic predictions. In linear conditions on the other hand, the linear and weak nonlinear model were in good agreement also for the sphere.

The second objective was to investigate the three geometries with respect to absorbed energy. It was seen that the WEC float absorbed most energy out of the three geometries at resonance and in longer waves. The sphere performed at a similar rate as the two other geometries at resonance, but absorbed substantially less power for larger waves due to the small size. It was argued with the following reasoning: the magnitude of the exciting forces acting on the body increases with size due to the pressure from the incident and diffracted waves being integrated over a larger area. Since the mean power is proportional to the square of the excitation forces, an increase in size will subsequently increase the mean power. Lastly, it was seen that the geometry has a severe impact at resonance, but seem to have less effect when oscillating off resonance. That implies that when control methods are applied, which forces the device to oscillate in resonance, the geometry is important.

Other findings which are not discussed here can be found under the concluding remarks for each numerical assessment.

8 Suggestions for future work

The numerical assessments only accounts for heave motion, and the only external force is the PTO damping. To describe a WEC in more realistic conditions, the points below could be included in future analysis.

- Include PTO damping and mooring stiffness.
- Increase the amount of DOF's. Firstly it is suggested look at the rotary pitch/roll motion.
- Further investigate the effect of viscosity.
- Further investigate the effect of Wheeler stretching.
- Optimise the absorbed power with the use of a control mechanism, i.e latching.
- Look at the behaviour in irregular waves.

References

[1] Aderinto, T. Ocean wave energy converters: status and challenges. *Energies*, 11(5) (2018).

[2] Akar, S., and Akbaş Akdoğan, D. *Environmental and Economic Impacts of Wave Energy:*. 01 2016.

[3] Alcorn, R. Wave energy, 2014.

[4] Alves, M. Chapter 2 - frequency-domain models. In *Numerical Modelling of Wave Energy Converters*, M. Folley, Ed. Academic Press, 2016, pp. 11 – 30.

[5] ANSYSInc. Aqwa v2019 R1 Theory Manual.

[6] Bailey, H. The effect of a nonlinear power take off on a wave energy converter. *The University of Edinburgh* (2009).

[7] Budal, K. A resonant point absorber of ocean-wave power, 1975.

[8] Budal, K., and Falnes, J. Apparatus for utilizing or absorbing wave energy. *British patent No. 1587344* (1978).

[9] Bull, D., Coe, R., Monda, M., Dullea, K., Bacelli, G., and Patterson, D. Design of a physical point-absorbing wec model on which multiple control strategies will be tested at large scale in the mask basin. vol. 2015-, International Society of Offshore and Polar Engineers, pp. 957–965.

[10] Coe, R. G.

[11] Cummins, W. E. The impulse response function and ship motions, 1962.

[12] Du, S., Hudson, D., Price, W., and Temarel, P. The occurrence of irregular frequencies in forward speed ship seakeeping numerical calculations. *Ocean Engineering 38*, 1 (2011), 235–247.

[13] Du, S. X., Hudson, D. A., Price, W. G., and Temarel, P. Implicit expressions of static and incident wave pressures over the instantaneous wetted surface of ships. *Proceedings of the Institution of Mechanical Engineers, Part M: Journal of Engineering for the Maritime Environment 223*, 3 (2009), 239–256.

[14] Energy Information Administration. International energy outlook. *Available online: https://www.eia.gov/outlooks/ieo/* (2018).

[15] Engström, J. Hydrodynamic modelling for a point absorbing wave energy converter, 2011.

[16] Eriksson, M. Modelling and experimental verification of direct drive wave energy conversion: Buoy-generator dynamics, 2007.

[17] Eriksson, M., Waters, R., Svensson, O., Isberg, J., and Leijon, M. Wave power absorption: Experiments in open sea and simulation. *Journal of Applied Physics 102*, 8 (2007).

[18] Evans, D. V. A theory for wave-power absorption by oscillating bodies. *Journal of Fluid Mechanics 77*, 1 (1976), 1–25.

[19] Falcão, A. Modelling of wave energy conversion.

[20] Falnes, J. Optimum control of oscillation of wave-energy converters, 1993.

[21] Falnes, J. Small is beautiful : how to make wave energy economic, 1994.

[22] Falnes, J. Principles for capture of energy from ocean waves. phase control and optimum oscillation.

[23] Falnes, J. Ocean waves and oscillating systems: Linear interactions including wave-energy extraction, 2002.

[24] Falnes, J. A review of wave-energy extraction. *Marine Structures 20*, 4 (2007), 185–201.

[25] Falnes, J., and Budal, K. Wave-power conversion by point absorbers. *Norw Marit Res 6* (01 1978), 2–11.

[26] Falnes, J., and Hals, J. Heaving buoys, point absorbers and arrays. *Philosophical Transactions: Mathematical, Physical and Engineering Sciences 370*, 1959 (2012), 246–277.

[27] Faltinsen, O. M. *Sea Loads on ship and offshore structures*. Cambridge University Press, 1990.

[28] French, M. J. A generalized view of resonant energy transfer. *Journal of Mechanical Engineering Science 21*, 4 (1979), 299–300.

[29] Giorgi, G., and Ringwood, J. Comparing nonlinear hydrodynamic forces in heaving point absorbers and oscillating wave surge converters. *Journal of Ocean Engineering and Marine Energy 4*, 1 (2018), 25–35.

[30] Giorgi, G., and Ringwood, J. V. Analytical representation of nonlinear froude-krylov forces for 3-dof point absorbing wave energy devices. *Ocean Engineering 164* (2018), 749 – 759.

[31] Guenther, D. A., Jones, D., and Brown, D. G. An investigative study of a wave-energy device. *Energy 4*, 2 (1979), 299–306.

[32] Havelock, T. Waves due to a floating sphere making periodic heaving oscillations. *Proceedings of the Royal Society of London. Series A, Mathematical and Physical Sciences (1934-1990) 231*, 1184 (1955), 1–7.

[33] Hess, J. L. Calculation of non-lifting potential flow about arbitrary three-dimensional bodies, 1962.

[34] Hotta, H., Washio, Y., Yokozawa, H., and Miyazaki, T. Rd on wave power device "mighty whale". *Renewable Energy 9*, 1 (1996), 1223 – 1226. World Renewable Energy Congress Renewable Energy, Energy Efficiency and the Environment.

[35] Hulme, A. The wave forces acting on a floating hemisphere undergoing forced periodic oscillations. *Journal of Fluid Mechanics 121*, 57 (1982), 443–463.

[36] Ilyas, A., Kashif, S. A., Saqib, M. A., and Asad, M. M. Wave electrical energy systems: Implementation, challenges and environmental issues. *Renewable and Sustainable Energy Reviews 40* (2014), 260–268.

[37] International Renewable Energy Agency. *Available online: https://www.irena.org/ocean*.

[38] J Cargo, C., Plummer, A., Hillis, A., and Schlotter, M. Determination of optimal parameters for a hydraulic power take-off unit of a wave energy converter in regular waves. *Proceedings of the Institution of Mechanical Engineers, Part A: Journal of Power and Energy 226* (02 2012), 98–111.

[39] Langer, C. M. *Marine Dynamics*. Department of Marine Technology, NTNU, 2015.

[40] Le Mehaute, B. An introduction to hydrodynamics and water waves, 1976.

[41] Leishman, J. The development of wave power : a techno - economic study, 1976.

[42] Mehlum, E. Tapchan. *IN: OCEAN SPACE UTILIZATION '85, PROC. INT. SYMP., (TOKYO, JAPAN: JUN. 4-6, 1985), W. KATO (ED.) 1* (1985).

[43] Mørk, G., Barstow, S., Kabuth, A., and Teresa Pontes, M. Assessing the global wave energy potential. vol. 3.

[44] Newland, D. E. An introduction to random vibrations, spectral wavelet analysis, 2005.

[45] Newman, J. N. *Marine hydrodynamics*. MIT Press, 1977.

[46] Ocean Energy Systems. Annual report ocean energy systems 2016. *Available online: https://report2016.ocean-energy-systems.org* (2017).

[47] Pettersen, B. *TMR4247 Marin Teknikk 3, Hydrodynamikk. 2007*.

[48] Pinkster, J. A. Low frequency second order wave exciting forces on floating structures, 1980.

[49] Retes, M. P., Merigaud, A., Gilloteaux, J.-C., and Ringwood, J. Nonlinear froude-krylov force modelling for two heaving wave energy point absorbers. *Proceedings of the 11th European Wave and Tidal Energy Conference* (2015).

[50] Ross, D. *Power from the waves*. Oxford University Press, 1995.

[51] Salter, S. H. Wave power. *Nature 249*, 5459 (1974).

[52] Tedd, J., and Peter Kofoed, J. Measurements of overtopping flow time series on the wave dragon, wave energy converter. *Renewable Energy 34*, 3 (2009), 711–717.

[53] Todalshaug, J. H., Ásgeirsson, G. S., Hjálmarsson, E., Maillet, J., Möller, P., Pires, P., Guérinel, M., and Lopes, M. Tank testing of an inherently phase-controlled wave energy converter. *International Journal of Marine Energy 15*, C (2016), 68–84.

[54] Tom, N., Lawson, M., Yu, Y., and Wright, A. Development of a nearshore oscillating surge wave energy converter with variable geometry. *Renewable Energy 96* (2016), 410 – 424.

[55] Vicinanza, D., and Frigaard, P. Wave pressure acting on a seawave slot-cone generator. *Coastal Engineering 55*, 6 (2008), 553–568.

[56] Wendt, F., Yu, Y.-H., Nielsen, K., Ruehl, K., Bunnik, T., Touzon, I., Nam, B., Kim, J., Kim, K.-H., Janson, C., Jakobsen, K.-R., Crowley, S., Vega, L., Rajagopalan, K., Mathai, T., Greaves, D., Ransley, E., Lamont-Kane, P., Sheng, W., Costello, R., Kennedy, B., Thomas, S., López, M., Bingham, H., Kurniawan, A., Kramer, M., Ogden, D., Girardin, S., Babarit, A., Wuillaume, P.-Y., Steinke, D., Roy, A., Beatty, S., Schofield, P., Jansson, J., and Hoffman, J. *International Energy Agency Ocean Energy Systems Task 10 Wave Energy Converter Modeling Verification and Validation*. Technical Committee of the European Wave and Tidal Energy Conference, 2017.

[57] WHEELER, J. Method for calculating forces produced by irregular waves. *JPT, Journal of Petroleum Technology 22*, 3 (1970), 359–367.

[58] Yemm, R., Pizer, D., Retzler, C., and Henderson, R. Pelamis: Experience from concept to connection. vol. 370, Royal Society, pp. 365–380.

Anders Matias Akselsen

Hydrodynamic Analysis of a Floating Renewable Energy Device

NTNU
Norwegian University of
Science and Technology

EDR™ MEDESO